SCDAP/RELAP5/MOD3.1 Code Manual
Volume II: Damage Progression Model Theory

Contributing Authors:
C. M. Allison
G. A. Berna
T. C. Cheng
E. W. Coryell
K. L. Davis
D. L. Hagrman
D. T. Hagrman
J. K. Hohorst
S. Paik
A. S. Shieh
L. J. Siefken

Editor:
K. L. Davis

ABSTRACT

The SCDAP/RELAP5 code has been developed for best estimate transient simulation of light water reactor coolant systems during a severe accident. The code models the coupled behavior of the reactor coolant system, the core, fission products released during a severe accident transient as well as large and small break loss of coolant accidents, operational transients such as anticipated transient without SCRAM, loss of offsite power, loss of feedwater, and loss of flow. A generic modeling approach is used that permits as much of a particular system to be modeled as necessary. Control system and secondary system components are included to permit modeling of plant controls, turbines, condensers, and secondary feedwater conditioning systems.

This volume contains detailed descriptions of the severe accident models and correlations. It provides the user with the underlying assumptions and simplifications used to generate and implement the basic equations into the code, so an intelligent assessment of the applicability and accuracy of the resulting calculation can be made.

EXECUTIVE SUMMARY

The specific features of SCDAP/RELAP5/MOD3.1 are described in this five volume set of manuals covering the theory, use, and assessment of the code for severe accident applications. This set replaces the SCDAP/RELAP5/MOD3 Code Manual, NUREG/CR-5273.

The SCDAP/RELAP5 computer code is designed to describe the overall reactor coolant system (RCS) thermal-hydraulic response, core damage progression, and in combination with VICTORIA[a], fission product release and transport during severe accidents. The code is being developed at the Idaho National Engineering Laboratory (INEL) under the primary sponsorship of the Office of Nuclear Regulatory Research of the U.S. Nuclear Regulatory Commission (NRC).

The code is the result of merging the RELAP5/MOD3[b] and SCDAP models. The RELAP5 models calculate the overall RCS thermal hydraulics, control system interactions, reactor kinetics, and the transport of noncondensable gases. Although previous versions of the code have included the analysis of fission product transport and deposition behavior using models derived from TRAP-MELT, this capability is being replaced through a data link to the detailed fission product code, VICTORIA, as a result of an effort to reduce duplicative model development and assessment.

The SCDAP code models the core behavior during a severe accident. Treatment of the core includes fuel rod heatup, ballooning and rupture, fission product release, rapid oxidation, zircaloy melting, UO_2 dissolution, ZrO_2 breach, flow and freezing of molten fuel and cladding, and debris formation and behavior. The code also models control rod and flow shroud behavior.

The RELAP5 code is based on a nonhomogeneous and nonequilibrium model for the two-phase system that is solved by a fast, partially implicit numerical scheme to permit economical calculation of system transients. The objective of the RELAP5 development effort from the outset was to produce a code that includes important first order effects necessary for accurate prediction of system transients but is sufficiently simple and cost effective such that parametric or sensitivity studies are possible. The development of SCDAP/RELAP5 has this same focus.

The code includes many generic component models from which general systems can be simulated. The component models include fuel rods, control rods, pumps, valves, pipes, heat structures, reactor point kinetics, electric heaters, jet pumps, turbines, separators, accumulators, and control system components. In addition, special process models are included for effects such as form loss, flow at an abrupt area change, branching, choked flow, boron tracking, and noncondensable gas transport.

The development of the current version of the code was started in the spring of 1992. This version contains a number of significant improvements to the SCDAP models since the last versions of the code, SCDAP/RELAP5/MOD2.5 and SCDAP/RELAP5/MOD3[7af], were released. These improvements include the addition of several new models to describe the earlier phases of a severe accident, changes in

---

a. T. Heames et al., *VICTORIA: A Mechanistic Model of Radionuclide Behavior in the Reactor Coolant System Under Severe Accident Conditions,* NUREG/CR-5545, SAND90-0756, Rev. 1, December 1992.
b. C. M. Allison, C. S. Miller, N. L. Wade (Eds.) *RELAP5/MOD3 Code Manual*, Volumes I through IV, NUREG/CR-5535, EGG-2596, June 1990.

the late phase models to provide more "physically intuitive" behavior for full plant calculations, and changes to improve the overall reliability and usability of the code. The improvements in the early phase models include the addition of models to treat (a) the effects of grid spacers including the effects of Inconel spacer grid-zircaloy cladding material interactions, (b) BWR B_4C control blade-zircaloy channel box material interactions, and (c) accelerated heating, melting, and hydrogen generation during the reflood of damaged fuel rods. An extension to the molten pool models to treat the sporadic growth of the boundaries of the molten pool into adjacent regions of relatively intact assemblies or rubble debris beds is the most significant change to the late phase models. Improvements in overall reliability and usability of the code for plant calculations include changes in the overall code numerics to reduce the likelihood of numerical instabilities or code failures and changes in the codes input/output processors. The most noticeable of these for the code users is the conversion of the SCDAP input to a form more compatible with the RELAP5 style. In addition to these modeling and coding changes, SCDAP/RELAP5/MOD3.1 has also been subjected to (a) an intensive effort of verification testing to identify and resolve outstanding code errors and (b) a systematic assessment of the code to quantify the uncertainties in the predicted results.

This volume, Volume II, describes models which are resident only to the SCDAP portion of the code, and contains detailed descriptions of the damage progression models and correlations. It provides the user with the underlying assumptions and simplifications used to generate and implement the basic equations into the code, so an intelligent assessment of the applicability and accuracy of the resulting calculation can be made.

ACKNOWLEDGMENTS

CONTENTS

LIST OF FIGURES

LIST OF TABLES

ACRONYMS

ADI   Alternating Direction Implicit

ANS   American Nuclear Society

ANSI   American National Standards Institute

BWR   Boiling Water Reactor

DOE   U. S. Department of Energy

RCS   Reactor Coolant System

IEEE   Institute of Electrical and Electronic Engineers

INEL   Idaho National Engineering Laboratory

IPR   Independent Peer Review

LOFT   Loss-of-Fluid Test

LWR   Light Water Reactor

NPA   Nuclear Plant Analyzer

NRC   U. S. Nuclear Regulatory Commission

OECR   Odd Even Cyclic Reduction

ORNL   Oak Ridge National Laboratory

PBF   Power Burst Facility

PWR   Pressurized Water Reactor

QA   Quality Assurance

QPP   Quality Program Plan

SNL   Sandia National Laboratory

TMI   Three Mile Island

VFP   Volatile Fission Product

SCDAP/RELAP5/MOD3.1 Code Manual
Volume II: Damage Progression Model Theory

1. INTRODUCTION

The SCDAP/RELAP5 computer code is designed to describe the overall reactor coolant system (RCS) thermal-hydraulic response, core damage progression, and, in combination with VICTORIA[1], fission product release and transport during severe accidents. The code is being developed at the Idaho National Engineering Laboratory (INEL) under the primary sponsorship of the Office of Nuclear Regulatory Research of the U.S. Nuclear Regulatory Commission (NRC).

1.1 General Code Capabilities

The code is the result of merging the RELAP5/MOD3[2] and SCDAP[3] models. The RELAP5 models calculate the overall RCS thermal hydraulics, control system interactions, reactor kinetics, and transport of noncondensable gases. Although previous versions of the code have included the analysis of fission product transport and deposition behavior using models derived from TRAP-MELT, this capability is being replaced through a data link to the detailed fission product code, VICTORIA, as a result of an effort to reduce duplicative model development and assessment. The SCDAP models calculate the damage progression in the core structures and the formation, heatup, and melting of debris.

SCDAP/RELAP5 is capable of modeling a wide range of system configurations from single pipes to different experimental facilities to full scale reactor systems. The configurations can be modeled using an arbitrary number of fluid control volumes and connecting junctions, heat structures, core components, and system components. Flow areas, volumes, and flow resistances can vary with time through either user control or models that describe the changes in geometry associated with damage in the core. System structures can be modeled with RELAP5 heat structures, SCDAP core components, or SCDAP debris models. The RELAP5 heat structures are one-dimensional models with slab, cylindrical, or spherical geometries. The SCDAP core components include representative light water reactor (LWR) fuel rods, silver-indium-cadmium (Ag-In-Cd) and B_4C control rods and/or blades, electrically heated fuel rod simulators, and general structures. A two-dimensional, finite element model based upon the COUPLE[4] code may be used to calculate the heatup of debris and/or surrounding structures. This model takes into account the decay heat and internal energy of newly fallen or formed debris and then calculates the transport by conduction of this heat in the radial and axial directions to the wall structures and water surrounding the debris. Perhaps the most important use of this model is to calculate the heatup of the vessel wall so that the time at which the vessel may rupture can be determined. Other system components available to the user include pumps, valves, electric heaters, jet pumps, turbines, separators, and accumulators. Models to describe selected processes, such as reactor kinetics, control system response, and tracking noncondensable gases, can be invoked through user control.

The development of the current version of the code was started in the spring of 1992. This version contains a number of significant improvements since the last versions of the code, SCDAP/RELAP5/MOD2.5 and SCDAP/RELAP5/MOD3[7af], were released. These improvements include the addition of several new models to describe the earlier phases of a severe accident, changes in the late phase models to

provide more "physically intuitive" behavior for full plant calculations, and changes to improve the overall reliability and usability of the code. The improvements in the early phase models include the addition of models to treat (a) the effects of grid spacers including the effects of Inconel spacer grid-zircaloy cladding material interactions, (b) BWR B_4C control blade-zircaloy channel box material interactions, and (c) accelerated heating, melting, and hydrogen generation during the reflood of damaged fuel rods. An extension to the molten pool models to treat the sporadic growth of the boundaries of the molten pool into adjacent regions of relatively intact assemblies or rubble debris beds is the most significant change to the late phase models. Improvements in overall reliability and usability of the code for plant calculations include changes in the overall code numerics to reduce the likelihood of numerical instabilities or code failures and changes in the codes input/output processors. The most noticeable of these for the code users is the conversion of the SCDAP input to a form more compatible with the RELAP5 style. In addition to these modeling and coding changes, SCDAP/RELAP5/MOD3.1 has also been subjected to (a) an intensive effort of verification testing to identify and resolve outstanding code errors, and (b) a systematic assessment of the code to quantify uncertainties in the predicted results.

1.2   Relationship to Other NRC-Sponsored Software

SCDAP/RELAP5 and RELAP5 are developed in parallel and share a common configuration. Both codes share a common source deck. Separate codes are formed only prior to compilation, so changes made to the source deck are automatically reflected in both codes.

The development and application of the code is also related to several other NRC-sponsored software packages. Theoretical work associated with the development of PARAGRASS-VFP[5] has resulted in model improvements for fission product release. A data link to the VICTORIA code will allow for the detailed treatment of phenomena such as fission product and aerosol transport, deposition, and resuspension. A link with PATRAN[6] and ABAQUS[7] provides the user with the means to calculate the details of lower head failure. Animated plant response displays are possible through links to the Nuclear Plant Analyzer (NPA)[8] display software, which gives the user an efficient way of analyzing the large amount of data generated. Detailed plant simulations from accident initiation through release of fission products to the atmosphere are made available through links to the CONTAIN[9] containment response and CRAC2[10] or MACCS[11] atmospheric dispersion consequence codes.

1.3   Quality Assurance

SCDAP/RELAP5 is maintained under a strict code configuration system that provides a historical record of the changes made to the code. Changes are made using an update processor that allows separate identification of improvements made to each successive version of the code. Modifications and improvements to the coding are reviewed and checked as part of a formal quality program for software. In addition, the theory and implementation of code improvements are validated through assessment calculations that compare the code-predicted results to idealized test cases or experimental results.

1.4   Organization of the SCDAP/RELAP5 Manuals

The specific features of SCDAP/RELAP5/MOD3.1 are described in a five-volume set of manuals covering the theory, use, and assessment of the code for severe applications. Although Volume I describes (a) the overall code architecture, (b) interfaces between the RELAP5 system models, and (c) any system models unique to SCDAP/RELAP5, the code user is referred to the companion set of six volumes which describe the RELAP5[2] system thermal hydraulics and associated models.

Volume I presents a description of SCDAP/RELAP5/MOD3.1-specific thermal-hydraulic models (relative to RELAP5/MOD3), and interfaces between the thermal-hydraulic models and damage progression models.

Volume II contains detailed descriptions of the severe accident models and correlations. It provides the user with the underlying assumptions and simplifications used to generate and implement the basic equations into the code, so an intelligent assessment of the applicability and accuracy of the resulting calculation can be made.

Volume III provides the user's guide and code input for the severe accident modeling. SCDAP input was recently changed to be consistent with the free-form input used by RELAP5. User guidelines are produced specifically for the severe accident code. The user should also refer to the RELAP5/MOD3 Code Manual Volume V: User Guidelines for a complete set of guidelines.

Volume IV describes the material property library, MATPRO. It contains descriptions of the material property subroutines available for severe accident analysis.

Volume V documents the assessments of SCDAP/RELAP5/MOD3.1 performed on versions released since the 1993 deficiency resolution effort. It includes nodalization sensitivity studies and time-step sensitivity studies, assessments using standard PWR and BWR plant models, and assessments using code-to-data comparisons.

1.5   Organization of Volume II

Volume II describes models resident only to the SCDAP portion of the code. Sections 2 and 3 describe the heat conduction and material oxidation models used by the fuel rod and other core component models. Section 4 describes models specific to the fuel rod component. Other core component models are discussed in Section 5, which includes the Ag-In-Cd control rod model, the new BWR B_4C control blade and channel box model, the older B_4C control rod model, and the flow shroud model. Section 6 describes the capabilities of the two-dimensional COUPLE model, and Section 7 covers the lumped parameter core region debris modeling. Section 8 discusses the creep rupture models, and Section 9 lists references.

2. HEAT CONDUCTION MODEL FOR CORE COMPONENTS

This section describes the heat conduction model used to calculate the temperature response for the fuel rod, Ag-In-Cd control rod, B_4C control rod, and shroud components.

2.1 Two-Dimensional Heat Conduction Governing Equation

In the cylindrical coordinate system, the integral form of the heat conduction equation for an isotropic solid continuum is:

$$\int_V \rho c_p \frac{\partial T}{\partial t} dV = \int_V \frac{1}{r}\frac{\partial}{\partial r}(rk\frac{\partial T}{\partial r}) dV + \int_V \frac{1}{r^2}\frac{\partial}{\partial \theta}(k\frac{\partial T}{\partial \theta}) dV + \int_V \frac{\partial}{\partial z}(k\frac{\partial T}{\partial z}) dV + \int_V Q_V dV + \int_B Q_s ds_B \qquad (2\text{-}1)$$

where

Q_V	=	volumetric heat source (nuclear, oxidation, W/m^3)
Q_s	=	surface heat flux (convective, radiative, W/m^2)
T	=	temperature at location (r, z) at time t where r and z are the radial and axial coordinates respectively (K)
ρc_p	=	volumetric heat capacitance ($J/m^3 \cdot K$)
k	=	thermal conductivity ($W/m \cdot K$).

By assuming that no heat is transferred in the θ direction, and by applying the divergence theorem to the right-hand side of the integral form of the heat conduction equation, the following two-dimensional heat conduction governing equation is obtained:

$$\int_V \rho c_p (T, r, z) \frac{\partial}{\partial t} T(r, z, t) dV = \int_S k(T, r, z) \nabla T(r, z, t) ds + \int_V Q_V(r, z, t) dV + \int_B Q_s(r, z, t) ds_B . \quad (2\text{-}2)$$

2.2 Finite Difference

The difference method used in the code is similar to the approach used in the finite volume method in Reference 12. However, instead of differencing the partial differential equation directly, the integral form of the partial differential equation, Equation (2-2), is differenced. Unlike the finite volume method where the mesh point is placed at half a mesh spacing from the boundary or the interface between two material layers, here the mesh points are placed at the boundary or at the interface between two different material layers. While this approach has the advantage of maximizing the accuracy of discretization at the boundary when, for example, the convective boundary condition is imposed, it also means that a control volume surrounding a typical mesh point will in general overlap mesh cells that lie in different material layers. Because of this, it is necessary to examine the mesh cells adjacent to a given mesh point (i,j) in some detail.

Consider the four mesh cells surrounding the mesh point (i,j) as shown in Figure 2-1. It is assumed that each of these mesh cells contains materials of one kind only so that the thermal conductivity or heat capacitance is essentially constant over each mesh cell. A control volume surrounding the mesh point (i,j)

will have $(i + \frac{1}{2}, j + \frac{1}{2})$, $(i + \frac{1}{2}, j - \frac{1}{2})$, $(i - \frac{1}{2}, j + \frac{1}{2})$, and $(i - \frac{1}{2}, j - \frac{1}{2})$ as its vertices and will overlap all four mesh cells.

M051-BDR-1191-0017
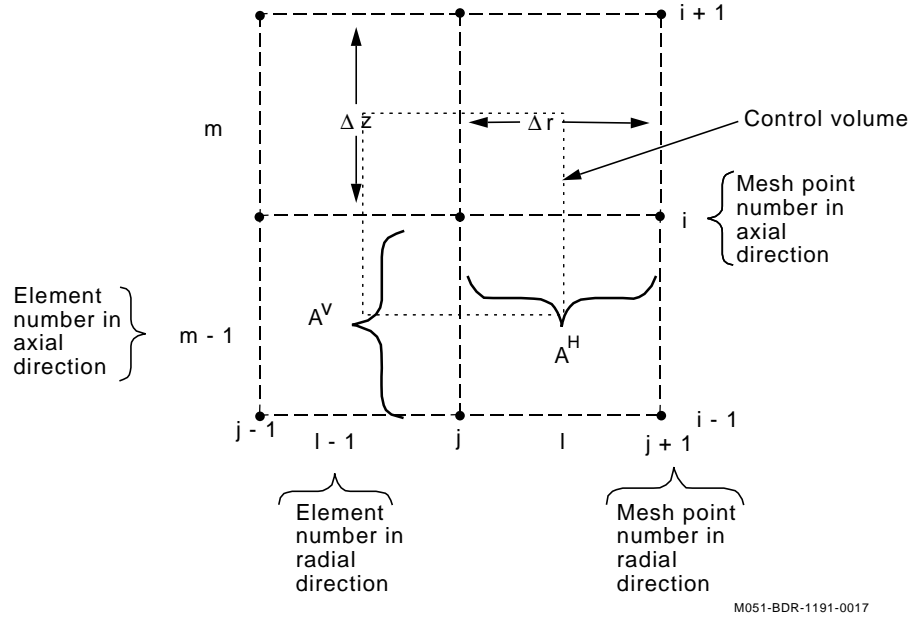
Figure 2-1. Definition of mesh for two-dimensional heat conduction.

For an element surrounding the interior point (i,j), the volume integrals of the volumetric heat capacitance and volumetric heat source can be written as

$$G_{ij} = \left(\int_v \rho c_p (T, r, z) \, dv \right)_{i,j}$$

$$= \frac{1}{4} \left(\rho c_{p_{l-1, m-1}} V_{l-1, m-1} + \rho c_{p_{l-1, m}} V_{l-1, m} \right) + \frac{1}{4} \left(\rho c_{p_{l, m-1}} V_{l, m-1} + \rho c_{p_{l, m}} V_{l, m} \right) . \tag{2-3}$$

$$Q_{ij} = \left(\int_v Q_v (T, r, z) \, dv \right)_{i,j}$$

$$= \frac{1}{4} \left(Q_{l-1, m-1} V_{l-1, m-1} + Q_{l-1, m} V_{l-1, m} + Q_{l, m-1} V_{l, m-1} + Q_{l, m} V_{l, m} \right) . \tag{2-4}$$

Here the subscripts l and m denote the mesh cell with element numbers l and m in the radial and axial direction, respectively (see Figure 2-1). By replacing the time derivative and spatial derivatives in Equation (2-2) by backward differencing and central differencing, respectively, the following is obtained:

$$\frac{G_{i,j} (T_{i,j}^{n+1} - T_{i,j}^{n})}{\Delta t} = A_{i,j}^{L} (T_{i-1, j} - T_{i, j}) + A_{i,j}^{R} (T_{i+1, j} - T_{i, j})$$

$$+ A_{i,j}^{T} (T_{i, j+1} - T_{i, j}) + A_{i,j}^{B} (T_{i, j-1} - T_{i, j}) + Q_{i,j} + Q_s \delta_{i-I} \delta_{j-J} \tag{2-5}$$

where

$$A_{i,j}^{L} = \frac{k_{l-1,m-1}A_{l-1,m-1}^{V}}{2\Delta r_{l-1,m-1}} + \frac{k_{l-1,m}A_{l-1,m}^{V}}{2\Delta r_{l-1,m}} \qquad (2\text{-}6)$$

$$A_{i,j}^{R} = \frac{k_{l,m-1}A_{l,m-1}^{V}}{2\Delta r_{l,m-1}} + \frac{k_{l,m}A_{l,m}^{V}}{2\Delta r_{l,m}} \qquad (2\text{-}7)$$

$$A_{i,j}^{T} = (k_{l-1,m}A_{l-1,m}^{H} + k_{l,m}A_{l,m}^{H}) / (2\Delta z_{m}) \qquad (2\text{-}8)$$

$$A_{i,j}^{B} = (k_{l-1,m-1}A_{l-1,m-1}^{H} + k_{l,m-11}A_{l,m-1}^{H}) / (2\Delta z_{m-1}) \qquad (2\text{-}9)$$

$$\delta_{i-l} = 1, i = l \ (0, i \neq l) \qquad (2\text{-}10)$$

$$\delta_{j-J} = 1, j = J \ (0, j \neq J) \qquad (2\text{-}11)$$

l, J	=	the total number of mesh points in the axial and radial directions, respectively
A^{V}	=	surface area weighting factor in the vertical direction for the given mesh cell
A^{H}	=	surface area weighting factor in the horizontal direction for the given mesh cell

The superscript $n + 1$ for the temperatures on the right-hand side of the difference equation, Equation (2-5), has been suppressed. The thermal properties and heat source terms are treated implicitly. This is accomplished by first solving the i multiplied by j difference equations using the alternating direction implicit (ADI) numerical scheme described in Section 2.3. The updated temperature at the current time level $n + 1$ is then used to recompute the thermal properties and the heat source term. The difference equations are then solved again to give a new updated temperature. This iterative process is terminated when the maximum of the absolute value of the differences between the two successive updated temperatures at all the mesh points is within a 10 K tolerance. The heat sink term is treated explicitly.

2.3   The Alternating Direction Implicit Method

If the system of difference equations are solved exactly, then the method is known as the fully implicit method. Because this involves the solution of a block tridiagonal system of equations, it is in general more cost effective to use the ADI method used in the code. This involves solving the system using only one sweep of the alternating direction iterative method. Because the method can be viewed as a fractional step method for solving Equation (2-1), it has the same order of accuracy as the fully implicit method and it is also unconditionally stable. Specifically, the method can be presented as follows. Form the following equation at each mesh point along each column j (j = 1,...J):

$$2 \frac{G_{i,j} \left(T_{i,j}^{n+\frac{1}{2}} - T_{i,j}^{n} \right)}{\Delta t} = A_{i,j}^{L} \left(T_{i-1,j}^{n} - T_{i,j}^{n} \right) + A_{i,j}^{R} \left(T_{i+1,j}^{n} - T_{i,j}^{n} \right) \tag{2-12}$$

$$+ A_{i,j}^{T} \left(T_{i,j+1}^{n+\frac{1}{2}} - T_{i,j}^{n+\frac{1}{2}} \right) + A_{i,j}^{B} \left(T_{i,j-1}^{n+\frac{1}{2}} - T_{i,j}^{n+\frac{1}{2}} \right) + Q_{i,j} + Q_{s}\delta_{j-J}. \tag{2-13}$$

This gives rise to the following tridiagonal system of equations

$$A\overline{T}^{n+\frac{1}{2}} = B(\overline{T}^{n}) \tag{2-14}$$

which is solved for

$$T_{i,j}^{n+\frac{1}{2}}, i = 1 \text{ to } I \tag{2-15}$$

for each column j. This is followed by another fractional time step that completes the time-step advancement by performing a row inversion for each row as follows. Form the following equation at each mesh point along each row i (i = 1,....,I):

$$2 \frac{G_{i,j} \left(T_{i,j}^{n+1} - T_{i,j}^{n+\frac{1}{2}} \right)}{\Delta t} = A_{i,j}^{L} \left(T_{i-1,j}^{n+1} - T_{i,j}^{n+1} \right) + A_{i,j}^{R} \left(T_{i+1,j}^{n+1} - T_{i,j}^{n+1} \right) \tag{2-16}$$

$$+ A_{i,j}^{T} \left(T_{i,j+1}^{n+\frac{1}{2}} - T_{i,j}^{n+\frac{1}{2}} \right) + A_{i,j}^{B} \left(T_{i,j-1}^{n+\frac{1}{2}} - T_{i,j}^{n+\frac{1}{2}} \right) + Q_{i,j} + Q_{s}\delta_{i-I}. \tag{2-17}$$

Then solving the following tridiagonal system of equations

$$A'\overline{T}^{n+1} = B' \left(\overline{T}^{n+\frac{1}{2}} \right) \tag{2-18}$$

for the updated temperatures $T_{i,j}^{n+1}$ at the time level $n + 1$ for each row i.

2.4   Matrix Methods

The tridiagonal system of Equations (2-14) or (2-18) can be solved by either by Gaussian elimination methods or odd even reduction methods.

The Gaussian elimination method used in the two-dimensional heat conduction solver of the code is known as the UL factorization method, which is a variant of the more familiar LU factorization method.

The matrix A in the matrix Equation (2-14) or (2-18) is factored into the product of an upper-triangular matrix (U) and a lower-triangular matrix (L) as follows:

$$A = \begin{bmatrix} b_1 & c_1 & 0 & 0 \\ a_2 & b_2 & c_2 & 0 \\ 0 & a_{n-1} & b_{n-1} & c_{n-1} \\ 0 & 0 & a_n & b_n \end{bmatrix} = \begin{bmatrix} G_1 & c_1 & 0 & 0 \\ 0 & G_2 & c_2 & 0 \\ 0 & 0 & G_{n-1} & c_{n-1} \\ 0 & 0 & 0 & G_n \end{bmatrix}\begin{bmatrix} 1 & 0 & 0 & 0 \\ E_2 & 1 & 0 & 0 \\ 0 & E_{n-1} & 1 & 0 \\ 0 & 0 & E_n & 1 \end{bmatrix} = UL . \tag{2-19}$$

It is easily verified that

$$G_n = b_n$$

$$E_n = a_n/G_n$$

$$G_j = b_j \;-\; c_j E_{j+1}, j = 1,....,n-1$$

$$E_j = a_j/G_j .$$

On the other hand, if $Uy = r$, where r is the right hand side of the matrix equation $Ax = r$, the result is

$$y_n = r_n/G_n$$

$$y_j = (r_j \;-\; c_j y_{j+1})/G_j, j = 1,.....,n-1 .$$

The solution of $Ax = r$ can therefore proceed as follows.

    1.   Factor A into UL.

    2.   Solve $Uy = r$

    3.   Solve $Lx = y$ for the solution x.

If only the matrix equation $Ax = r$ is solved for one right-hand side vector r for a given matrix A, then Steps 1 and 2 can be combined to give the following algorithm.

1. Solve for y in Step 2 above directly by setting

$$a_n = a_n/b_n$$

$$r_n = r_n/b_n$$

$$a_j = a_j/(b_j \;-\; a_{j+1}c_j), j = 1,....,n-1$$

$$r_j = (r_j \;-\; c_j r_{j+1})/(b_j \;-\; a_{j+1}c_j), j = 1,....,n-1 .$$

The updated a_j and r_j are the E_j and y_j described in steps 1 and 2 above.

2. Back solve for x by solving $Lx = y$ as follows:

$$x_1 = r_1$$

$$x_j = r_j \quad - \quad a_j x_{j-1}, \; j = 1,....,n-1 \; .$$

In the code, the above procedure is vectorized by carrying out steps 1 and 2 in the above algorithm simultaneously for all the columns (rows) during the column (rows) inversion step in the ADI schemes. This procedure is most efficient during the column (row) inversion step when there are many rows (columns) and only a few columns (rows). In general, the odd even cyclic reduction (OECR) algorithm is more competitive on vector machines such as the Cray.

2.5   OECR Algorithm

Solving the tridiagonal system of equations $Ax = r$ with the $j - 1, j, j + 1$ rows displayed, the following applies:

$$a_{j-1}x_{j-2} + b_{j-1}x_{j-1} + c_{j-1}x_j = r_{j-1}$$

$$a_j x_{j-1} + b_j x_j + c_j x_{j+1} = r_j$$

$$a_{j+1}x_j + b_{j+1}x_{j+1} + c_{j+1}x_{j+2} = r_{j+1} \; .$$

If the $j - 1$ and $j + 1$ rows are multiplied with $-a_j/b_{j-1}$ and $-c_j/b_{j+1}$, respectively, and added to the j row, the references to the $j - 1$ and $j + 1$ variables in the j row are eliminated. In general, if the odd numbered rows are multiplied by suitable scalars and added to the even numbered rows, then the references to the odd numbered variables in the even numbered rows disappear. This permits a large system of equations to be eventually reduced to a system that consists of only one or two equations. The operation count, however, is 17N vs. 8N for Gaussian elimination methods, where N is the order of the matrix so that the method is not competitive on serial machines. On vector machines such as the Cray, the method is known to be several times faster than Gaussian elimination methods for large N, with break even occurring at N = 100. When used with the ADI scheme, the secret of success is to form long vectors of length IJ where I is the number of axial levels and J is the number of radial nodes. The OECR algorithm is then used to reduce the matrix problem on all the mesh points to a system of either I times one or two equations or J times one or two equations depending on whether the ADI sweep is in the axial or radial direction. Note that the variables at each row (column) during the ADI row (column) inversion are not coupled with that at adjacent rows (columns,) so that the I (or J) times 1 or 2 equations can be solved simultaneously at all the I rows or J columns. Hence, the vector length for all the vectors during the OECR algorithm never falls below I or J and the method is therefore significantly more efficient than the usual OECR algorithm when the vector length eventually becomes 1 or 2. This procedure is most easily implemented when the column (row) length is equal to 2^n or 3 multiplied by 2^n when column (row) inversion is performed in the ADI scheme. In the code, odd even reduction is used when the above mentioned criteria are satisfied. Otherwise, the vectorized Gaussian elimination method is used.

2.6   Volume Averaging

Effective material properties and effective volumetric heat generation are applied over a control volume. The following volumetric averaging is applied.

$$(\rho c_p)_{eff} = \frac{\int_V \rho c_p dV}{\int_V dV} \qquad (2\text{-}20)$$

$$\left(\frac{1}{k}\right)^n_{eff} = \frac{\int_V \frac{1}{k} dV}{\int_V dV} \qquad (2\text{-}21)$$

$$Q_{v_{eff}} = \frac{\int_V Q_v dV}{\int_V dV} \ . \qquad (2\text{-}22)$$

3. MATERIAL OXIDATION MODEL

The material oxidation model calculates the generation of heat, production of hydrogen, and reduction of steam. This model uses oxidation rate equations with material temperatures defined by the component heat conduction model.

3.1 Parabolic Rate Equation

Material oxidation is assumed to behave following the parabolic rate equation

$$\frac{d\delta}{dt} = \frac{A}{\delta} e^{(\frac{-B}{T})} \tag{3-1}$$

where

δ	=	weight gain or layer thickness (kg/m^2 or m)
T	=	temperature (K)
t	=	time (s)
A,B	=	parabolic rate constants taken from MATPRO.

For a constant temperature, this equation can be integrated over the time interval, Δt, to give

$$\delta^2 - \delta_o^2 = 2Ae^{(\frac{-B}{T})} \Delta t \tag{3-2}$$

where δ_o is the value at the beginning of the time interval. For zircaloy, three separate parabolic equations are solved for oxygen weight gain and the growth of the α and ZrO_2 layers. For all other materials, only the oxygen weight gain is computed.

The oxidation heat generation rate, Q_{ox}, is computed from the weight gain,

$$Q_{ox} = \frac{M}{M_{(O_2)}} h_r S \frac{dw}{dt} \tag{3-3}$$

where

$M_{(O_2)}$	=	molecular weight of oxygen
M	=	molecular weight of the material
h_r	=	heat of reaction in J/kg of material reacted
S	=	original surface area (m^2)
w	=	oxygen weight gain per unit surface area (kg/m^2).

The original surface area is based on the area prior to any oxidation and does include the effect of deformation.

The hydrogen production rate, $\dot{H}_2$, and steam removal rate, $\dot{H}_2O$, are also computed from the oxygen weight gain and are given by

$$\dot{H}_2 \;=\; \frac{1}{8}S\frac{dw}{dt} \tag{3-4}$$

$$\dot{H}_2O \;=\; \frac{9}{8}S\frac{dw}{dt}\;. \tag{3-5}$$

The oxidation process is subjected to three limits. First, the oxidation is terminated when the material is fully oxidized, in the case of zircaloy when material is converted to ZrO_2 and for stainless steel when the iron is converted to FeO_2. The resulting limits on oxygen uptake can then be expressed as

$$w \leq \frac{M_{o_2}}{M}\rho\frac{V}{S} \tag{3-6}$$

where M_{o_2} is the molecular weight of oxygen, M is the molecular weight of material, and ρ and V are the density and volume of the material, respectively. Second, the oxidation rate is limited by the availability of steam. That is,

$$\frac{dw}{dt} \leq \frac{8}{9}\frac{\dot{m}}{S} \tag{3-7}$$

where $\dot{m}$ is the mass flow rate of the steam available to the oxidizing surface. Finally, oxidation is limited by the diffusion of water vapor. The water vapor molar mass flow rate $N_{(H_2O)}$ is driven by the partial pressure of the water vapor, which can be written as

$$\frac{N_{(H_2O)}}{A} \;=\; B_{(H_2O)}P_{(H_2O)} \tag{3-8}$$

where

$N_{(H_2O)}$	=	molar mass flow rate (kg-mole/s)
A	=	surface area (m^2)
$B_{(H_2O)}$	=	mass transfer coefficient (kg-mole/s $\cdot$ m^2 $\cdot$ Pa)
$P_{(H_2O)}$	=	partial pressure of water vapor (Pa).

Using a mass/heat transfer analogy assuming Colburn j factors for heat and mass transfer are equal,[13] then

$$\frac{Nu}{RePr^{0.33}} \;=\; \frac{Sh}{ReSc^{0.33}} \tag{3-9}$$

where

Nu	=	Nusselt number, $\dfrac{hL}{k_{(H_2O)}}$
$k_{(H_2O)}$	=	thermal conductivity of water vapor (W/m $\cdot$ K)
h	=	convective heat transfer coefficient (W/m$^2 \cdot$ K)
L	=	characteristic length (m)
Sh	=	Sherwood number $\dfrac{B_{(H_2O)}RTL}{D_v}$
D_v	=	mass diffusivity (m^2/s)
R	=	gas constant (Pa$\cdot$m^3/kg-mole $\cdot$ K)
T	=	temperature (K)
Pr	=	Prandtl number $\dfrac{C_{p(H_2O)}\mu_{(H_2O)}}{k_{(H_2O)}}$
$C_{p(H_2O)}$	=	specific heat (J/kg $\cdot$ K)
$\mu_{(H_2O)}$	=	viscosity of water vapor (kg/s $\cdot$ m)
Sc	=	Schmidt number, $\dfrac{\mu_{(H_2O)}}{\rho_{(H_2O)}D_v}$
$\rho_{(H_2O)}$	=	density of water vapor (kg/m^3).

Using the mass/heat transfer analogy, the rate of oxygen uptake for an oxidizing surface becomes limited by

$$\frac{dw}{dt} \leq \frac{m_{O_2}}{2m_{H_2O}}\frac{N_{H_2O}}{A} = \frac{8}{9}\left(\frac{hD_v}{k_{(H_2O)}}\right)\left(\frac{P_{(H_2O)}}{RT}\right)\left(\frac{k_{(H_2O)}}{\rho_{(H_2O)}C_{p(H_2O)}D_v}\right) \tag{3-10}$$

where the mass diffusivity is calculated by[14]

$$D_v = (1-X)\frac{\mu_{(H_2O)}RT}{PM_{(H_2O)}} + \sum_{i=1}^{n}X_i\frac{\mu_i RT}{PM_i} \tag{3-11}$$

where

$M_{(H_2O)}$	=	molecular weight of the water vapor
M_i	=	molecular weight of the gas specie i
$\mu_{(H_2O)}$	=	molecular viscosity of the water vapor (kg/m $\cdot$ s)
μ_i	=	molecular viscosity of the gas specie i (kg/m $\cdot$ s)
P	=	total pressure (Pa)
X_i	=	i-th noncondensable gas quality
X	=	total noncondensable quality, $\sum_{i=1}^{n}X_i$
n	=	number of noncondensable gas species.

Important assumptions are made which are dependent upon the type of component or structures being modeled. The assumptions are:

- The surface areas and material volumes can either be based on cylindrical or slab geometries.

- Volume changes due to oxidation are considered only for zircaloy.

- For structures with multiple material layers, including layers of frozen material, it is assumed that outer layers oxidize completely prior to any oxidation of inner layers. It is also assumed that once the outer layers are oxidized, they do not inhibit the flow of steam to inner layers so that the parabolic rate equations for the inner layers are solved, ignoring the presence of any outer layers.

- For ballooned and ruptured fuel rod cladding or input defined failure of the inner layer of a shroud, the oxidation rates are doubled in the failed regions, assuming the inside and outside of the cladding or shroud inner layer oxidize at the same rates.

3.2 Enhanced Oxidation Due to Shattering of Oxidized Fuel Rod Cladding

Shattered oxidized cladding debris has been observed, for example, in LOFT LP-FP-2, SFD-ST, and CORA-12 experiments,[15] where each core was subjected to reflood. Post irradiation examination of the LOFT experiment revealed cladding remnants scattered through the upper blockage which were formed during the reflood.[16]

Direct comparison of comparable experiments with and without reflood is possible using data from the CORA facility. Table 3-1 shows the post-test condition of simulator rod cladding after CORA-12, which was subjected to a reflood, while Table 3-2 shows the post-test condition of the simulator rod cladding after CORA-5, which did not experience reflood. These tables list the number of rods at a given location and cladding end state condition. Table 3-1 shows that after the CORA-12 reflood a significant portion of the cladding was broken or missing, while Table 3-2 shows that CORA-5, with no reflood, experienced no extensive shattering, since shattering would have shown broken shards or missing cladding. Comparison of CORA-5 (no reflood) and CORA-12 (with reflood) indicates that cladding was mechanically broken during the quench. Apparently, the cladding was brittle due to oxidation; thermal stresses induced by reflood caused the exposed surfaces to shatter, resulting in exposure of fresh metal that oxidized immediately.[17] This mechanism of oxidation also helps explain the surge in temperatures and hydrogen production during reflood.

This model is intended to only increase the oxidation rate due to the shattering of fuel rod cladding during reflood conditions. This model is not activated by default, and must be initiated through user input. In addition, a RELAP5 logical trip is also available on input, which, when specified, will provide enhanced oxidation on all fuel rod components at all axial nodes.

Enhanced oxidation will be calculated when the outer oxide layer of a fuel rod component is considered to shatter. This will occur when the following criteria[15] are met:

- β phase thickness less than or equal to 0.1 mm

- Cooling rate greater than 2 K/s for four consecutive time steps within the temperature range of 1,150 to 1,560 K.

In the implementation of the enhanced oxidation model, the oxidation model was modified to track two oxide histories, a physical oxide history and an effective oxide history. The physical oxide history was unchanged and is used for all the mass balance and heat conduction modeling. An effective oxide history was added as two independent variables, the effective oxide thickness and the effective oxygen weight gain. These variables are, of course, tracked for each axial node of each component and represent, δ, in Equation (3-1). When the reflood criteria are met, the effective oxide thickness is reset to model fresh un-oxidized zircaloy, and the oxygen weight gain is reset to the difference between the physical oxygen weight gain and the oxygen in the removed oxide layer.

Table 3-1. CORA-12 cladding posttest condition.

| | Number of rods | | | | | |
Elevation (mm)	Cladding intact	Cladding missing	Cladding reacted	Cladding flowered	Cladding broken (mechanical)	Absorber rod
51	23	0	0	0	0	2
216	0	9	6	0	8	2
381	0	5	0	18	0	0
503	0	16	0	7	0	0
711	0	19	0	4	0	0
876	2	15	0	6	0	0

Table 3-2. CORA-5 cladding posttest condition.

| | Number of rods | | | | | |
Elevation (mm)	Cladding intact	Cladding missing	Cladding reacted	Cladding flowered	Cladding broken (mechanical)	Absorber rod
95	24	0	0	0	0	1
208	23	0	1	0	0	1
393	0	0	3	21	0	0
408	0	0	2	22	0	0

Table 3-2. CORA-5 cladding posttest condition. (Continued)

	Number of rods					
Elevation (mm)	Cladding intact	Cladding missing	Cladding reacted	Cladding flowered	Cladding broken (mechanical)	Absorber rod
663	0	8	0	16	0	0
853	0	10	0	14	0	0

3.3 Oxidation of Debris

This section describes the model for the oxidation of debris. The oxidation of debris is a continuation of the oxidation that began when the material being oxidized was configured as intact fuel rods. The rate of oxidation of debris is a function of the configuration of the debris. If the debris is in the form of drops that are slumping down the outer surface of fuel rods, the rate of oxidation may be more rapid than when the fuel rod was intact. If the debris is in the form of a horizontal layer of cohesive material, the rate of oxidation in the debris state will be less than when in the intact state due to a large reduction in surface area. In either case the oxidation of debris has the potential of significantly influencing the damage progression and the hydrogen production that occurs during a severe accident.

A model of the oxidation of debris has been developed that is applicable to debris that is composed of a mixture of Zr and UO_2 and to debris in three types of configurations. The three types of configuration are: 1. drops on the surface of fuel rod cladding, 2. layers of solidified debris, and 3. particles of solidified debris. These three configurations of debris are shown in Figure 3-1. The variables calculated by the model are: 1. rate of oxygen weight gain per unit surface area of debris, 2. rate of heat generation per unit surface area of debris, and 3. rate of hydrogen production per unit surface area of debris. These variables are applied by the fuel rod model to calculate the heatup of fuel rods with droplets of debris on the surface or that support a layer of cohesive debris. These variables are applied by the porous debris model to calculate the heatup of porous debris.

The oxidation of debris is represented as a diffusion-controlled process with a parabolic rate law under isothermal conditions. The oxidation process is represented by the equation

$$\frac{dw}{dt} = \frac{k_{eff}}{2w} \tag{3-12}$$

where

w = oxygen weight gain per unit surface area (kg O_2/m^2)

t = time (s)

k_{eff} = effective parabolic constant for oxygen weight gain [$(kg/m^2)^2/s$].

The integration of the above equation with respect to time yields the equation
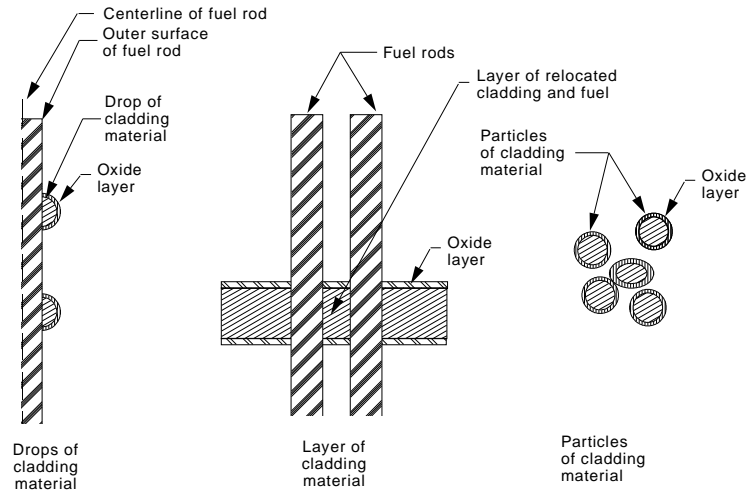
Various configurations of oxidizing debris

M253-BDR-0694-006

Figure 3-1. Various configurations of oxidizing debris.

$$w_1 = (k_{eff}\Delta t + w_0^2)^{0.5} \tag{3-13}$$

where

w_1 = weight gain at end of time step (kg/m^2)

w_0 = weight gain at start of time step (kg/m^2)

Δt = size of time step (s).

The effective parabolic rate constant is determined by interpolation of experimental data. The parabolic rate constants for debris composed of 100% Zr or 100% UO_2 are well-defined by experimental results. For mixtures of Zr and UO_2, however, experimentally determined rate constants are limited. This limitation of experimental results makes it necessary to calculate the rate constants for a mixture of Zr and UO_2 based on an assumption of the relation of the rate constants for a mixture to those for 100% Zr and 100% UO_2. The assumption is made that the rate constant changes linearly with change in mass fraction of UO_2 in the mixture. The rate constant is thus calculated by the equation

$$k_{eff} = (1 - f) \cdot k_{zr} + fk_{UO_2} \tag{3-14}$$

where

f = mass fraction of UO_2 in mixture

k_{zr} = parabolic rate constant for oxidation of Zr [$(kg/m^2)^2/s$]

k_{UO2} = parabolic rate constant for oxidation of UO_2 [$(kg/m^2)^2/s$]

The value of k_{eff} as calculated by Equation (3-14) is in agreement with experimental results[18] for debris temperatures less than 2,000 K. The calculated values of k_{eff} as a function of temperature are compared with experimentally determined values in Figure 3-2. The comparison is shown for a mixture consisting of 85 mol% Zr and 15 mol% UO2, which is the only mixture composition for which experimental results are available. The values of k_{zr} in Equation (3-14) are calculated by the MATPRO function COXWTS and the values for k_{UO2} are calculated by the MATPRO function FOXYK[19]. The variation between calculated and experimental values for temperatures greater than 2,000 K are due to the differences between the parabolic rate constants for pure Zr used in MATPRO (Urbanic-Heidrick for temperatures above 1,850 K) and those measured by Prater-Courtright[18].
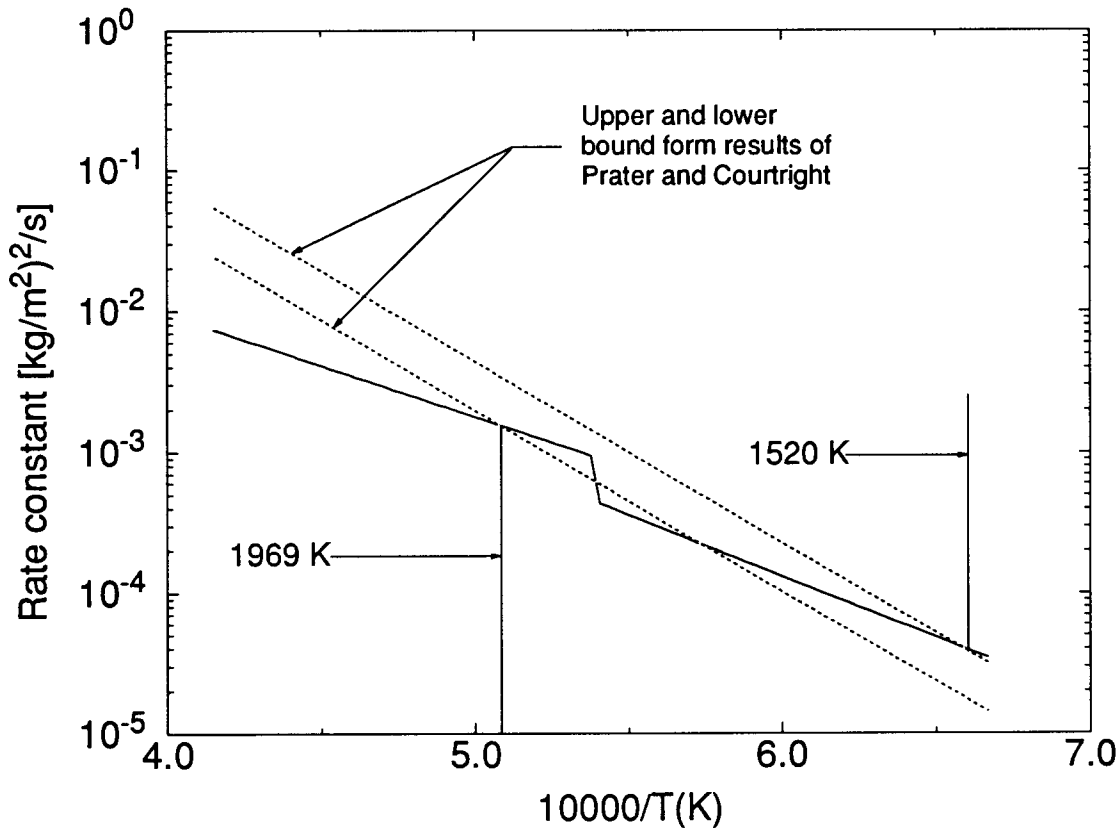
Figure 3-2. Parabolic rate constant for mixture of 85 mol% Zr and 15 mol% UO$_2$.

Heat is produced by the oxidation of a mixture of Zr and dissolved UO$_2$. The heat is produced by the conversion of Zr to ZrO$_2$ and UO$_2$ to U$_3$O$_8$. The rate of heat generation is calculated by the equation

$$Q = \left((1-f) \cdot H_{Zr} \cdot \frac{A_{wZr}}{A_{wO2}} + f \cdot H_{UO_2} \cdot \frac{A_{wU}}{A_{wO_2}} \right) \cdot \left(\frac{w_1 - w_0}{\Delta t} \right) \tag{3-15}$$

where

Q	=	heat generation due to oxidation (W/m^2)
H_{zr}	=	heat of reaction for Zr (6.45×10^6 J/kg of Zr converted to ZrO$_2$)

A_{wZr} =   atomic weight of Zr (91.22)

A_{wO2} =   atomic weight of O_2 (32)

H_{UO2} =   heat of reaction of UO_2 as obtained from MATPRO (1.84×10^5 J/kg of $(UO_2)_3$ converted to U_3O_8)

A_{wU} =   atomic weight of $(UO_2)_3$ (810).

4. FUEL ROD MODELS

4.1 Electrical Heat Generation Model for Fuel Rod Component

This model is used to represent electrically heated fuel rods with a central tungsten heater rod. The total power input is specified by user input, while the axial and temperature dependent power release is calculated by the model.

The electrical heat generation model computes the axial and temperature dependent power release in the heated area of the tungsten heater rod and also includes the effects of the molybdenum electrode and the copper at the top and bottom of the tungsten heater rod. The model first computes the resistance of copper, molybdenum and tungsten. The model currently has the dimensions of the tungsten rod and molybdenum and copper electrodes at the top and bottom of the tungsten heater rod built into the resistance equations. The specific dimensions are based upon the CORA[20] heater rod elements. The resistances are calculated by the equations:

$$R_{Mo} = 2.25 \text{ x } 10^{-2} + 5.36 \text{ x } 10^{-5} \, T_{Mo} + 1.38 \text{ x } 10^{-7} \, T_{Mo}^2 - 2.22 \text{ x } 10^{-11} \, T_{Mo}^3 \; (\Omega \bullet mm^2/m) \tag{4-1}$$

$$R_{Cu} = -7.89 \text{ x } 10^{-3} + 9.90 \text{ x } 10^{-5} \, T_{Cu} - 5.49 \text{ x } 10^{-8} \, T_{Cu}^2 + 3.16 \text{ x } 10^{-11} \, T_{Cu}^3 \; (\Omega \bullet mm^2/m) \tag{4-2}$$

$$R_W(I) = [-0.0261 + 2.63 \text{ x } 10^{-4} T(I) + 2.20 \text{ x } 10^{-8} T(I)] DZ(I)(3.5368 \text{ x } 10^{-2}) \; (\Omega), \, I = 1, 2, ...NAZ \tag{4-3}$$

where

NAZ	=	number of axial levels
DZ(I)	=	height of i-th axial node (m)
T(I)	=	fuel rod centerline temperature at node I (K)
T_{Mo}	=	$0.5[T(NAZ) + 350]$ (K)
T_{Cu}	=	$0.5(T_{Mo} + 350)$ (K)
T	=	fuel center temperature at the 1st axial level (K).

The total resistance is then given by

$$R_t = \sum_{I=1}^{NAZ} R_w(I) + 0.0086 \, (R_{Mo} + R_{Cu}) + 0.0005 \; (\Omega). \tag{4-4}$$

The power per unit length in each axial node is then

$$UNUC(I) = \frac{R_w(I)}{R_t} \frac{P_t}{D_z(I)} \tag{4-5}$$

where P_t is the total input rod power (W).

4.2   Fission Product Release Models

The models described in this section calculate the rate of fission product release from intact fuel rods and rods that have experienced fuel liquefaction or fragmentation. The models also calculate the enthalpy of the released fission products. This description has been divided into three subsections. The first subsection describes the current fission product release models for rods with undisrupted fuel but failed or damaged cladding. The other subsections describe the fission product release during the liquefaction or fragmentation of UO_2 and the enthalpy of released fission products.

4.2.1   Release Model for Intact Fuel

SCDAP/RELAP5 models the release of fission products from the fuel to the gap using a combination of a theoretical model developed by Rest et al.,[21] to treat the release of xenon, krypton, cesium, iodine, and tellurium from solid fuel, and empirical models to treat other fission products.[a]

The theoretical model is a simplified version of the FASTGRASS code that has been used for predicting the behavior of fission gas in UO_2-based fuels during steady state and transient conditions.[21,22,23,26] Fission products released from the fuel are assumed to reach the fuel surface by successively migrating from the grains to grain faces and then to the grain edges, where the fission products are released through a network of interconnected tunnels of fission gas induced and fabricated porosity. This model treats the production of gas from fissioning nuclei, bubble nucleation and resolution, bubble migration, bubble coalescence, gas bubble and channel formation on grain faces, interlinked porosity on grain edges, grain boundary microcracking, and grain growth and grain boundary sweeping.

The specific models used for xenon, krypton, cesium, iodine, and tellurium are described by Rest.[21,22,23,21] For completeness, an example of the equations used to describe the diffusion of gases to grain boundaries is described below. The concentration of atoms, C_g, within the spherical grain satisfies the equation

$$\frac{\partial C_g}{\partial t} = \frac{1}{r^2}\frac{\partial}{\partial r}\left[D_g r\frac{\partial C_g}{\partial r}\right] + K_g \tag{4-6}$$

where

$$D_g \qquad = \qquad \text{atom diffusion coefficient}$$

$$K_g \qquad = \qquad \text{the rate of generation of atoms.}$$

In general, Equation (4-6) is solved with the boundary conditions

$$C_g = 0 \text{ at } t = 0 \text{ for } 0 \le r \le \frac{d_g}{2} \tag{4-7}$$

---

a. The theoretical model is based upon PARAGRASS Version 50531, with the cesium iodide chemistry model deactivated because of an error in that version of PARAGRASS that resulted in an error in the iodine release.

$$C_g = 0 \text{ at } r = \frac{d_g}{2} \text{ for } t_o \le t \le t_o + h \tag{4-8}$$

$$\frac{\partial C_g}{\partial r} = 0 \text{ at } r = 0 \text{ for } t_o \le t \le t_o + h \tag{4-9}$$

where

d_g =   grain diameter

h   =   time interval between times t_o and $t_o + h$.

The diffusive flow of the fission gas bubbles to the grain boundaries is also governed by Equation (4-6). For this case, it is assumed that gas bubbles are not being nucleated and are essentially noninteracting.

The coupling of the diffusive flow problem to other processes affecting fission gas behavior (e.g., gas atom resolution, gas atom trapping by gas bubbles) is accomplished by solving equations of the form

$$\frac{dY_i}{dt} = -a_i Y_i^2 - b_i Y_i + C_i \tag{4-10}$$

where

Y_i =   density of intragranular gas atoms (bubbles)

$a_i Y_i^2$ =   rate at which gas atoms (bubbles) are lost owing to gas bubble nucleation (coalescence)

$b_i Y_i$ =   rate at which gas atom (bubbles) are lost owing to diffusive flow and diffusion into gas bubbles (gas atom resolution)

C_i =   rate at which gas atoms are gained owing to gas atom resolution and fission of uranium nuclei (i.e., the rate gas bubbles are gained owing to bubble nucleation and diffusion of gas atoms into bubbles).

A more detailed description of the above variables is also given in Table 4-1.

Equation (4-6) is discretized in time using backward Euler approximation to give the following equation:

$$\frac{1}{r^2}\frac{\partial}{\partial r}\left[D_g r^2 \frac{\partial C_g}{\partial r}\right] - \frac{C_g}{h} + \frac{C_g(t-h)}{h} + K_g = 0 . \tag{4-11}$$

By applying a variational principle and setting the first variation to zero,

$$\int_0^{(\frac{1}{2}D_g)} 4\pi\left[0.5 D_g\left(\frac{\partial C_g}{\partial r}\right)^2 + \frac{C_g 2}{2h} - \frac{C_g(t-h)}{h} + K_g C_g\right] r^2 dr = 0 . \tag{4-12}$$

Table 4-1. Definition of variables in Equation 4-10.

Y_i	$a_i Y_i^2$	$b_i Y_i$	C_i
Density of intragranual gas atoms and VFPs	Rate at which gas atoms are lost owing to gas bubble nucleation	Rate at which atoms and VFPs are lost owing to diffusive flow to the grain boundaries, grain boundary sweeping, diffusion into gas bubbles, and chemical reactions	Rate at which atoms and VFPs are gained owing to an atom resolution, a fission of uranium nuclei, and chemical reaction
Density of intragranular gas bubbles	Rate at which gas bubbles are lost owing to bubble coalescence	Rate at which gas bubbles are lost owing to diffusive flow to the grain boundaries, grain boundary sweeping, and gas atom resolution	Rate at which gas bubbles are gained owing to bubble nucleation and diffusion of gas atoms into bubbles
Density of grain-face gas bubbles and VFPs	Rate at which gas bubbles are lost owing to bubble coalescence	Rate at which gas bubbles and VFPs are lost owing to diffusion to grain edges, formation of grain channels, microcracking, and chemical reactions	Rate at which gas bubbles and VFPs are gained owing to intragranular migration to grain faces, and chemical reactions.
Density of grain-edge gas bubbles and VFPs	Rate at which gas bubbles are lost owing to bubble coalescence	Rate at which gas bubbles and VFPs are lost owing to long-range grain-edge bubble interconnection, microcracking, and chemical reactions	Rate at which gas bubbles and VFPs are gained owing to migration of grain-face fission products to grain edges and chemical reactions

The spherical grain is then split into two concentric regions of approximately equal volume. In each region, the gas concentration is represented by a quadratic function. In the Central Region I, the concentration function is constrained to have $\partial/\partial r(C_g) = 0$ at $r = 0$. In the Outer Region II, the concentration function is constrained to have a value of $C_g = 0$ at $r = d_g/2$. The two functions are also constrained to be continuous at the common boundary of the two regions. This leaves three free parameters, C_1, C_2, and C_3. These are chosen to be gas-atom concentrations at positions corresponding to the midpoint radius of Region 1, the boundary between the regions, and the midpoint radius of Region II, respectively.

Hence, for Region I,

$$C_g = C_1 \frac{(0.64 - a^2)}{0.48} + C_2 \left[a^2 - \frac{0.167}{0.48} \right] \qquad (4\text{-}13)$$

and for Region II,

$$Cg = 5C_2(10a^2 - 19a + 9) + 10C_3(18a - 10a^2 - 8) \qquad (4\text{-}14)$$

where a is equal to $2r/dg$. Equations (4-13) and (4-14) are substituted for C_g in Equation (4-12) and an extremum is found by differentiating with respect to C_1, C_2, and C_3 in turn. A set of three linear equations is thus obtained. The solution of this set of equations expressed C_i in terms of D_g, d_g, and q_j. The q_j's, j = 1,2,...13, are integrals which, when directly evaluated, are $q_1 = 4.552,..., q_{13} = 0.1083$.
The flux of gas atoms to the boundary (in units of atoms/cm^3•s) is given by

$$J = -6 \left(\frac{D_g}{d_g} \right) \frac{\partial C_g}{\partial r} \bigg|_{r = d_g/2} . \qquad (4\text{-}15)$$

This term J is one of the terms in the expression for the rate at which gas atoms are lost, given by the term $b_i Y_i$ in Equation (4-10). It is determined by Wood and Mathews[27] that the best expression for the average concentration within the grains, $C_g(av)$, is given by

$$C_g(av) = 0.2876C_1 + 0.2176C_2 + 0.4216C_3 . \qquad (4\text{-}16)$$

At the end of an iteration, the concentrations C_1, C_2, and C_3 in Equation (4-15) are scaled by imposing the condition that the average concentration equals that calculated by use of Equation (4-10), i.e.,

$$C_g(av) = Y_i . \qquad (4\text{-}17)$$

The modified C_1, C_2, and C_3 then become the initial values of these concentrations [i.e., $C_1(t-h)$, $C_2(t-h)$, $C_3(t-h)$] to be used for the next iteration. The diffusion of gas bubbles is treated analogously to that for fission gas atoms, but with $K_g = 0$ in Equation (4-11).

The elemental fission yields of the fission gases are xenon (0.2635), krypton (0.0465), cesium (0.1507), iodine (0.011), and tellurium (0.02519). These quantities are in units of atoms per fission event. Multiplication by fission rate per unit volume gives the fission gas generation rate in units of atoms/s/m^3. Because very little fission gas is released during steady-state calculations, the calculation of initial inventories is dominated by the fission gas generation rate.

This version of the PARAGRASS model differs from the older versions. Two options for grain growth are included:

1.   An empirical law is used to calculate grain growth; grain boundary sweeping of fission

products is proportional to the volume swept by the growing grains.

2.   A theoretical grain growth model is fully coupled to the grain boundary sweeping model.

A model for the effect of UO_2 oxidation is included, using a grain growth activation energy appropriate for stoichiometric UO_2.

The fission product tellurium is included with iodine, cesium, and cesium iodide. The effects of the oxidation state of the cladding on tellurium release are included (i.e., cladding not completely oxidized and cladding oxidized more than 90%). When the cladding is not more than 90% oxidized, only 1/40 of the tellurium release is allowed to come out. Otherwise, all of the tellurium release comes out.

Theoretical models to calculate the instantaneous rate of change of the bubble radius have been included. Previous versions of PARAGRASS handled the nonequilibrium growth of gas bubbles by modifying the bubble coalescence rates by an appropriate factor. Equilibrium values of the bubble radius were used in the calculation of various material properties, e.g., the calculation of bubble diffusivities.

The model for the behavior of gas bubbles on grain surfaces has been improved. In the previous version, the effect of external stress on intragranular bubble growth was inadvertently decoupled.

A more efficient method for the time integration of Equation (4-10) is used. After burst of fuel rods, it is assumed that cesium and iodine will combine to form cesium iodide, with any leftover cesium reacting with water on release from the gap to form cesium hydroxide or any leftover iodine being release as I_2. This assumption is based on fission product chemical states.[28]

The interaction of cesium with water releases one-half mole of hydrogen gas per mole of cesium hydroxide. This is accounted for in the model by adding the additional hydrogen release to the total release of noncondensable gases. This reaction also releases energy that is accounted for in the enthalpy of the released gap gases.

Release of less volatile fission products is based on the CORSOR-M model in NUREG/CR-4173.[29] It assumes a first order release rate from each node for each species such that

$$FP = FFP \cdot (1 - e^{[(-FRC)(DTIME)]}) \tag{4-18}$$

where

    FFP   =   mass of the species present at the node at the start of the time step

    FRC   =   fractional release rate coefficient

The value of FRC is given by an Arrhenius type equation of the form:

$$FRC = KO(I) \cdot e^{\left(\frac{-Q(I)}{1.987 \times 10^{-3}T}\right)} \tag{4-19}$$

where

KO(I)

and

Q(I) = species-dependent constants

T = nodal absolute temperature

$1.9873 \times 10^{-3} =$ value of the gas constant multiplied by a unit conversion factor.

The values of the constants KO and Q are given in Table 4-2.

The tin release rate is calculated by the equation

$$\frac{dm}{dt} = K_w [C_{eq} - C] \tag{4-20}$$

where

$\frac{dm}{dt}$ = release rate of tin vapor from the cladding surface ($kg/m^2 \cdot s$)

K_w = mass transfer coefficient (m/s)

C_{eq} = equilibrium concentration of tin vapor at the surface of the cladding (kg/m^3)

C = concentration of tin in the bulk coolant (kg/m^3).

Table 4-2. Constants KO and Q in release rate coefficients taken from NUREG/CR-4173.

Species	KO (min^{-1})	Q (kcal/mol)
UO_2	1.46 E7	143.1
Zr	2.67 E8	188.2
Sn (clad)	5.95 E3	70.8
Fe	2.94 E4	87.0
Ru	1.62 E6	152.8
Z(clad)	8.55 E4	139.5
Ba	2.95 E5	100.2
Sr	4.40 E5	117.0
Te	2.00 E5	63.8
Ag	7.90 E3	61.4
Cs*	2.00 E5	63.8

Table 4-2. Constants KO and Q in release rate coefficients taken from NUREG/CR-4173. (Continued)

Species	KO (min^{-1})	Q (kcal/mol)
I*	2.00 E5	63.8

The mass transfer coefficient is given by the correlation

$$K_w = 0.023 \, (\text{Re})^{0.83} \, (\text{Sc})^{0.33} \frac{D_r}{D_e} \tag{4-21}$$

where

Re	=	Reynolds number of bulk coolant
Sc	=	Schmidt number
D_r	=	diffusivity of tin in bulk coolant (m^2/s)
D_e	=	equivalent diameter of flow channel (m).

The variable D_r is calculated by the equation

$$D_r = 9.8 \cdot 10^{-5} \, (T_B) \frac{1.75}{p} \tag{4-22}$$

where

T_B	=	temperature of bulk coolant (K)
p	=	pressure of bulk coolant (Pa).

The variable C_{eq} is calculated by the equation

$$C_{eq} = 118.69 P_{sn} \, (8.31 \cdot 10^3 T_{zr} + 1.63 \cdot 10^{-2} P) \tag{4-23}$$

where

P_{sn}	=	equilibrium partial pressure of tin (Pa)
T_{zr}	=	cladding surface temperature.

The variable P_{sn} is calculated by the equation

$$P_{sn} = f_{sn} e^{\left(\frac{-2.847 \times 10^4}{T_{zr}} + 4.548 \ln (T_{zr}) - 14.31\right)} \tag{4-24}$$

where f_{sn} is the concentration of tin in the cladding (atomic fraction).

The variable f_{sn} is calculated by the equation

$$f_{sn} = \frac{\left[\dfrac{M_{sn}}{A_{sn}}\right]}{\left[\dfrac{M_{sn}}{A_{sn}}\right] + \left[\dfrac{M_{zr}}{A_{zr}}\right]} \qquad (4\text{-}25)$$

$$f_{sn} = \frac{M_{sn}}{M_{sn} + \left[\dfrac{A_{sn}}{A_{zr}}\right]\rho_{zr}\left[h_z - \dfrac{m_{sn}}{\rho_{sn}}\right]} \qquad (4\text{-}26)$$

where

$\quad M_{sn}$ $\quad=\quad$ mass of tin remaining in the cladding per unit surface area (kg/m^2)

$\quad M_{zr}$ $\quad=\quad$ mass of unoxidized cladding per unit surface area (kg/m^2)

$\quad A_{sn}$ $\quad=\quad$ atomic weight of tin (118.69 kg/kg-mole)

$\quad A_{zr}$ $\quad=\quad$ atomic weight of cladding zirconium (91.22 kg/kg-mole)

$\quad \rho_{zr}$ $\quad=\quad$ density of zirconium (kg/m^3)

$\quad h_{zr}$ $\quad=\quad$ thickness of unoxidized cladding (m).

The control rod release is calculated in the code based on the following method, described also in NUREG/CR-4173.[29]

At 1,673 K, the control rods are assumed to fail; 5% of the inventory of silver and 50% of the cadmium are released from the nodes reaching this temperature.

From 1,673 to 2,573 K, the cumulative fraction of the inventory released is calculated according to:

Silver: FREL = 0.0005(T-1673) + 0.05   (4-27)

Cadmium: FREL = 0.00033(T-1673) + 0.50.   (4-28)

From 2,573 to 3,073 K, the cumulative fractions of the inventory released are calculated according to:

Silver: FREL = 0.001(T-2573) + 0.5   (4-29)

Cadmium: FREL = 0.0004(T-2573) + 0.8   (4-30)

which results in complete release at 3073 K.

The cumulative fraction of the inventory released is then scaled by 0.1 for silver and 0.7 for cadmium to take into account the relocation of silver and cadmium.

4.2.2 Release During UO$_2$ Liquefaction and Fragmentation

The effect of UO$_2$ liquefaction is modeled by allowing xenon, krypton, cesium, and iodine to be instantaneously released to the gap from any fuel that is liquefied as predicted by the LIQSOL model. During the fragmentation of the UO$_2$, the fission products accumulated upon grain boundaries, as predicted by the theoretical model, are released instantaneously. Subsequent release within a rubble bed is controlled only by the intragrain processes. The release of other less volatile species is not affected by liquefaction or fragmentation.

4.2.3 Enthalpy of Released Gases

The noncondensable gases released from the gap are hydrogen, helium, krypton, and xenon. Iodine is also assumed to be noncondensable in this model, even though it is slightly soluble in water at high temperatures. The specific heat of the noble gases (helium, xenon, krypton) is nearly constant with temperature. Therefore, the enthalpy of a particular species can be calculated as a function of specific heat and temperature.

The specific heat of hydrogen is a function of temperature, so the enthalpy must be determined by

$$h = h'_o + \int_{T_o}^{T} c_p(T) \, dT \tag{4-31}$$

where

h	=	enthalpy of gas (J/kg)
c_p	=	specific heat of gas (J/kg $\bullet$ K)
T	=	temperature of gas (K)
h'_o	=	enthalpy at reference temperature T_o (J/kg)
T_o	=	reference temperature (K).

The specific heat of hydrogen is expressed as a function of temperature[30] as

$$c_p = (a + bT + cT^2 + dT^3 + eT^4) \, R \tag{4-32}$$

Inserting Equation (4-32) into Equation (4-31) and integrating yields

$$h = h'_o + Ra\,(T - T_0) + \frac{b}{2}\,(T^2 - T_0^2) + \frac{c}{3}\,(T^3 - T_0^3) + \frac{d}{4}\,(T^4 - T_0^4) + \frac{e}{5}\,(T^5 - T_0^5)$$

$$= h'_o + R\,(aT + \frac{b}{2}T^2 + \frac{c}{3}T^3 + \frac{d}{4}T^4 + \frac{e}{5}T^5) \tag{4-33}$$

Reference 31 supplies the constants a through e in Equation (4-32) for the temperature range of 300 to 5,000 K, with a reference temperature of 300 K. However, the SCDAP/RELAP5 hydrodynamic model requires that the enthalpy be based on a reference temperature of 0 K. In order to account for this shift in reference temperature, the constant h'_o was adjusted so that the enthalpy calculated with Equation (4-33) coincided with hydrogen enthalpy tables based on a reference temperature of 0 K. The constants in Equation (4-33) (a-e, R,h) are given in Table 4-3. (The thermodynamic properties of all the gap gases are also given in Table 4-3). Figure 4-1 shows a comparison between enthalpy calculated with Equation (4-33) and low pressure data from Keenan[32] and 20 MPa data from Reynolds.[33] Note that Equation (4-33) and the data form Keenan are nearly identical.

The enthalpy of iodine is assumed to be

$$h(I_2) = c_P T + h_v + h_m \tag{4-34}$$

where

h_v = heat of vaporization (J/kg)

h_m = heat of fusion (J/kg).

To determine the enthalpy of a mixture of noncondensable gases, the enthalpies of the individual species are combined in the following manner: The enthalpy of cesium hydroxide is assumed to be the heat of formation in water, since the reaction occurs when the cesium is released and is a large energy source compared with the energy carried into the reaction by the cesium compound or water. All of the energy from this reaction is assumed to be imparted to cesium hydroxide rather than hydrogen gas.

The enthalpy of cesium iodide is assumed to be

$$h(CsI) = c_P T + h_v + h_s + h_m \tag{4-35}$$

where

h_v = heat of vaporization (J/kg)

h_s = heat of solution (J/kg)

h_m = heat of fusion (J/kg).

The heat of formation is not included because the reaction is thought to occur within the fuel matrix.

Table 4-3. Thermodynamic properties of gap gases.

Hydrogen[a] $c_p = (a + bT + cT^2 + dT^3 + eT^4) R$ **(J/kg • K)**

h_o	a	b	c	d	e	Temperature Range (K)
0.122×10^6	3.05745	2.67652×10^{-3}	-5.80992×10^{-6}	5.52104×10^{-9}	-1.81227×10^{-12}	$300 < T \leq 1,000$
0.576×10^5	3.10019	5.11195×10^{-4}	5.26442×10^{-8}	-3.491×10^{-11}	3.69452×10^{-15}	$T > 1,000$

Species	Heat of formation (J/kg)	Heat of solution (J/kg)	Heat of fusion (J/kg)	Heat of vaporization (J/kg)	c_p (J/kg • K)
CsI[b]		-1.33×10^5	9.18×10^4	5.82×10^5	240.0
$CsOH$[c]	3.18×10^6	--	--	--	540.0
He[d]	--	--	--	--	5,233.5
Kr[e]	--	--	--	--	248.5
Xe[f]	--	--	--	--	158.5
I_2[g]	--	--	--	--	147.5

a. Reference 31
b. Reference 34
c. Reference 34
d. Reference 35
e. Reference 35
f. Reference 35
g. Reference 35
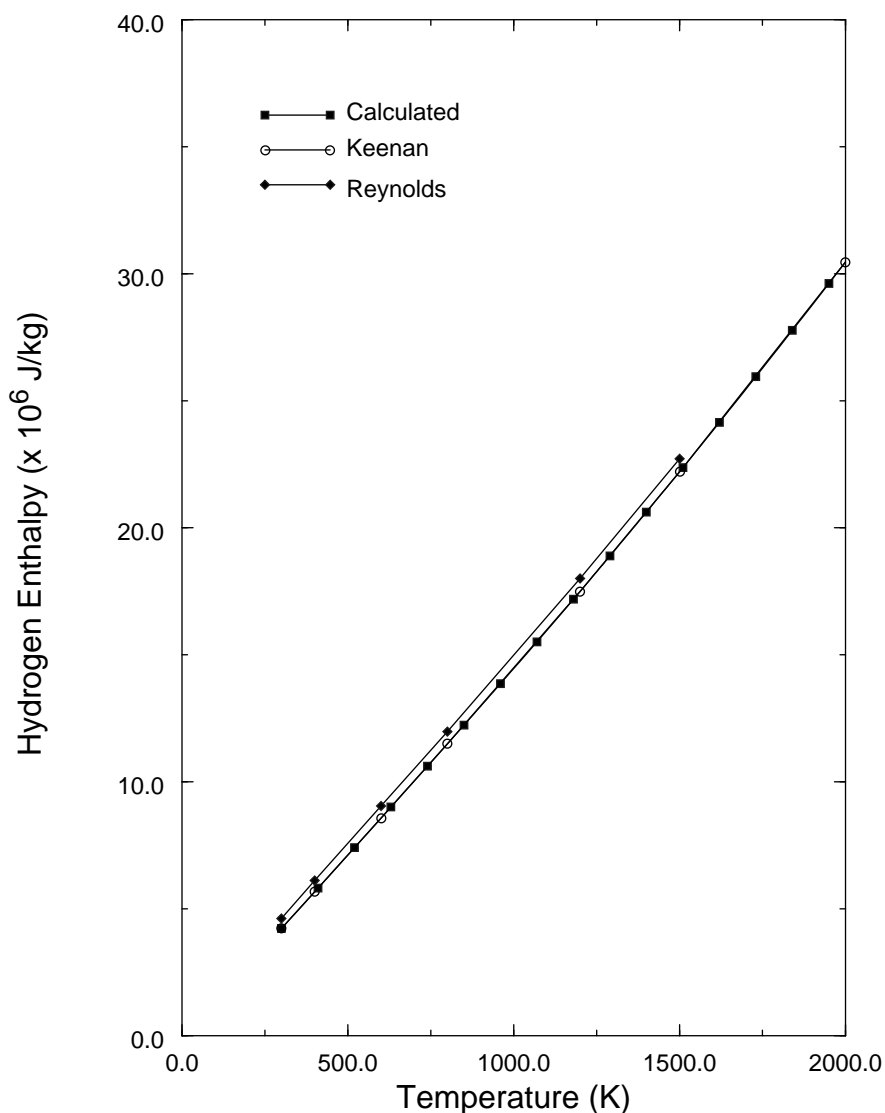
Figure 4-1. Comparison of calculated hydrogen enthalpy using Equation (4-33) and data from Keenan[32] and Reynolds.[33]

4.3   Decay Heat Reduction due to Fission Product Release

The reduction in fission product decay heat resulting from loss of volatile elements can be accounted for using the model described in Reference 28. Fission product decay heat for the intact fuel is calculated from the power history using ANS-5.1. After a major disruptive event, the decay heat reduction is determined from a set of pre-calculated tabular values describing the time dependent fractional changes in decay heat following fuel disruption. The existing SCDAP tables correspond to several possible irradiation history volatile element release scenarios. This method provides a mechanism for treating decay heat reduction in the disrupted fuel region but provides no information on the distribution of decay power among the released materials.

4.3.1   Fission Product Decay Heat Methodology

This section summarizes the methodology and results of calculations performed to obtain decay heat distributions for the released fission products. Based on model reviews, it was agreed to limit the analysis to one of the irradiation history volatile release scenarios in Reference 28 and to isolate contributions from tellurium, iodine, and cesium. Decay heat contributions from the remaining fission products are lumped into a single composite group.

The generic pressurized water reactor (PWR) rapid fuel heatup scenario described in Reference 28 was selected for this analysis. Fission product inventories were calculated using ORIGEN2,[36] assuming full power operation at the end of an equilibrium cycle. Fuel failure was assumed to occur at 2 minutes after shutdown. Fission product releases were calculated using ORIGEN2 and the time dependent release rate constants listed in Table 4 of Reference 28. These best estimate release rate constants are not necessarily the current best estimate values but were used for this analysis to maintain compatibility with the existing SCDAP volatile element release scenarios.

4.3.2   Fission Product Decay Heat Model Results

The time dependent decay heat contributions from selected elements are shown in Table 4-4 and in Figure 4-2. The decay heat fraction is defined as the ratio of the decay heat from all isotopes of that element to the decay heat of all released fission products. The decay heat contribution from all released fission products other than tellurium, iodine, and cesium is about 76% at 130 seconds and drops to about 23% at 15.6 hours. Table 4-5 lists estimated decay heat gamma fractions for the three elements as a function of time following shutdown.

Table 4-4. Fractional decay heat contributions for selected fission product elements (based on total decay heat from all released fission products).

Time after shutdown (s)	Tellurium	Iodine	Cesium
130	0.0485	0.1179	0.0739
150	0.0504	0.1214	0.0756
170	0.0522	0.1248	0.0774
180	0.0531	0.1265	0.0783
200	0.0530	0.1437	0.0891
220	0.0530	0.1594	0.0986
240	0.0529	0.1737	0.1070
260	0.0515	0.2149	0.1286
280	0.0506	0.2440	0.1431
300	0.0502	0.2659	0.1536
320	0.0505	0.3094	0.1732
340	0.0511	0.3313	0.1822
360	0.0518	0.3452	0.1874
480	0.0524	0.3727	0.1948
540	0.0526	0.3839	0.1971
600	0.0528	0.3939	0.1986
660	0.0530	0.4030	0.1995
720	0.0532	0.4113	0.2000
750	0.0518	0.4421	0.1773
780	0.0534	0.4538	0.1710
840	0.0505	0.4729	0.1584
1,020	0.0519	0.4970	0.1516
1,080	0.0534	0.5000	0.1521
1.7783×10^3	0.0498	0.5321	0.1429
3.1623×10^3	0.0436	0.5726	0.1177
5.6234×10^3	0.0359	0.6162	0.0738
1.0000×10^4	0.0288	0.6521	0.0322
1.7783×10^4	0.0267	0.6755	0.0197
3.1623×10^4	0.0311	0.6965	0.0248
5.6234×10^4	0.0381	0.6988	0.0340
1.0000×10^5	0.0448	0.6731	0.0468
1.7783×10^5	0.0484	0.6287	0.0640
3.1623×10^5	0.0448	0.5564	0.0858
5.6234×10^5	0.00354	0.4702	0.1177
1.000×10^6	0.0251	0.3707	0.1772
1.7783×10^6	0.0197	0.2403	0.2944
3.1623×10^6	0.0214	0.0960	0.4814
5.6234×10^6	0.0190	0.0118	0.6532
1.0000×10^7	0.0099	0.0002	0.7123
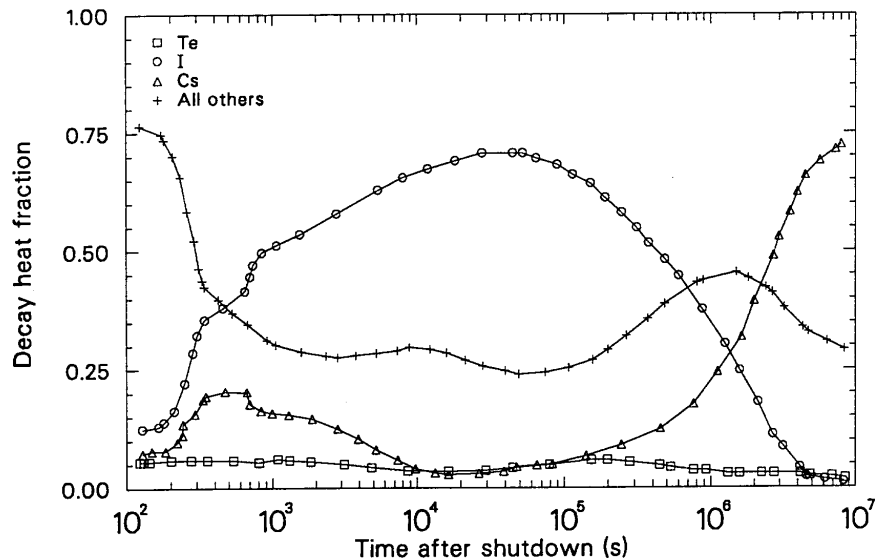
Figure 4-2. Decay heat contributions of selected elements (based on total decay heat of all released fission products).

Table 4-5. Estimated gamma decay power fractions for released fission products (based on total decay heat from all released fission products).

Time after shutdown(s)	Tellurium	Iodine	Cesium
170	0.6594	0.7832	0.5082
320	0.6616	0.7924	0.5715
540	0.6638	0.7948	0.6025
1080	0.6657	0.7945	0.6379
1.7783×10^3	0.6718	0.7929	0.6723
3.1623×10^3	0.6791	0.7895	0.6983
5.6234×10^3	0.6830	0.7833	0.7169
1.0000×10^4	0.6763	0.7729	0.7642
1.7783×10^4	0.6653	0.7591	0.8506
3.1623×10^4	0.6721	0.7452	0.8663
5.6234×10^4	0.6821	0.7335	0.8673
1.0000×10^5	0.6809	0.7291	0.8670
1.7783×10^5	0.6662	0.7367	0.8659
3.1623×10^5	0.6363	0.7499	0.8639
5.6234×10^5	0.5796	0.7486	0.8606
1.0000×10^6	0.4579	0.7269	0.8554
1.7783×10^6	0.2437	0.6970	0.8477
3.1623×10^6	0.1400	0.6787	0.8386
5.6234×10^6	0.1302	0.6759	0.8314
1.0000×10^7	0.1219	0.6757	0.8267

4.4   Fuel State Models

The fuel rod state modeling includes models for locating the radial position of fuel rod materials and changes in axial power peaking due to fuel axial relocation. Because material with a different peaking factor may be moved to a new axial node location, axial peaking factors are calculated as a function of elevation. Figure 4-3 presents the geometry considered, which accounts for the relocation of material due to liquefaction, flow, and solidification.

The peaking factor in relocated material is found using the following equation:

$$_cF_{i+1}(z) = \begin{cases} 0 & \text{for } z > z_2 \\ \dfrac{A_a(z)}{A_t(z)} \displaystyle\int_{z_3}^{z_4} \dfrac{F_i(z)\,A_r(z)}{V_a(z)}\,dz + \dfrac{_cF_i(z)\,A_c(z)}{A_t(z)} & \text{for } z_1 < z < z_2 \end{cases} \tag{4-36}$$
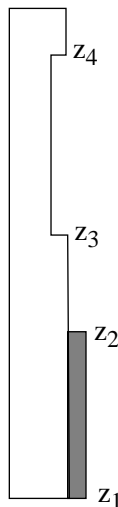
Figure 4-3. Melting and solidification geometry.

where

$_cF_{i+1}(z)$ =   axial peaking factor for delayed heating of the crust at time $i + 1$

$_cF_i(z)$ =   axial peaking factor for delayed heating of the crust at time i

$F_i(z)$ =   average axial peaking factor for z_3 to z_4

$A_r(z)$ =   local area of removed material (m^2)

$A_t(z)$ =   total area of crust in the region at the end of time step (m^2)

$A_c(z)$ =   crust area at the beginning of the time step (m^2)

$A_a(z)$ =   area added to the crust at elevation z during the time step (m^2)

z =   axial elevations (m)

V_a =   total volume of crust added during the time step (m^3).

4.5   Fuel Rod Cladding Deformation Model

The ballooning of fuel rod cladding and the time and location of rupture of the cladding can have a significant impact on the progression of damage in a reactor core during a severe accident. Several phenomena that may occur during a severe accident are influenced by cladding ballooning and rupture. The most important of these phenomena are cladding oxidation and heatup. If cladding is calculated to balloon and rupture, the heatup due to oxidation may be a factor of 2.6 times larger than that before ballooning and rupture. The factor of 2.6 is the result of the cladding diameter increasing up to a factor of 1.3 due to ballooning and the inside surface area of the cladding being exposed to steam after rupture of the cladding, which doubles the surface area of the cladding that is oxidizing. Other phenomena influenced by cladding ballooning include fission product release from fuels to the coolant and the distribution of flow throughout the reactor core.

The SCDAP/RELAP5 code uses mechanistic models to calculate the elastic-plastic deformation that can occur in fuel rods during a severe accident. Anisotropic plastic deformation is calculated using the theory of Hill[38] and the Prandtl-Reuss equations.[39] If the cladding deformation is small (maximum true hoop strain less than 15%), then a simplified model that does not take into account circumferential variations in cladding temperature is used. This model is called the sausage deformation model. If the cladding deformation is larger (maximum true hoop strain greater than 15%), then a more detailed model that takes into account the circumferential variation in temperature is used at the elevation of maximum cladding deformation. This model is called the localized deformation model. Section 4.5.1 describes the sausage deformation model, and Section 4.5.2 describes the localized deformation model.

4.5.1   Sausage Deformation Model

The sausage deformation model is based on the following assumptions:

- Cladding deformation is axisymmetric.

- Cladding deforms like a membrane. There are no bending strains in the cladding.

- Isotropic hardening is assumed in calculating the cladding yield stress.

- Once the outer diameter of the cladding is equal to the fuel rod pitch, no additional cladding deformation takes place.

- Cladding oxidation does not affect the cladding mechanical properties.

- Any constraint imposed by the spacer grids on cladding deformation is ignored.

- Once the inner diameter of the cladding is equal to the fuel pellet diameter, no additional cladding deformation takes place.

The sausage deformation model described here is similar to the model available in FRACAS-I,[40] except for the following two modifications:

1. Plasticity calculations are based on true strains. FRACAS-I uses engineering strains.

2. Anisotropic properties of cladding are taken into account in the calculation of effective stress and incremental plastic strains. FRACAS-I assumes that plastic deformation of cladding is isotropic.

In this model, the cladding strains are calculated at each component node of a fuel rod group. As cladding experiences elastic-plastic strains, an iterative scheme is required to ensure the convergence of cladding strains. It may be necessary to use a small component time step (the time step used to analyze intact fuel rods) to ensure convergence. Theory used to calculate these strains is described next.

Sausage cladding deformation is a stress driven process. First, the stresses in the cladding are calculated by satisfying the equilibrium conditions at each component node at the beginning of an iteration. The resulting expressions for the stresses are as follows:

$$\sigma_h = \frac{p_g r_i - p_c r_o}{r_o - r_i} \qquad (4\text{-}37)$$

$$\sigma_a = \frac{p_g r_i^2 - p_c r_o^2}{r_o^2 - r_i^2} \qquad (4\text{-}38)$$

$$\sigma_r = -0.5(p_c + p_g) \qquad (4\text{-}39)$$

where

σ_h	=	hoop stress (Pa)
σ_a	=	axial stress (Pa)
σ_r	=	radial stress (Pa)
p_g	=	gas pressure (Pa)
p_c	=	coolant pressure (Pa)
r_i	=	inside radius (m)
r_o	=	outside radius (m).

Note that the inner and outer radii are current radii in Equation (4-37) through (4-39), so the calculated stresses are true stresses. The effective stress,[41] σ_e, is given by

Fuel Rod

$$\sigma_e = [ACS(\sigma_h - \sigma_a)^2 + AAS(\sigma_a - \sigma_r)^2 + ARS(\sigma_r - \sigma_h)^2]^{0.5} \tag{4-40}$$

where ACS, AAS, and ARS are strength coefficients of anisotropy for calculating effective stress.

These coefficients are calculated with the aid of the MATPRO subroutine CANISO. At the beginning of a time step, the plastic increments during the time step are not known; so during the first iteration, they are assumed to be equal to zero in the calculations of the strength coefficients used in Equation (4-40).

If the effective stress, σ_e, is greater than the corresponding true effective yield stress (calculated using the MATPRO subroutine CSTRES), then the increments in the plastic strains are calculated using the Prandtl-Reuss equations and Hill's theory for anisotropic plastic deformation.

The effective true strain in the cladding is calculated using the MATPRO subroutine CSTRNI that takes into account the effect of strain rate and cladding temperature. Since plastic deformation is an irreversible process, d_{ep}, the increment in the true effective strain, is zero or positive. The increment in the plastic strain components is calculated as follows:

$$d\varepsilon_{h,p} = d_{ep}[A_1(\sigma_h - \sigma_a) + A_2(\sigma_h - \sigma_r)]/\sigma_e \tag{4-41}$$

$$d\varepsilon_{a,p} = d_{ep}[A_3(\sigma_a - \sigma_r) + A_1(\sigma_a - \sigma_h)]/\sigma_e \tag{4-42}$$

and

$$d\varepsilon_{r,p} = d_{ep}[A_2(\sigma_r - \sigma_h) + A_3(\sigma_r - \sigma_a)]/\sigma_e \tag{4-43}$$

where

$d\varepsilon_{h,p}$ = increment in plastic hoop strain

$d\varepsilon_{a,p}$ = increment in plastic axial strain

$d\varepsilon_{r,p}$ = increment in plastic radial strain

and A_1, A_2, and A_3 are coefficients of anisotropy for calculating plastic strain increments.

The total true hoop strain is

$$\varepsilon_h = \varepsilon_{h,e} + \varepsilon_{h,t} + \varepsilon_{h,p_o} + d\varepsilon_{h,p} \tag{4-44}$$

where

ε_h = total hoop strain at the end of the time step

$\varepsilon_{h,e}$ = hoop strain due to elastic deformation $[\sigma_h - \nu(\sigma_a + \sigma_r)]/E$

$\varepsilon_{h,t}$ = hoop strain due to thermal deformation $(\alpha\Delta T)_h$

ε_{h, p_o} = hoop strain due to plastic deformation at the beginning of the time step

ν = Poisson's ratio

E = elastic modulus (Pa).

Equation (4-44) may be written as

$$\varepsilon_h = [\sigma_h - \nu(\sigma_a + \sigma_r)]/E + (\alpha\Delta T)_h + \varepsilon_{h, p_o} + d\varepsilon_{h, p}. \tag{4-45}$$

Similarly,

$$\varepsilon_a = [\sigma_a - \nu(\sigma_r + \sigma_h)]/E + (\alpha\Delta T)_a + \varepsilon_{a, p_o} + d\varepsilon_{a, p} \tag{4-46}$$

and

$$\varepsilon_r = [\sigma_r - \nu(\sigma_a + \sigma_h)]/E + (\alpha\Delta T)_r + \varepsilon_{r, p_o} + d\varepsilon_{r, p}. \tag{4-47}$$

The true hoop strain, ε_h, is used to calculate cladding radii at the end of the iteration as follows:

$$R_{m1} = R_m e^{\varepsilon}h \tag{4-48}$$

where

R_m = original cladding mean radius (m)

R_{m1} = cladding mean radius at the end of the iteration (m).

The cladding wall thickness is calculated assuming that the cladding cross-sectional area remains constant:

$$T_{wall} = \frac{A_c}{2\pi(R_{m1})} \tag{4-49}$$

where

T_{wall} = cladding wall thickness at the end of the iteration (m)

A_c = cladding cross-section area (m^2).

So, the cladding radii at the end of the iteration are

$$r_o = R_{m1} + \frac{T_{wall}}{2} \tag{4-50}$$

Fuel Rod

$$r_i = R_{ml} - \frac{T_{wall}}{2} \tag{4-51}$$

The cladding radii in Equations (4-50) and (4-51) are used to calculate the void volume at the end of the iteration.

During the next iteration, the void volumes are used to update the fuel rod gas pressure model (see Section 4.6). The cladding radii from the last iteration [Equations (4-50) and (4-51)] are used to calculate stresses using Equations (4-37) through (4-39). The plastic strain increments from the last iteration using Equations (4-40) through (4-43) are used to calculate anisotropic strength coefficients (calculated using the MATPRO routine CANISO), which are used to calculate the effective stress in Equation (4-40). Then Equations (4-41) through (4-51) are solved. The iteration process continues until the calculated hoop stresses converge for each component node. The converged hoop stresses at each component node are compared with the corresponding failure stresses calculated using the MATPRO routine CMLIMT to determine whether or not the cladding has ruptured. Then the analysis will proceed to the next component time step. Once a fuel rod cladding has ruptured, the cladding deformation calculations for the corresponding fuel rod bundle are no longer performed during the remaining portion of the analysis.

The flow area reduction for each representative fuel rod component is then computed by subtracting the change in the cross-sectional area of the fuel rod from the original flow area. No allowance is made for flow internal to the cladding that could result from cladding failure. The total change in flow area for each thermal-hydraulic volume is then computed from the sum of the changes in flow area for all of the fuel rods. Deformation of other core components, such as control rods or structures, is neglected.

4.5.2   Localized Deformation Model

In the beginning of the analysis, the sausage type deformation model is used. The sausage type deformation model is replaced by the localized deformation model, and the calculations for the localized deformation begin if the following conditions are satisfied:

- Maximum cladding true hoop stress is less than failure stress (i.e., the cladding has not failed)

- Maximum true hoop strain is >15%

- At a node having maximum true hoop strain, the axial gradient in cladding temperature is (a) 1 K/cm, if cladding temperature is <1,250 K or (b) 10 K/cm, if cladding temperature is >1,250 K.

The above conditions are tested at every time step. If satisfied, the localized deformation model is used for the remaining portion of the analysis at the elevation of maximum cladding deformation. If the above conditions are not satisfied, then the sausage type deformation model is used.

The localized deformation model consists of two models that were developed earlier for the FRAP-T6 computer code.[42] These models are:

- Zircaloy cladding shape at failure - BALON2 model[41]

- Probabilistic flow area reduction model - FAR1 model.[43]

The BALON2 model calculates the localized cladding deformation for a single fuel rod at a selected axial location. The FAR1 model uses the uncertainty in the axial location of the maximum cladding temperature and calculates the probabilistic distribution of the cladding deformation along the axial direction for a bundle of fuel rods. The mean value of the cladding deformation is used to calculate the mean value of the flow area reduction at each component node of the bundle of fuel rods. The cladding localized deformation model for SCDAP/RELAP5 is based on the following assumptions:

- Localized deformation is assumed to initiate at an axial location where the effective true strain in the cladding is at a maximum and exceeds the corresponding instability true strain. This axial location is referred to as the ballooning location.

- The peak cladding temperature takes place close to the ballooning location so that the uncertainty in the ballooning location is the same as the uncertainty in the location of the peak cladding temperature.

- The effective plastic strain in the cladding along the fuel rod is not uniform.

- The inputs to the BALON2 model are assumed to represent an average rod in a given fuel rod bundle.

- The localized deformation of an individual rod does not affect the deformation of any other rod.

- The BALON2 model specifies the small variation in the temperature along the axial and circumferential directions near the ballooning location. The circumferential variation is non-axisymmetric but has a diameter of symmetry. The axial variation is approximately symmetric with respect to the ballooning location. So, the resulting cladding deformation is non-axisymmetric but has two planes of symmetry.

- Isotropic hardening is assumed in calculating the cladding yield stress.

- The FAR1 model assumes that the maximum flow area reduction due to coplanar localized deformation is 90%.

- Each group of fuel rods consists of only fuel rods and no control rod.

- Constraint imposed by the spacer grid on cladding deformation is not taken into account.

4.5.3 High-Temperature Cladding Deformation

In the event that ballooning does not occur until the cladding temperature exceeds 1,220 K, the oxide layer on the outside of the cladding will have a significant amount of strength. In this case the cladding limit strain (based upon rod-to-rod contact) will be reset to a value of 2% to represent the reduced amount of ballooning that may occur under these conditions.

4.6   Fuel Rod Internal Gas Pressure Model

The fuel rod internal gas pressure is computed from the perfect gas law. This includes different volumes of gas at different temperatures as given by

$$P = \frac{N_m R}{\sum_i \frac{V_i}{T_i}} \qquad (4\text{-}52)$$

Fuel Rod

where

  P = internal gas pressure (Pa)

  N_m = moles of gas in fuel rod void volumes (g-mole)

  R = universal gas constant (N•m/g-mole•K)

  V_i = i-th volume (m³)

  T_i = temperature of gas in i-th volume (K).

The different volumes considered are:

-   Fuel rod upper plenum volume,

-   Fuel rod lower plenum volume, if modeled,

-   Fuel void volumes at each axial elevation that are the sum of crack, dish, gap (except contributions due to cladding ballooning), porosity, and roughness volumes,

-   Additional gap volumes due to cladding ballooning at each axial elevation.

Thus, the gas pressure model becomes

$$P = \frac{N_m R}{\dfrac{V_{up}}{T_{up}} + \dfrac{V_{lp}}{T_{lp}} + \sum_{i=1}^{M} \dfrac{V_{(void),i} + V_{(gap),i}}{T_{f,i}}} \tag{4-53}$$

where

  V_{up} = Fuel rod upper plenum volume (m³)

  T_{up} = gas temperature in fuel rod upper plenum (K), which is assumed to be coolant temperature at the top of the rod plus 6 K

  V_{lp} = Fuel rod lower plenum volume (m³)

  T_{lp} = gas temperature in fuel rod lower plenum (K), which is assumed to be coolant temperature at the bottom of the rod plus 6 K

  M = number of axial nodes

  $V_{void,i}$ = fuel void volume in i-th axial node (m³)

  $V_{gap,i}$ = additional gap volume due to cladding ballooning in i-th axial node (m³)

  $T_{f,i}$ = average fuel temperature in i-th axial node (K).

4.6.1 Correlations for Void Volumes for Standard PWR and BWR Fuel

Correlations were developed to account for the effects of fuel burnup and temperature on fuel void volumes for commercial PWR and BWR fuel rods. Twelve FRAPCON-2[44] cases were used, six for a standard PWR fuel rod and six for a standard BWR fuel rod. The detailed fuel rod data used are given in

Kleijnen,[45] while the basic data are listed in Tables 4-6 and 4-7. For a set of constant burnup states between 0.1 and about 30 MWd/kgU, the average rod temperature was specified stepwise from 500 to 1,100 K for the PWR rod, and from 500 to 1,200 K for the BWR rod, with essentially zero power. Because of a constant temperature profile both in the radial and axial directions, the local temperatures were equal to the average rod temperatures for the FRAPCON-2 calculations. The peak temperatures of 1,100 and 1,200 K for PWR and BWR, respectively, have been defined as upper bounds of the temperature ranges taken in consideration because the FRAPCON-2 calculations showed cladding ballooning and rupture for temperatures greater than these peak temperatures. The coolant pressure was held constant at 15.51×10^6 N/m^2 and 7.14×10^6 N/m^2 for the PWR and BWR fuel rod calculations, respectively.

Table 4-6. PWR fuel rod data input for FRAPCON-2 calculations.

Cladding inside diameter	9.50×10^{-3} m
Cladding thickness	0.61×10^{-3} m
Diametric gap thickness	0.191×10^{-3} m
Fuel pellet diameter	9.31×10^{-3} m
Fuel pellet length	15.20×10^{-3} m
Fuel pellet true density	94%
Fuel stack height	3.66 m
Fuel dish volume fraction	0.0147
Plenum length	0.173 m
Plenum volume	1.04×10^{-5} m^3
Rod total void volume	2.52×10^{-5} m

The relative plenum volumes

$$R_p = \frac{V_p^{hot}}{V_p^{cold}} \qquad (4\text{-}54)$$

and the relative fuel void volumes

$$R_{void} = \frac{V_{void}^{hot}}{V_{void}^{cold}} \qquad (4\text{-}55)$$

depend on fuel rod temperature and burnup and are shown in es 4-4 through 4-7, respectively, for the PWR and BWR fuel rod.

Table 4-7. BWR fuel rod data input for FRAPCON-2 calculations

Cladding inside diameter	12.70×10^{-3} m
Cladding thickness	0.864×10^{-3} m
Diametric gap thickness	0.305×10^{-3} m
Fuel pellet diameter	12.40×10^{-3} m
Fuel pellet length	9.27×10^{-3} m
Fuel pellet true density	94%
Fuel stack height	3.66 m
Fuel dish volume fraction	0.
Plenum length	0.406m
Plenum volume	4.52×10^{-5} m^3
Rod total void volume	6.85×10^{-5} m^3

The FRAPCON-2 calculations show a jump in the temperature-dependence of both the relative plenum volumes and the relative fuel void volumes from temperature range of 500 to 700 K to the temperature ranges of 800 to 1,100 K and 800 to 1,200 K for the PWR and BWR, respectively. This is an effect of the zircaloy material behavior, resulting in a strong increase of strain rate sensitivity and thus a significant increase of cladding hoop strain at temperatures above ~750 K. The resulting decrease in cladding diameter for coolant pressures higher than the internal gas pressure causes a decrease in both the plenum volume and the fuel void volume.

The behavior of relative void volumes, as shown in Figures 4-4 through 4-7, can be approximated by a function of the form

$$R = f(T) e^{\alpha Bu} (1 - \beta e^{\gamma Bu}) \tag{4-56}$$

where

R	=	relative void volume, related to the corresponding as-fabricated volume
f(T)	=	$a + bT$
T	=	fuel rod temperature (K)
α, β, γ	=	coefficients, the values of which depend on the kind of fuel rod (i.e., PWR or BWR rod) and on the temperature range (i.e., $500 \leq T \leq 750$ K or $750 < T \leq 1,100$ K or $750 < T \leq 1,200$ K)
Bu	=	burnup (MWD/kgU).
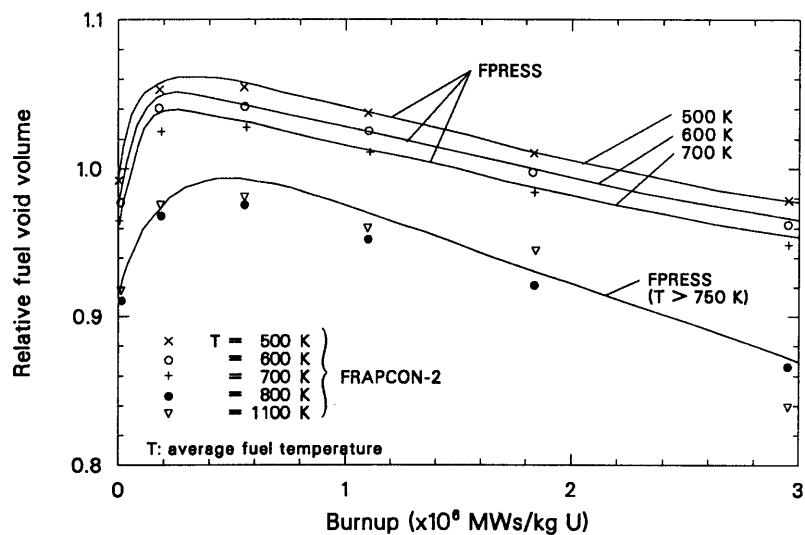
Figure 4-4. Relative plenum volume, R_p, resulting from FRAPCON-2 calculations for a standard PWR fuel rod design.
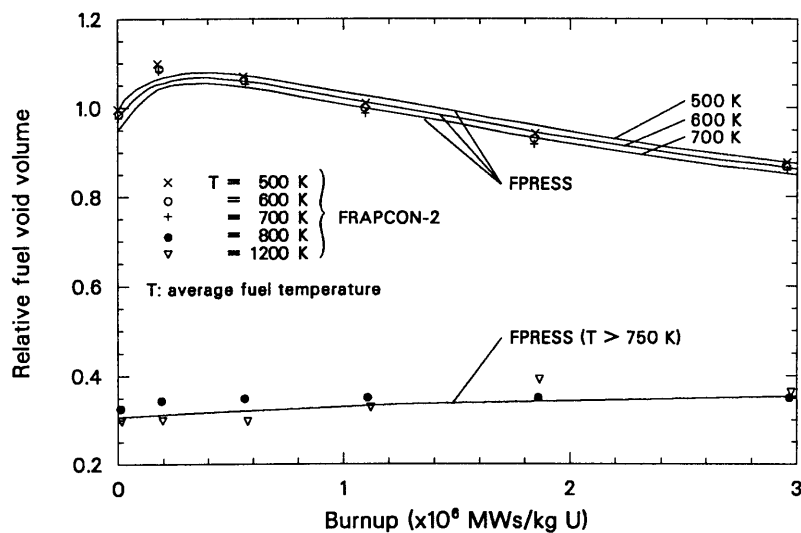
Figure 4-5. Relative fuel void volume, R_{void}, resulting from FRAPCON-2 calculations for a standard PWR fuel rod design.
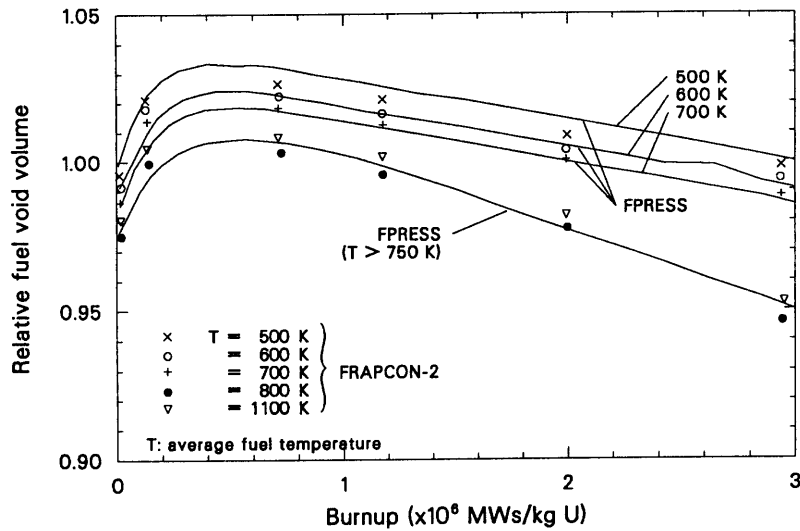
Figure 4-6. Relative plenum volume, R_p, resulting from FRAPCON-2 calculations for a standard BWR fuel rod design.
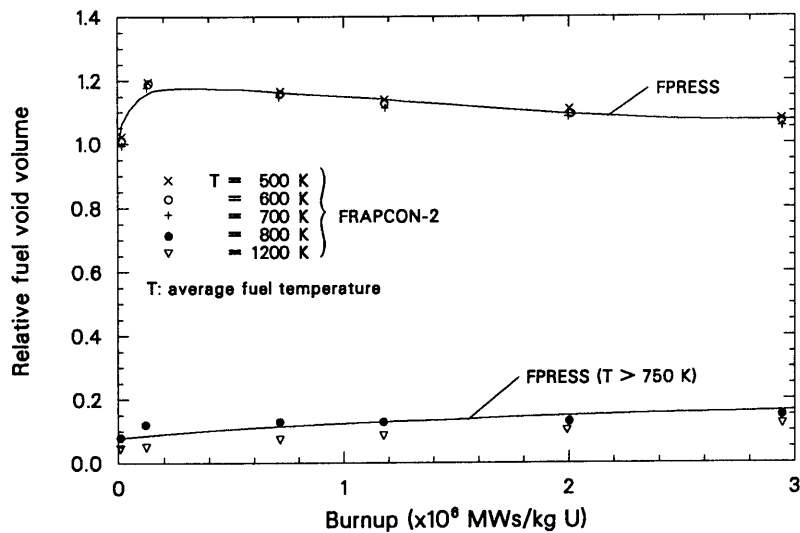
Figure 4-7. Relative fuel void volume, R_{void}, resulting from FRAPCON-2 calculations for a standard BWR fuel rod design.

The coefficients of Equation (4-55) are listed in Table 4-8 for the different reactor systems and temperature ranges. Tables 4-9 through 4-12 show comparisons between the FRAPCON-2 results and the results predicted using Equation (4-57). The differences in calculated relative plenum volumes and relative

fuel void volumes for both the standard PWR and the standard BWR fuel rod, expressed by the relative error ε, are small.

The FRAPCON-2 results of relative plenum volumes, as shown in Figures 4-4 and 4-6, are interpreted as two overlapping effects that influence the hot plenum volume of both the standard PWR and the standard BWR fuel rod. These are the fuel stack axial deformation and (under the special conditions of coolant pressures exceeding internal gas pressures) the significant decrease in plenum cladding diameter at temperatures > 750 K. When the latter effect becomes dominant for plenum (cladding) temperatures exceeding 750 K, the plenum volume calculation by the FPRESS model is performed in two different ways, depending on the temperature.

For plenum (cladding) temperatures T_p in the range of $500 \leq T_p < 750$ K, the plenum volume is calculated by linear super-position of the temperature-dependent contributions of the axial fuel zones due to fuel axial expansion:

Table 4-8. Coefficients $(a, b, \alpha, \beta, \gamma)$ of the general empirical correlation for calculation of relative void volumes.

$R = (a + bT)\, e^{\alpha Bu}\, [1 - \beta e^{\gamma Bu}]$				
$\underline{a}$	$\underline{b}$	α	β	γ
Standard PWR fuel rod				
Plenum volume				
$500 \leq T \leq 750$ K 1.146	-1.37×10^{-4}	-2.90×10^{-3}	0.0952	-1.148
$750 \leq T \leq 1,100$ K 1.040	0.0	-5.19×10^{-3}	0.1126	-0.3712
Fuel void volume				
$500 \leq T \leq 750$ K 1.175	-1.11×10^{-4}	-7.498×10^{-3}	0.1247	-0.6442
$750 \leq T \leq 1,100$ K 0.360	0.0	0.0	0.1441	-4.473×10^{-2}
Standard BWR fuel rod				
Plenum volume				
$500 \leq T \leq 750$ K 1.063	-0.52×10^{-4}	-1.122×10^{-3}	0.0425	-0.5838
$750 \leq T \leq 1,200$ K 1.031	0.0	-2.344×10^{-3}	0.0534	-0.3070
Fuel void volume				
$500 \leq T \leq 750$ K 1.198	0.0	-3.588×10^{-3}	0.167	-1.288
$750 \leq T \leq 1,200$ K 0.160	0.0	0.0	0.5343	-7.226×10^{-2}

Table 4-9. Relative plenum volume, R_p, of a standard PWR fuel rod, comparison between FRAPCON-2 and FPRESS calculations.

	Burnup (MWs/kgU)	Temperature (K)
		500	600	700	800	900	1,000	1,100
FRAPCON-2	1.123×10^4	0.992	0.987	0.965	0.911	0.913	0.915	0.917
	1.901×10^5	1.054	1.041	1.026	0.970	0.972	0.975	0.975
	5.615×10^5	1.055	1.042	10.29	0.975	0.977	0.978	0.980
	1.106×10^6	1.038	1.025	1.011	0.953	0.955	0.958	0.959
	1.840×10^6	1.011	0.997	0.984	0.920	0.921	0.950	0.944
	2.938×10^6	0.978	0.961	0.947	0.865	0.840	0.837	0.837
FPRESS	1.123×10^4	0.989	0.976	0.964	0.926	0.926	0.926	0.926
	1.901×10^5	1.063	1.049	1.036	0.975	0.975	0.975	0.975
	5.616×10^5	1.058	1.044	1.031	0.993	0.933	0.993	0.993
	1.106×10^6	1.038	1.025	1.012	0.970	0.970	0.970	0.970
	1.840×10^6	0.013	1.000	0.988	0.930	0.930	0.930	0.930
	2.938×10^6	0.977	0.964	0.952	0.870	0.870	0.870	0.870
Relative error ε	1.134×10^4	<0.01	<0.01	<0.01	0.02	0.01	<0.01	<0.02
	1.901×10^5	<0.01	<0.01	<0.01	<0.01	<0.01	--	--
	5.616×10^5	<0.01	<0.01	<0.01	0.02	0.02	0.02	0.01
	1.106×10^5	--	--	<0.01	0.02	0.01	0.01	0.01
	1.840×10^6	<0.01	<0.01	<0.01	0.01	<0.01	0.02	0.01
	2.938×10^6	<0.01	<0.01	<0.01	<0.01	0.03	0.03	0.03

Table 4-10. Relative fuel void volume, R_{void}, of a standard PWR fuel rod, comparison between FRAPCON-2 and FPRESS calculations.

		Temperature (K)						
	Burnup (MWs/kgU)	500	600	700	800	900	1,000	1,100
FRAPCON-2	1.123×10^4	0.998	0.987	0.980	0.323	0.323	0.307	0.295
	1.901×10^5	1.099	1.090	1.083	0.341	0.343	0.302	0.291
	5.615×10^5	1.071	1.064	1.054	0.345	0.346	0.301	0.289
	1.106×10^6	1.007	0.997	0.989	0.345	0.345	0.336	0.324
	1.840×10^6	0.941	0.993	0.923	0.346	0.364	0.341	0.385
	2.938×10^6	0.876	0.870	0.859	0.349	0.353	0.352	0.352
FPRESS	1.123×10^4	0.990	0.180	0.971	0.308	0.308	0.308	0.308
	1.901×10^5	1.068	1.057	1.047	0.313	0.313	0.313	0.313
	5.616×10^5	1.064	1.054	1.043	0.321	0.321	0.321	0.321
	1.106×10^6	1.017	1.007	0.997	0.331	0.331	0.331	0.331
	1.840×10^6	0.954	0.954	0.935	0.335	0.335	0.335	0.335
	2.938×10^6	0.868	0.859	0.850	0.350	0.350	0.350	0.350
Relative error ε	1.123×10^4	<0.01	<0.01	<0.01	0.05	0.05	<0.01	<0.04
	1.901×10^5	<0.03	<0.03	<0.03	<0.08	<0.09	0.04	0.08
	5.616×10^5	<0.01	<0.01	<0.01	0.07	0.07	0.07	0.11
	1.106×10^6	<0.01	0.01	<0.01	0.04	0.01	0.04	0.02
	1.840×10^6	0.01	0.01	0.01	0.03	<0.03	0.02	--
	2.938×10^6	<0.01	0.01	0.01	<0.01	<0.01	<0.01	<0.01

Table 4-11. Relative plenum volume, R_p, of a standard BWR fuel rod, comparison between FRAPCON-2 and FPRESS calculations.

	Burnup (MWs/ kgU)	Temperature (K)							
		500	600	700	800	900	1,000	1,100	1,200
FRAPCON-2	0.691×10^4	0.995	0.991	0.986	0.975	0.977	0.978	0.979	0.98
	1.244×10^5	1.021	1.018	1.013	0.999	1.000	1.001	1.003	1.00
	7.085×10^5	1.027	1.022	1.018	1.003	1.004	1.005	1.006	1.00
	1.175×10^6	1.021	1.016	1.012	0.995	0.996	0.997	0.999	1.00
	1.996×10^6	1.008	1.003	1.000	0.997	0.978	0.980	0.980	0.98
	2.929×10^6	0.998	0.993	0.988	0.946	0.948	0.950	0.950	0.95
FPRESS	0.691×10^4	0.995	0.990	0.985	0.977	0.977	0.977	0.977	0.97
	1.244×10^5	1.016	1.011	1.006	0.993	0.993	0.993	0.993	0.99
	7.085×10^5	1.027	1.022	1.017	1.007	1.007	1.007	1.007	1.00
1.00	1.175×10^6	1.021	1.016	1.012	0.998	0.998	0.998	0.998	0.99
	1.996×10^6	1.010	1.005	1.000	0.977	0.977	0.977	0.977	0.97
	2.929×10^6	0.998	0.993	0.988	0.953	0.953	0.953	0.953	0.95
Relative error ε	0.691×10^4	--	<0.01	<0.01	<0.01	--	<0.01	<0.01	<0.0
	1.244×10^5	<0.01	<0.01	<0.01	<0.01	<0.01	<0.01	<0.01	<0.0
	7.085×10^5	--	--	<0.01	<0.01	<0.01	<0.01	<0.01	<0.0
	1.175×10^6	--	--	--	<0.01	<0.01	<0.01	<0.01	<0.0
	1.996×10^6	<0.01	<0.01	--	--	<0.01	<0.01	<0.01	<0.0
	2.929×10^6	--	--	--	<0.01	<0.01	<0.01	<0.01	<0.0

Table 4-12. Relative fuel void volume, R_{void}, of a standard BWR fuel rod, comparison between FRAPCON-2 and FPRESS calculations.

	Burnup (MWs/ kgU)	Temperature (K)							
		500	600	700	800	900	1,000	1,100	1,200
FRAPCON-2	0.691×10^4	1.017	1.007	0.994	0.075	0.075	0.057	0.041	0.04
	1.244×10^5	1.201	1.190	1.183	0.117	0.117	0.054	0.040	0.03
	7.085×10^5	1.170	1.159	1.148	0.124	0.124	0.085	0.071	0.06
	1.175×10^6	1.143	1.133	1.122	0.128	0.128	0.102	0.087	0.08
	1.996×10^6	1.102	1.095	1.084	0.136	0.136	0.121	0.107	0.09
	2.929×10^6	1.077	1.067	1.060	0.147	0.145	0.145	0.132	0.12
FPRESS	0.691×10^4	1.017	1.017	1.017	0.075	0.075	0.075	0.075	0.07
	1.244×10^5	1.160	1.160	1.160	0.083	0.083	0.083	0.083	0.08
	7.085×10^5	1.162	1.162	1.62	0.113	0.113	0.113	0.113	0.11
	1.175×10^6	1.140	1.140	1.140	0.128	0.128	0.128	0.128	0.12
	1.996×10^6	1.102	1.102	1.102	0.144	0.144	0.144	0.144	0.14
	2.929×10^6	1.060	1.060	1.060	0.153	0.153	0.153	0.153	0.15
Relative error ε	0.691×10^4	--	<0.01	<0.02	--	--	0.32	0.83	0.8
	1.244×10^5	0.03	0.03	0.02	0.29	0.29	0.54	1.000	1.00
	7.085×10^5	<0.01	<0.01	0.01	0.09	0.09	0.33	0.59	0.6
	1.175×10^6	<0.01	<0.01	0.02	--	--	0.25	0.47	0.5
	1.996×10^6	--	<0.01	0.02	0.06	0.06	0.19	0.35	0.4
	2.929×10^6	0.02	<0.01	--	0.04	0.04	0.04	0.16	0.2

Fuel Rod

$$V_p = \left[\sum_{i=1}^{M} \frac{l_i}{l_{tot}^{cold}} R_p (T_{f,i}) \right] V_p^{cold} \tag{4-57}$$

where

V_p^{cold} = plenum volume (m^3)

V_p = as-fabricated plenum volume (m^3)

l_i = length of axial fuel zone i (m)

l_{tot}^{cold} = total fuel stack length (m) $\sum_{i=1}^{M} l_i$

$R_p(T_i)$ = relative plenum volume, evaluated using Equation (4-55) with T = T$_i$

$T_{f,i}$ = average fuel temperature in axial zone i (K).

For plenum (cladding) temperatures $T_p > 750$ K, the plenum volume is approximated by

$$V_p = R_p (T_p) V_p^{cold} \tag{4-58}$$

where

$R_p(T_p)$ = relative plenum volume, evaluated using Equation (4-55) with T = T$_p$

T_p = plenum (cladding) temperature, $750 < T_p < 1,100$ K for standard PWR case and $750 < T_p < 1,200$ K for standard BWR case.

$R_p(T_p)$ includes the effect of the fuel stack axial expansion with the assumption of a uniform axial fuel temperature T_F.

The fuel void volume in axial zone i is calculated by

$$V_{void,i} = R_{void} (T_{f,i}) V_{void,i}^{cold} \tag{4-59}$$

where

$V_{void,i}$ = fuel void volume in axial zone i (m^3)

$R_{void}(T_{f,i})$ = relative fuel void volume in axial zone i, evaluated by Equation (4-55) with T = T$_{f,i}$ and the coefficients given in Table 4-8

$T_{f,i}$ = average fuel temperature in axial zone I (K)

$V_{void,i}^{cold}$ = as-fabricated void volume in axial zone i (m^3).

For the case of internal gas pressure exceeding coolant pressure, no FRAPCON-2 calculations have been performed. Thus, the FPRESS model uses the information on relative void volumes provided by the FRAPCON-2 calculations for the temperature range of $500 \leq T \leq 750$ K. For maximum average fuel temperatures up to 1,100 and 1,200 K, for a PWR and BWR, respectively, the relative plenum and fuel void volumes are extrapolated from this lower temperature range in a linear manner using Equation (4-55).

As mentioned before, fuel temperatures have been limited to 1,100 K for the standard PWR fuel rod and to 1,200 K for the standard BWR fuel rod, since FRAPCON-2 predicted significant permanent cladding deformation and cladding rupture at higher temperatures. Thus, with respect to the calculation of relative plenum and fuel void volumes on the basis of the empirical correlations, the FPRESS model will set all average fuel temperatures exceeding 1,100 and 1,200 K to these limiting values.

The corrections discussed in the next sections are used to model conditions beyond those of the FRAPCON-2 simulations.

4.6.2 Corrections in Void Volumes Due to Variation from Standard Design

To include fuel rods with as-fabricated plenum and/or fuel stack length that differ significantly from the standard rods, a correction factor is introduced. This correction factor fits the calculated relative plenum volumes of the standard cases on different rod lengths.

The relative change in plenum volume due to temperatures can be approximated by

$$
\frac{V_p^{hot} - V_p^{cold}}{V_p} = \frac{[\Delta L + (L + \Delta L)\, \alpha_{clad}\Delta T - (L\alpha_{fuel}\Delta T)\,]\, A^{hot} - \Delta L A^{cold}}{\Delta L A^{cold}} \tag{4-60}
$$

where

V_p^{hot} $=$ hot plenum volume (m^3)

V_p^{cold} $=$ as-fabricated plenum volume (m^3)

L $=$ as-fabricated fuel stack length (m)

ΔL $=$ as-fabricated plenum length (m)

ΔT $=$ temperature difference between hot and cold fuel rod state assuming a uniform rod temperature

α_{clad} $=$ expansion coefficient of cladding (l/K)

α_{fuel} $=$ expansion coefficient of fuel (l/K)

A^{hot} $=$ cross-sectional area of hot plenum (m^2)

A^{cold} $=$ cross-sectional area of as-fabricated plenum (m^2).

With $A^{hot} =$ $\delta A(\Delta T)\, A^{cold}$ and the assumption that ΔL is small compared to L, then

$$
\frac{V_p^{hot}}{V_p^{cold}} - 1 \approx \frac{L}{\Delta L}\Delta T\, (\alpha_{clad} - \alpha_{fuel})\, \delta A\, (\Delta T) \tag{4-61}
$$

where $\delta A(\Delta T)$ is the relative cross-sectional area of the hot plenum (related to cross-sectional area of the hot plenum).

Additionally, if $\delta A(\Delta T)$ is approximately independent of as-fabricated geometry (i.e., inner cladding radius) but only dependent on the temperature difference ΔT, a correction factor K_p can be defined to be

Fuel Rod

$$K_p = \frac{[V_p^{hot} V_p^{cold}] - 1}{[V_p^{hot} V_p^{cold}] - 1_{stnd}} = \frac{\dfrac{L}{\Delta L}}{\left(\dfrac{L}{\Delta L}\right)_{stnd}}$$ (4-62)

and the relative plenum volume for rods differing from standard geometries becomes

$$K_p = \frac{V_p^{hot}}{V_p^{cold}} = 1 + K_p (R_{p, stnd} - 1) \; .$$ (4-63)

Figure 4-8 shows the relative plenum volume, R_p, depending on the standard relative plenum volume $R_{p,stnd}$. The parameter shown in Figure 4-8 is the correction factor, K_p, ranging from 0.7 to 1.5.

For fuel void volumes, it is assumed that the relative fuel void volume predicted by the empirical correlations holds for varying as-fabricated geometries (i.e., pellet radii and/or inner cladding radii). Thus, no correction factor has been introduced for relative fuel void volumes.

The plenum volume is calculated using Equations (4-56) and (4-57), while the fuel void volume is calculated using Equation (4-59)
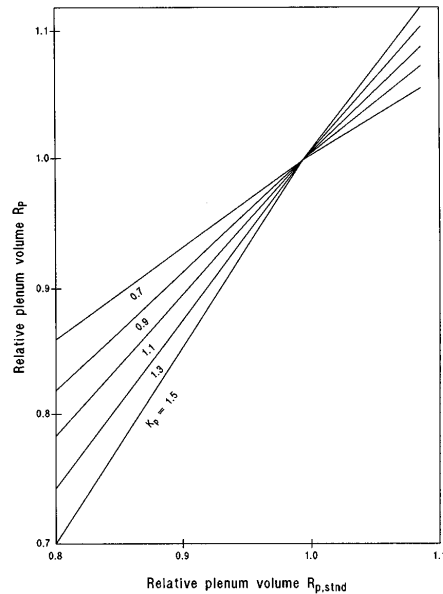
Figure 4-8. Relative plenum volume, R_p, depending on standard case $R_{p, stnd}$ and correction factor, K_p.

4.7 Fuel Rod Liquefaction and Relocation Model

The LIQSOL (LIQuefaction-flow-SOLidification) model calculates the change in fuel rod configuration due to meltdown and the oxidation and heat transfer occurring at the locations in a fuel rod at which liquefied cladding is slumping. Meltdown of fuel rods may have a significant impact on the subsequent damage progression that occurs in a reactor core. In some cases, meltdown may result in a rapid increase in

oxidation of the reactor core. In other cases, meltdown may result in blockage of coolant flow. The LIQ-SOL model is designed to calculate these important stages in damage progression. The LIQSOL model is designed to calculate the processes shown in Figure 4-9. Table 4-13 summarizes the processes that are modeled. First, the model calculates the rate of dissolution of fuel by the cladding. Then, the model determines the timing and the locations in the fuel rod where liquefied fuel and cladding breach the cladding oxide shell that contains the liquefied mixture. Last, the model calculates the downward movement of the mixture due to gravity and the configuration and rate of oxidation of the liquefied mixture.
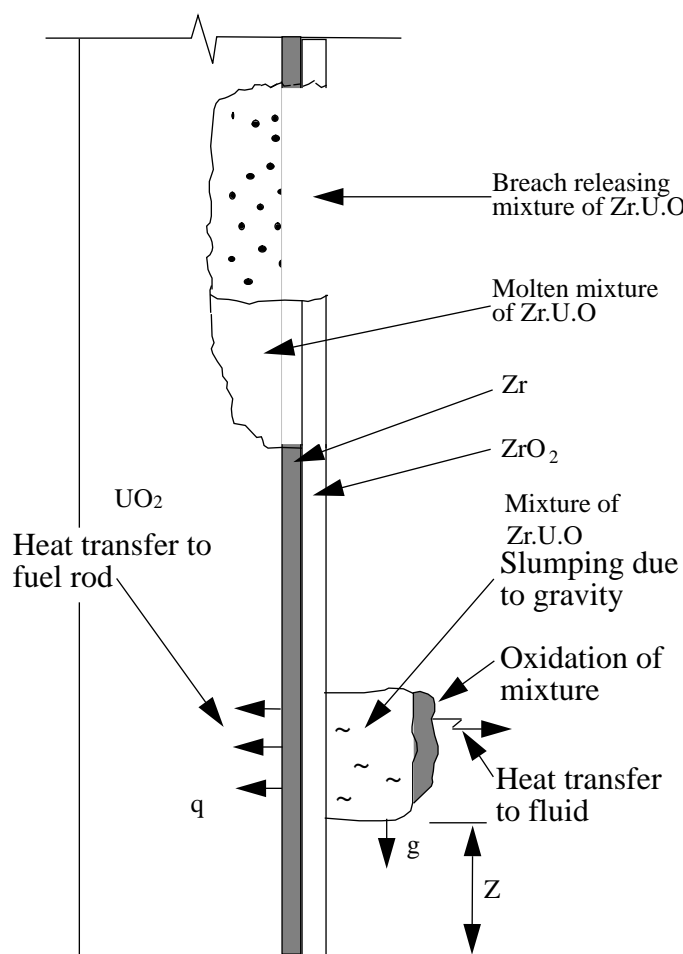
Figure 4-9. Processes occurring during meltdown of fuel rod.

The LIQSOL model is empirical in nature and is based on observations of the behavior of fuel rod meltdown. A theoretical analysis performed by Dussan and Chow[47] showed that a mechanistic model for the motion of a drop flowing down a surface in response to gravity requires correlations of contact angles as a function of the velocity of the drop. These correlations of the advancing and receding contact angles as a function of velocity are not available for a mixture of Zr-U-O flowing down the surface of a fuel rod. Thus an empirical model of the configuration and motion of drops of Zr-U-O has been developed that is based on observations of meltdown during experiments that subjected fuel rods to severe damage. These observations are primarily obtained from the CORA experiments[48,49] and are supplemented by the results of PIE from other severe fuel damage experiments.[50, 51]

Table 4-13. Summary of processes modeled by LIQSOL.

Process being modeled →	1. Dissolution of fuel by Zr	1. Configuration of liquefied material (array of drops)	1. Transfer of internal energy drom drops to fuel rod at moment of freezing	1. Transfer of internal energy from drops to spacer drop to spacer grid and fuel rods
	2. Durability of oxide shell	2. Motion of drops	2. Additional heat capacity of cladding due to frozen drops	2. Changes in configuration from drops to cohesive debris
		3. Oxidation of drops	3. Additional oxidation due to frozen drops	3. Additional heat capacity of fuel rod due to contact with cohesive debris
		4. Heat transfer from drops to fuel rod and fluid		4. Additional heat generation in fuel rod due to oxidation of cohesive debris
		5. Temperature change of drops		
Stage of meltdown →	Liquefied cladding and fuel contained by oxide shell	Liquefied material slumping down fuel rod	Frozen drops	Impact of drops with spacer grid

An example of the configuration of a fuel rod that was subjected to meltdown is shown in Figure 4-10. This figure was taken during a post test examination of the fuel bundle for the CORA-13 experiment[49]. A summary of the observed characteristics of fuel rod meltdown are listed in Table 4-14. The most significant characteristic is that the slumping material is in the configuration of drops. A schematic of the configuration of the slumping material is shown in Figure 4-11. The definition of the contact angles in an individual drop are shown in Figure 4-12. Another significant characteristic is that the material slumps at a velocity of only about 0.025 m/s. This slow velocity indicates that the drops are subjected to a large amount of flow resistance.

Several simplifying assumptions are applied to develop the LIQSOL model. These assumptions are summarized in Table 4-15 and are based upon observations of fuel rod behavior obtained from severe fuel damage experiments.[48,49,50,51] The most significant assumption is that liquefied fuel and cladding do not flow downward inside the cladding. This assumption is considered valid for unballooned fuel rods. For a case of liquefied fuel and cladding in a ballooned region, the assumption may not be valid if the fuel is uncracked and a large fuel cladding gap exists. In this case, liquefied cladding is expected to flow downward inside the fuel rod and collect at the elevation at which the fuel cladding gap is small enough to block the flow. However, if the fuel is cracked due to power cycling, the gap may be filled with fuel fragments,
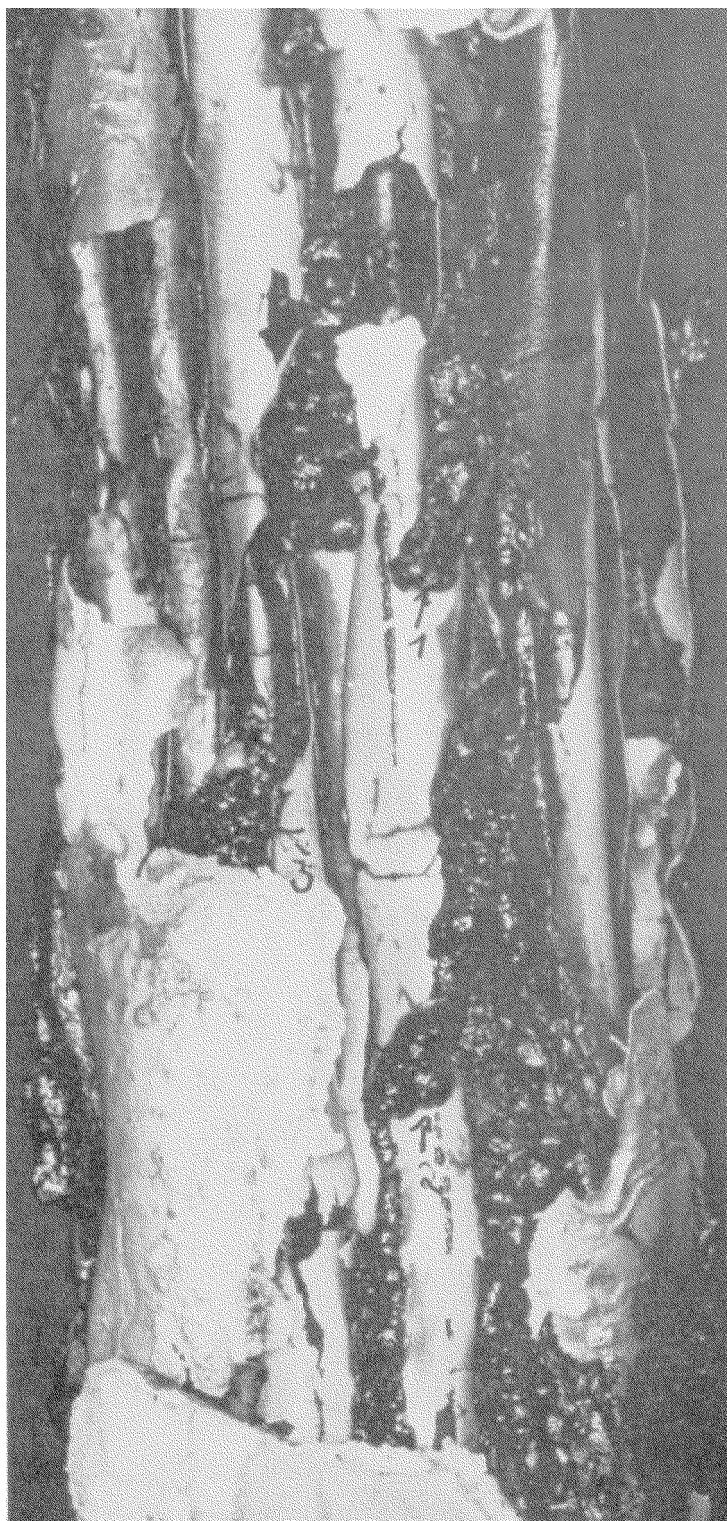
Figure 4-10. Posttest view of bundle CORA-13.

View from front   View from side

Fuel rod

Drop of
liquefied
material

M253-BDR-0692-004
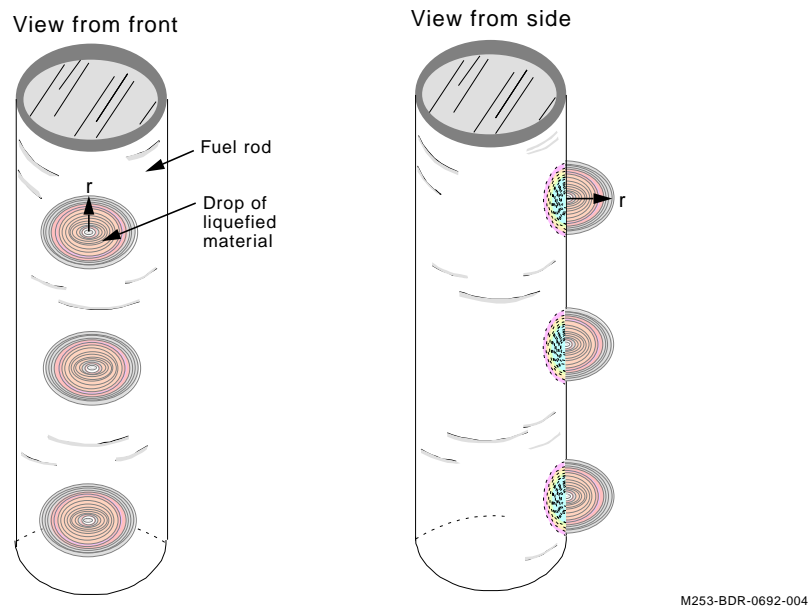
Figure 4-11. Configuration of slumping material.

which should inhibit the relocation of liquefied cladding within the gap.

Table 4-14. Characteristics of fuel rod meltdown.

Identification Number	Characteristic
1	Relocated material is in the configuration of drops
2	Drops slump at rate of about 0.025 m/s.
3	Advancing contact angle is about 100 degrees.
4	Receding contact angle is about 80 degrees.

The framework for the LIQSOL model, illustrated in Figure 4-13, is the stack of axial zones into which a fuel rod has been divided by the code user. The cladding temperatures and thicknesses of the cladding zirconium and ZrO_2 layers are input to the model. The first axial zone is defined to be at the bottom, and the last axial zone is defined to be at the top of the fuel rod. The bottom of the fuel pellet stack is defined to have an elevation of zero.

The LIQSOL model performs calculations in three steps. The first step calculates where the cladding and fuel have been liquefied. The second step calculates where and when the cladding oxide shell is breached. The third step calculates the configuration and the relocation of the liquefied cladding and fuel that flows through a breach, down the outside surface of the fuel rod, and solidifies.
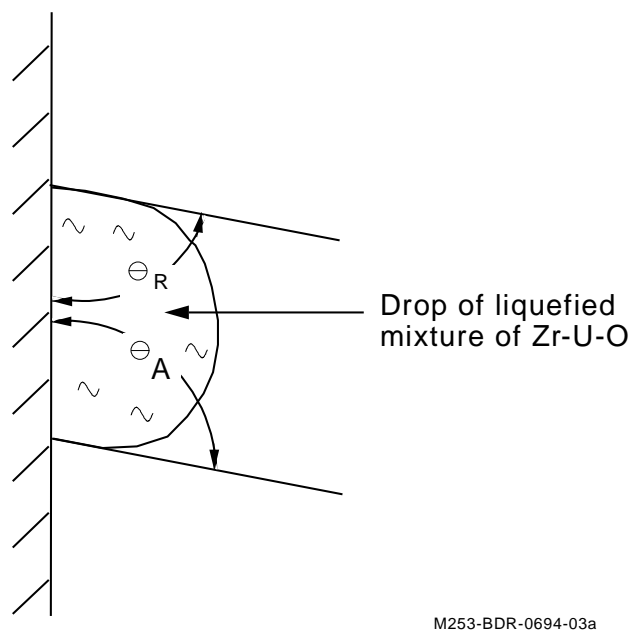
Figure 4-12. Configuration of drop of liquefied material suspended on surface of fuel rod.
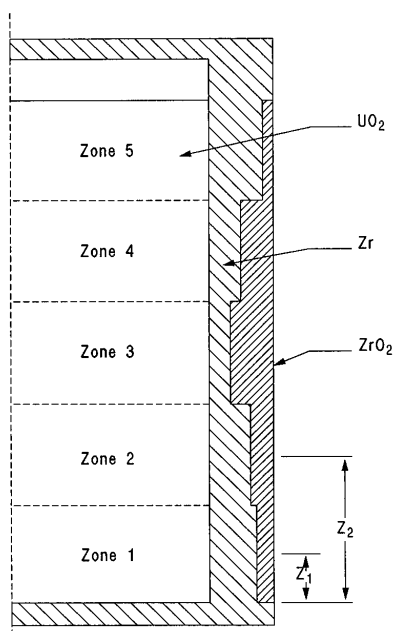
Figure 4-13. Framework of LIQSOL calculations.

Table 4-15. Simplifying assumptions in LIQSOL model.

Number	Assumption
1	Inside surface of cladding is in contact with outside surface of fuel pellet. Liquefied Zr-U-O does not flow downward inside the cladding.
2	If temperature of oxide layer on cladding is less than 2,600 K, then oxide layer contains melted cladding. If temperature exceeds 2,600 K, oxide layer fails and releases melted and liquefied cladding and fuel. However, if cladding is more than 30% oxidized when its temperature first exceeds 2,600 K, then oxide layer does not fail until its melting temperature is reached.
3	Rapid cooling of fuel rod results in cracks in cladding oxide layer and release of liquefied material contained by oxide layer.
4	Drops of slumping material are in shape of hemisphere.
5	Intact spacer grid blocks drops of slumping material and causes slumping material to change into configuration of horizontal layer of cohesive debris.

4.7.1 Cladding and Fuel Liquefaction

This step calculates the amount and position of liquefied Zr-U-O contained by the ZrO_2 layer on the outside of the cladding. The calculations are performed in the sections of the fuel rod with no breach in the ZrO_2 layer. The dissolution kinetics calculations assume that, at a given temperature, energy is neither given up or absorbed.

The amount of liquefied zirconium in an axial zone of the fuel rod is calculated by the equation

$$W_{zk} = \begin{cases} \pi\left[(r_{ik} + t_{zk})^2 - r_{ik}^2 \right]\Delta z_k \rho_z & \text{for } T_{sk} \geq T_{Lz} \\ \\ 0 & \text{for } T_{sk} < T_{Lz} \end{cases} \tag{4-64}$$

where

W_{zk}	=	mass of liquefied zirconium in axial zone k of fuel rod (kg)
r_{ik}	=	inside radius of cladding in axial zone k (m)
t_{zk}	=	thickness of unoxidized portion of cladding in axial zone k (m)
Δz_k	=	height of axial zone k (m)
ρ_z	=	density of unoxidized portion of cladding (kg/m^3)
T_{sk}	=	cladding temperature in axial zone k (K)
T_{Lz}	=	liquidus temperature of zirconium (K).

The number of molecules of liquefied zirconium in an axial zone is calculated by the equation

$$N_z = 1000 N_A \frac{W_{zk}}{A_z} \qquad (4\text{-}65)$$

where

N_z	=	number of molecules of liquefied zirconium
N_A	=	Avogadro's number (molecules/g-mole), 6.0238×10^{23}
W_{zk}	=	mass of liquefied zirconium (kg)
A_z	=	atomic weight of zirconium (91.2, amu).

Liquefied zirconium dissolves UO_2 that it contacts. The dissolution begins at the outside surface of the fuel pellet and propagates as a front inward toward the fuel center. A model for the rate of dissolution was obtained from Hofmann, et al.[46] This model calculates fuel dissolution by the equations

$$P_2 = 35.8 + \sqrt{(P_1 - 35.8)^2 + 1.0196 \times 10^{15} e^{\left(-\frac{677200}{RT}\right)} \Delta t} \qquad (4\text{-}66)$$

$$W_u = P_2 \frac{W_z}{(100. - P_2)} \qquad (4\text{-}67)$$

$$r_{m2} = \sqrt{r_p^2 - \frac{W_u}{(\rho_u \Delta Z \pi)}} \qquad (4\text{-}68)$$

where

P_2	=	weight percent of UO_2 at end of time step in mixture of U-Zr-O resulting from fuel dissolution by liquefied zirconium
P_1	=	weight percent of UO_2 at start of time step
R	=	universal constant (8.314 J/kg-mole $\cdot$ K)
Δt	=	time step (s)
W_u	=	mass of UO_2 dissolved at an axial node (kg)
W_z	=	mass of zirconium liquefied at an axial node (kg)
r_{m2}	=	outer radius of undissolved fuel at end of time step at an axial node (m)
r_p	=	outer radius of fuel prior to fuel dissolution (m)
ρ	=	density of fuel (kg/m^3)

ΔZ　　$=$　　height of an axial node (m).

The calculated amount of fuel dissolution is limited to the amount at which equilibrium occurs as determined by the solidus line in the ternary phase diagram. The calculation of this limit to the fuel dissolution is explained in Volume IV.

4.7.2　Breach of Cladding Oxide Layer

This step calculates whether or not a breach of the cladding surface ZrO_2 layer occurs during the time step. If no breach occurs, then no relocation of liquefied fuel and cladding is calculated. If a breach occurs, then liquefied fuel and cladding pour out of the breach and the position at which the mixture solidifies is calculated.

A criterion based on defined parameters is used to determine whether or not a breach occurs in a shell of cladding oxide that holds liquefied fuel and cladding. Variables in the criterion are temperature and extent of oxidation. The criterion is expressed by the logical operations

$$\left.\begin{array}{c} \text{if } T_{ox} > T_{fail} \text{ and } f_{ox} < f \\ \text{or} \\ \text{if } T_{ox} > T_{melt} \\ \text{or} \\ \text{if } T_{ox} > T_{zrm} \text{ and } h_{ox} \leq 1 \times 10^{-5} \end{array}\right\} \text{ then breach} \qquad (4\text{-}69)$$

where

T_{ox}	$=$	temperature of oxide shell (K)
T_{fail}	$=$	defined failure temperature of oxide shell, 2,600 (K)
f_{ox}	$=$	fraction of cladding oxidized at location at which the possibility of cladding breach is being evaluated
f	$=$	defined extent of oxidation beyond which oxide shell does not breach even if its temperature exceeds the failure temperature, 0.30
T_{melt}	$=$	temperature at which oxide shell melts (~ 2,950 K)[a]
T_{zrm}	$=$	melting temperature of metallic zircaloy (2,125 K)[a]
h_{ox}	$=$	thickness of oxide layer (m).

The rapid cooling of hot fuel rods may also cause breaches to form in the oxide layer on the outer surface of the cladding. These breaches form as a result of the differential contraction of the cladding and fuel as the cladding is initially cooled. The cladding cools much faster than the fuel but is constrained from contracting due to contact with the fuel. As a result, a large axial stress is produced in the cladding that

---

a. From MATPRO subroutine PLIQ.

causes cracking of the oxide layer and then the release of liquefied material contained by the oxide layer. An empirical model is used to determine the time and location at which the oxide layer on the surface of the cladding cracks due rapid cooling of the fuel rod. The model is based on the results of experiments in which hot fuel rods were subjected to reflood. This model is described in Section 3.2.

4.7.3 Configuration and Relocation of Liquefied Zr-U-O

This step of the modeling calculates the configuration and relocation of liquefied Zr-U-O that pours through a breach in the ZrO_2 layer and slumps downward until solidifying. The configuration of the slumping material is taken into account in calculating the oxidation of the slumping material. The relocated material that is released by a breach is assumed to be configured as an array of drops, as has been previously shown in Figure 4-11.

The size of each drop of slumping material is calculated based on the application of lubrication theory by Dussan and Chow.[47] According to their analysis, the area of surface wetted by a drop is

$$A_s = \frac{8\varepsilon\Theta_A\sigma}{\rho g \sin\gamma} \tag{4-70}$$

where

A_s =   area of surface wetted by drop (m^2)

Θ_A =   advancing angle of contact between drop and surface of fuel rod (radians)

σ =   surface tension (N/m)

ε =   1. - Θ_R/Θ_A

Θ_R =   receding angle of contact between drop and surface of fuel rod (radians)

ρ =   density of drop (kg/m^3)

g =   acceleration of gravity (9.8 m/s^2)

γ =   angle of inclination of surface ($\pi/2$)

In order to calculate the radius of the drops, two simplifying assumptions are required. The first assumption is that the drops are in the shape of a hemisphere. The second assumption is that the area wetted by moving drops is 10% larger than the area wetted by static drops. The radius of the drops is then related to the wetted area by the equation

$$\pi r_d^2 = 1.1 A_s \tag{4-71}$$

Substituting in A_s its value from Equation (4-70) and solving for r_d, the result is

$$r_d = 1.67 \left[\frac{\varepsilon\Theta_A\sigma}{\rho\gamma} \right]^{0.5} \tag{4-72}$$

For values of wetting angles shown in Table 4-16, a value of 0.45 N/m for surface tension and a drop density of 7000 kg/m^3, the value of r_d is calculated to be 2.5 mm. This value is in agreement with the size of the drops observed in fuel rod meltdown experiments, as shown in Figure 4-12.

The volume of drops is calculated by the equation

$$V_d = \frac{2}{3}\pi r_d^3 \tag{4-73}$$

where

      r_d =   radius of hemisphere that represents drop [effective radius of drop] (m)

The number of drops of slumping material per fuel rod per unit elevation resulting from the breach of liquefied material at an axial node is calculated by the equation

$$N_{dn} = \frac{\pi (r_{on}^2 - r_{dn}^2)}{V_d} \tag{4-74}$$

where

      N_{dn} =   number of drops of liquefied fuel rod material per fuel rod per m of elevation at axial node n

      r_{on} =   outer radius of annulus of liquefied material in fuel rod at axial node n(m)

      r_{dn} =   inner radius of annulus of liquefied material inside fuel rod at axial node n(m)

The oxidation of the drops of Zr-U-O on the outside surface of the fuel rod may result in a significant amount of heat generation. The oxidation of the drops initially occurs very rapidly because hot metallic material is released from the protective oxide shell on the cladding surface and exposed directly to steam. The heat generation in the fuel rod due to oxidation is calculated based on the configuration shown in Figure 4-14. The oxidation of the portion of the surface of the fuel rod that is covered with drops is represented by the drop oxidation model and the oxidation of the uncovered portion of the fuel rod is represented by the oxidation model for intact fuel rods. Drops are identified according to the axial node at which they originated. This distinction takes into account the different extents of oxidation of drops that have different times of origin. When a breach occurs at an axial node, all of the liquefied material inside the fuel rod is assumed to simultaneously be released to the surface of the fuel rods and to obtain the configuration of drops. Thus the number of different origins of drops on a fuel rod is less than or equal to the number of axial nodes in the fuel rod.

The calculation of the oxidation at an axial node with drops of relocated material is performed in four steps. First, the change in weight gain per unit surface area of drop is calculated. This calculation takes into account the limitation on the rate of mass transfer. Second, the rate of heat generation for each drop is calculated. Third, the sum of the heat generation due to oxidation of drops at an axial node is calculated and added to the heat generation term for the axial node of the fuel rods with the drops. Fourth, the area of the surface of the axial node that is not covered with drops is calculated and applied to calculate the heat generation due to oxidation of the uncovered portion of the cladding. The equations applied in these four steps
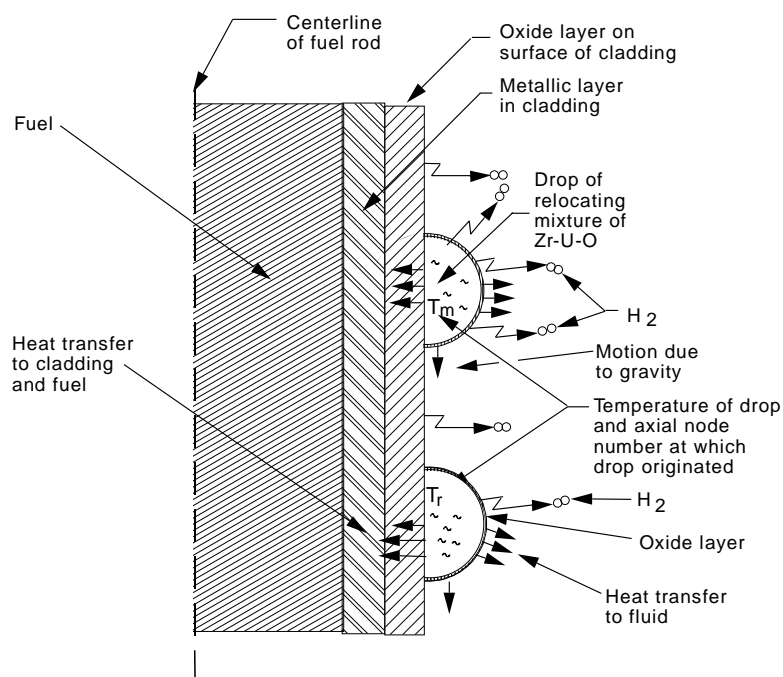
M259-BDR-0694-002

Figure 4-14. Cross section of fuel rod with oxidation of relocating material and intact section of fuel rod.

of calculations are described next.

The change in weight gain per unit surface area of a drop during a time step is calculated by the equation

$$w_{dkn1} = (w_{dkn0}^2 + k_{eff}\Delta t)^{0.5} \tag{4-75}$$

where

w_{dkn1}	=	weight gain of oxygen per unit surface area at end of time step for drop that originated at n-th axial node and is now located at k-th axial node (kg O_2/m^2)
w_{dkn0}	=	same as wdkn1 but for start of time step
k_{eff}	=	effective parabolic rate constant [(kg/m^2)^2/s]
Δt	=	time step (s)

The value of k_{eff} in the above equation is calculated taking into account the temperature of the drop and the composition of the mixture of Zr-U-O in the drop. The value of k_{eff} is calculated by Equation 3-14 in Section 3.3. The weight gain is limited to the maximum mass transfer that can occur. This maximum transfer is calculated by Equation 3-10 of Section 3.1.

The rate of heat generation per unit surface area of drop is calculated by the equation

Fuel Rod

$$Q_{dkn} = H_{eff} \left(\frac{w_{dkn1} - w_{dkn0}}{\Delta t} \right) \tag{4-76}$$

where

Q_{dkn} = heat generation per unit surface area of drop located at k-th axial node and that originated at the n-th axial node (W/m^2)

H_{eff} = effective heat of reaction for drop (J/kg of oxidized Zr and UO_2)

The value of H_{eff} is calculated taking into account the composition of the drop; it is calculated by the equation

$$H_{eff} = \left((1-f) \cdot H_{Zr} \cdot \frac{A_{wZr}}{A_{wO2}} + f \cdot H_{UO_2} \cdot \frac{A_{wU}}{A_{wO_2}} \right) \tag{4-77}$$

where

H_{eff} = effective heat of reaction (J/kg of oxidized Zr and UO_2)

H_{zr} = heat of reaction for Zr (6.45×10^6 J/kg of Zr converted to ZrO_2)

A_{wZr} = atomic weight of Zr (91.22)

A_{wO2} = atomic weight of O_2 (32)

H_{UO2} = heat of reaction of UO_2 as obtained from MATPRO (7.84×10^5 J/kg of $(UO_2)_3$ converted to U_3O_8)

A_{wU} = atomic weight of $(UO_2)_3$ (810)

f = mass fraction of UO_2 in mixture of relocated material.

The sum of the heat generation due to oxidation of drops is then calculated by the equation

$$q_{totk} = \sum_1^{n_{tot}} N_{dn} 2\pi r_{dn}^2 Q_{dkn} \tag{4-78}$$

where

q_{totk} = total heat generation due to oxidation of drops of relocated material that are at axial node k (W)

n_{tot} = number of different axial nodes of origin of drops of relocated material that are located at axial node k

r_{dn} = effective radius of drops that originated at axial node n (m).

The rate of oxidation of intact cladding is adjusted to account for the covering of intact cladding by drops of relocated material. The rate of oxidation is multiplied by the ratio of the surface area not covered by drops to the total surface area. This multiplier is calculated by the equation

$$F_{dk} = 1 - \sum_{1}^{n_{tot}} \pi N_{dn} r_{dn}^2 / 2\pi r_k \Delta z_k \tag{4-79}$$

where

F_{dk} = multiplier applied to rate of oxidation for intact fuel rods at axial node k

r_k = outside radius of fuel rods at axial node k (m)

Δz_k = height of axial node k (m).

The decrease in elevation of drops during a time step is calculated by the equation

$$z_{dn2} = z_{dn1} + u_d \Delta t \tag{4-80}$$

where

z_{dn2} = elevation at end of time step of drop that originated at axial node n (m)

z_{dn1} = elevation at start of time step of drop that originated at axial node n (m)

u_d = velocity of drop (m/s)

Δt = size of time step (s).

According to the analysis of Dussan and Chow[47] the downward velocity of a drop is approximately calculated by the equation

$$u_d = \frac{3.395 \, (1 - \Theta_R / \Theta_A)}{(1/\lambda_A + 1/\lambda_R)} \, (f_{wet} - 1) \tag{4-81}$$

where

u_d = downward velocity of drop (m/s)

λ_A = $du_d / d\Theta_a$ = rate of change of velocity with respect to change in advancing contact angle ((m/s)/radian).

λ_R = $du_d / d\Theta_a$ = rate of change of velocity with respect to change in receding contact angle ((m/s)/radian).

f_{wet} = ratio of area of surface wetted by moving drop to area of surface wetted by static drop. As stated for Equation 4-71, this value is assumed to be equal to 1.1.

The equation above cannot be applied in practice to calculate the velocity of the drop because of unknown fluid properties, namely λ_A and λ_R. As a result the velocity of drops must be obtained from experimental results.

A limited survey of experimental results showed that the average velocity of a moving drop to be about 0.025 m/s. The data is currently too limited to establish a correlation of velocity with parameters such as drop temperature and the composition of the drop. So the debris oxidation model will determine

the velocity of the drop by the following simple criterion:

$$u_d = 0.025 \text{ for } T_{kn} > T_{sol} \tag{4-82}$$

$$u_d = 0.0 \text{ for } T_{kn} < T_{sol} \tag{4-83}$$

where

T_{kn}	=	temperature of drops at axial node k that originated at axial node n (K)
T_{sol}	=	solidus temperature of material in drops (K).

Since further analyses and experiments may indicate that adjustments should be made to the average velocity of the drops, the option is provided for the user definition of the average velocity.

The experimentally determined value of drop velocity can be compared with the theoretical value calculated on the basis of assumed values for λ_A and λ_R in Equation 4-80. Since the change in contact angles with respect to velocity has not been measured the contact angles are conjectured to linearlly increase by a value of $\pi/36$ as the velocity of the drop changes for 0 to 0.025 m/s. With these changes in contact angle with respect to velocity,

$$\lambda_A = \lambda_R = 0.025 / (\pi/36) = 0.286((m/s)/radian).$$

Substituting these values into Equation 4-81 and using the MATPRO values for σ of 0.45 N/m and for ρ of 7000 hg/m^3, the theoretical value of u_d is calculated to be 0.01 m/s compared with the experimentally determined value of 0.025 m/s. In view of the large uncertainties in material properties, the theoretical and experimentally based values are considered to be in fair agreement and the assumption made to calculate the size of drops was not unreasonable. This assumption was that the wetted surface area of a moving drop is 10% larger than that for a static drop.

The temperature of the drops is calculated taking into account the heatup of the drop due to oxidation and the transfer of heat from the drop to the substrate on one side of it and to the fluid on the other side of it. The heat transfer process that is modeled is shown in Figure 4-15 and Figure 4-16. The set of equations used to calculate the transient temperature of the drops is shown in Table 4-16. The variables in the equation set are defined in Table 4-17. A temperature wave propagates into an axial slice of the fuel rod beginning at the instant the drop of relocating material contacts the surface of the axial slice. The amount of heat transferred into the axial slice is calculated using the integral method.[53] The transient heat flux at the surface of the axial slice is calculated assuming that the temperature of the surface changes from T_c to T_d at the instant that the drop contacts the surface. The distance propagated by the temperature wave is proportional to the square root of time. The first equation in Table 4-16, the equation for cover time, calculates the length of time the axial slice is covered by the flowing mixture. The heat equation, namely that for Q_{l1}, calculates the amount of heat that is conducted into the axial slice from the time the leading edge on the drop contacted the surface of the slice to the time that the receding edge covered the surface of the slice. The next equation, namely that for Q_{l2}, calculates the amount of heat that was transferred from the drop to the surrounding fluid during the time that the drop covered the axial slice. The next equation, namely that

for Q_g, calculates the heat generation in the drop. The last equation calculates the temperature change of the drop during the SCDAP/RELAP5 time step. The heat transfer from the drop to its cladding substrate is accounted for by the heat conduction model of the intact fuel rod; the heat generation term for the cladding includes the heat transfer from the drop to the cladding. The term that accounts for the transfer of heat from the fuel rod to the fluid is incremented to account for the heat transfer from the drop to the fluid.
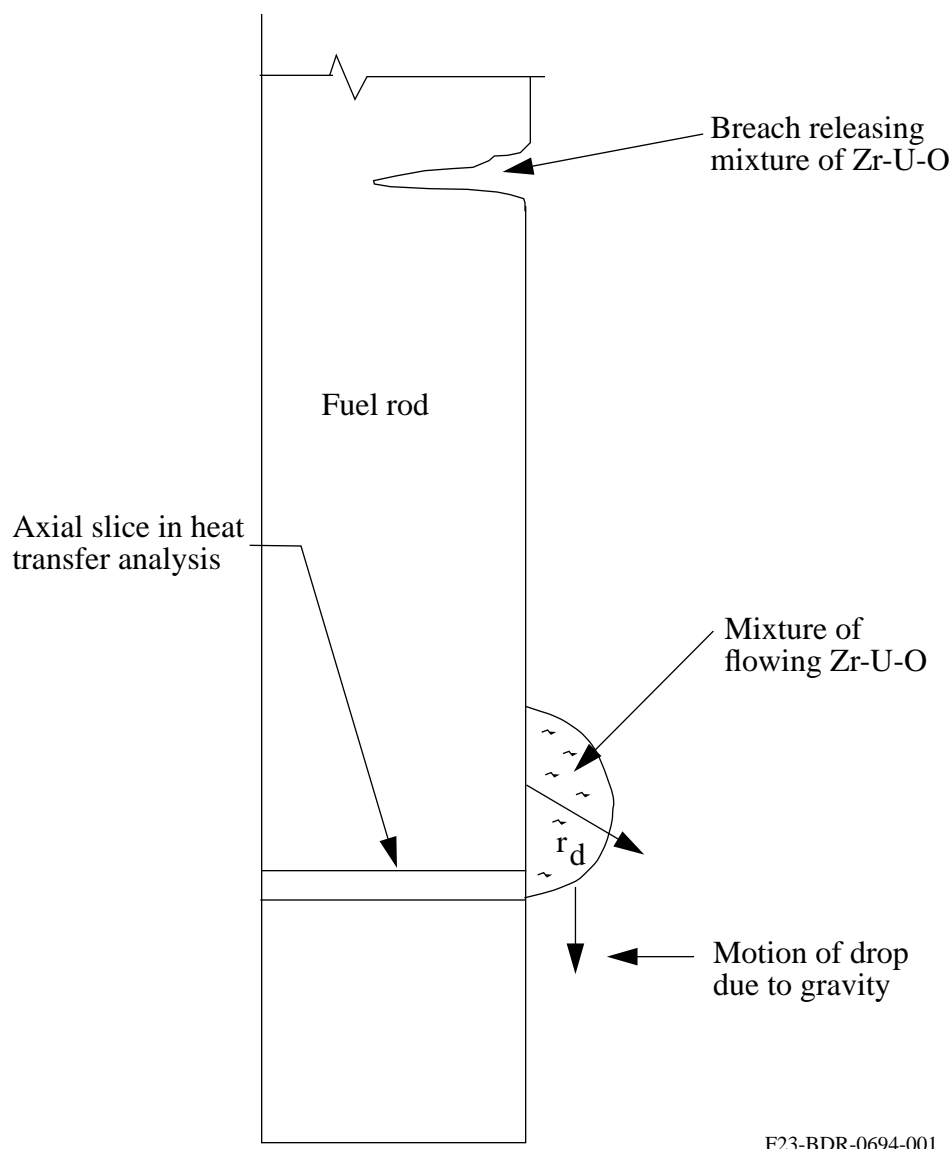
Figure 4-15. Frame of reference for LIQSOL equations in Table 4-15.

After the drop has frozen and become static, the drop is represented as being part of the cladding.

Fuel
Cladding Zr layer
Cladding ZrO_2 layer
Flowing mixture of Zr-U-O

q_1

Time = t_1

T_d

Temperature

T_c

r_1 Radius r_o

q_2

Time = t_2

T_d

Temperature

T_c

r_1 Radius r_o
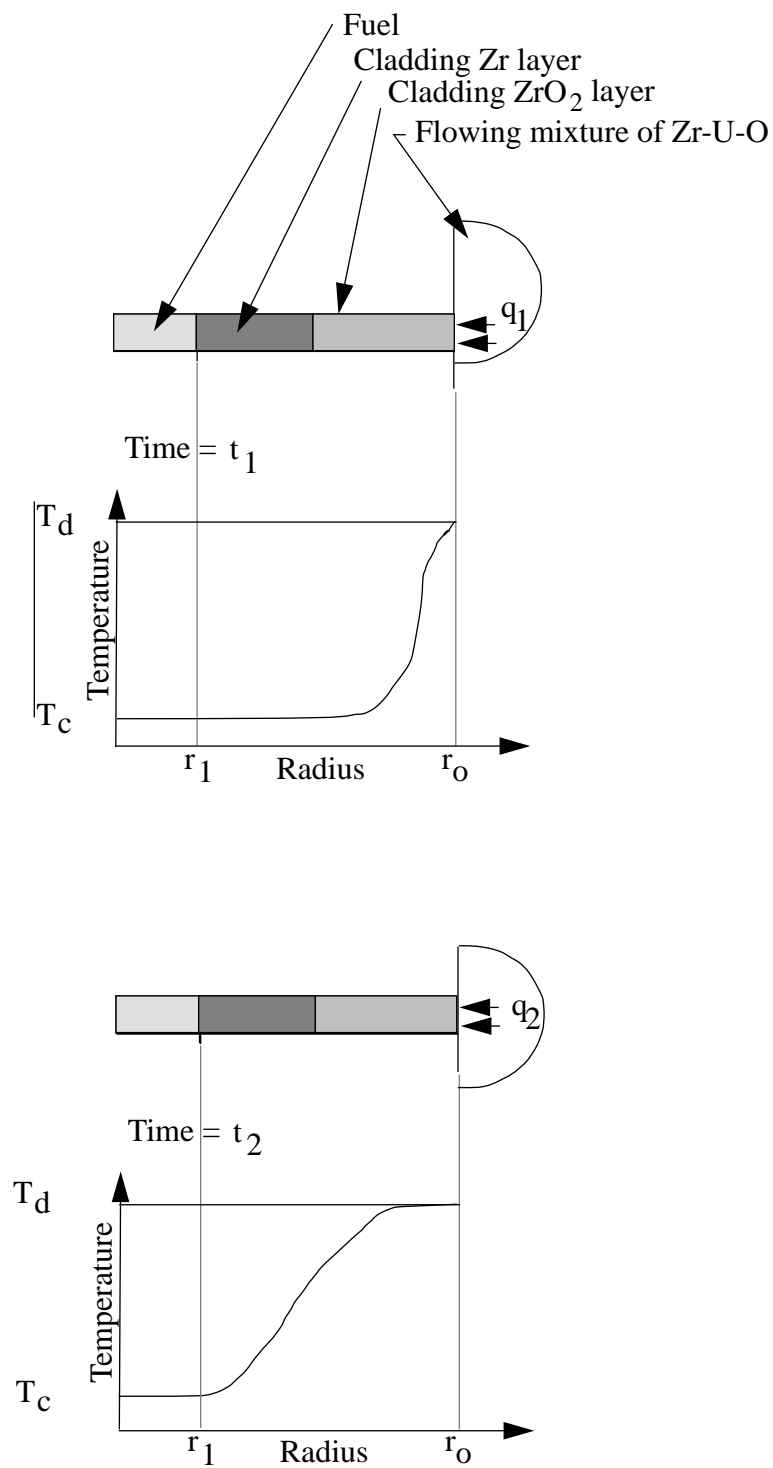
F23-BDR-0694-002

Figure 4-16. Heat transfer from flowing mixture into axial slice of fuel rod.

Table 4-16. Equation set for calculation of temperature of drop of relocating material .

Phenomenom modeled	Equation
Time that surface is covered with drop	$$\Delta t_c = \frac{\sqrt{\pi r_d}}{u_d}$$
Heat loss by conduction into fuel rod during cover time	$$Q_{l1} = 7.69 r_d^2 (T_D - T_C) \left[(\rho_o C_{po} K_o)^{0.5} + \frac{0.5}{po} + (\rho_c c_{pc} k_c)^{0.5} (t_{pc}^{0.5} - t_{po}^{0.5}) + (\rho_f c_{pf} k_f)^{0.5} (\Delta t_c^{0.5} - t_{pc}^{0.5}) \right]$$
Time for penetration of heat through cladding oxide	$$t_{po} = h_o^2 / \alpha_o$$
Time for penetration of heat through metallic layer of cladding	$$t_c = h_c^2 / \alpha_{oc}$$
Heat loss by convection and radiation to fluid	$$Q_{l2} = 2\pi r_d^2 [h_s (T_d - T_s) + F_g \sigma (T_d^4 - T_s^4)] \Delta t_c$$
Gray body factor	$$F_g = 1 - \exp(-a_g p_s p)$$
Total heat loss during time step	$$Q_{lt} = (Q_{l1} + Q_{l2}) (\Delta t / (\Delta t_c))$$
Heat generated by oxidation during time step	$$Q_g = 2\pi r_d^2 Q_{dkn} \Delta t$$
Temperature change of drop during time step	$$\Delta T_{mix} = \frac{1.5}{\pi r_d^3 \rho_d C_d} (Q_g - Q_{lt})$$

First, the equilibrium temperature is calculated of the drop and the fuel rod at the axial node at which the drop solidified. This calculation of equilibrium temperature adds the internal energy of the drop to the fuel rod. The calculation of the equilibrium temperature is performed in the same way as the calculation of the equilibrium temperature at a location in which drops of slumping material are blocked by a spacer grid; this calculation is described in Section 4.8.3 of this report. The subsequent representation of the drop is performed by the heat conduction model for intact fuel rods. The heat capacity of the drop is taken into account in calculating the effective heat capacity of the cladding. The oxidation of the drop is taken into account in calculating the oxidation of the cladding. If the drop heats up to the point of liquefaction, then the drop is calculated to move in response to gravity and the temperature of the drop is again calculated by the set of equations shown in Table 4-16.

Moving drops that encounter a spacer grid are assumed to be blocked by the spacer grid and then to self-level into a layer of cohesive debris that completely fills in the space between the fuel rods at the location of the spacer grid. The physical situation that results from the blockage of drops by spacer grids is shown in Figure 4-17. At the moment of impact the equilibrium temperature is calculated of the drops and the axial node with the impacted grid spacer. This equilibrium temperature is calculated as described in Section 4.8.3 of this report. Subsequently, the blocked drops of relocated material are represented by the heat conduction model for intact rods. The heat capacity of the drop is taken into account in calculating the effective heat capacity of the fuel rod at the location of the blockage. The oxidation of the top and bottom surfaces of the blockage is calculated and added to the heat generation term of the fuel rod. The heat generation per unit surface area of the cohesive debris is calculated using the same model as is used for the drops of relocated material. The change during the time step of the weight gain of oxygen in the cohesive debris per unit surface area and the heat generation in the cohesive debris per unit surface area are calculated by Equations 4-75 and 4-76, respectively. The heat generation due to oxidation over the entire surface area of the cohesive debris is calculated by the term
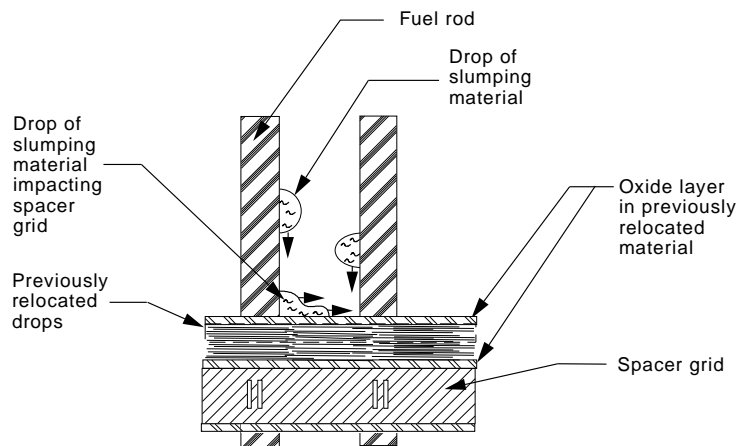
Figure 4-17. Blockage of drops of relocating material by spacer grid.

Definitions of symbols in Table 4-16.

Symbol	Units	Definitions
a_g	1/m•pa	Absorption coefficient
C_{pc}	J/kg•K	Heat capacity of metallic part of cladding
C_{pd}	J/kg•K	Heat capacity of Zr-U-O mixture in relocating drops
C_{po}	J/kg•K	Heat capacity of ZrO_2
F_g		Gray body factor
h_c	m	Thickness of metallic layer in cladding
h_o	m	Thickness of ZrO_2 layer in cladding
h_s	W/m^2•k	Convective heat transfer between drop of relocating material and steam
k_c	W/m•k	Thermal conductivity of metallic part of cladding
k_f	W/m•k	Thermal conductivity of UO_2
k_o	W/m•k	Thermal conductivity of ZrO_2
p	m	Pitch of fuel rods in reactor bundle
p_s	p_a	Pressure of steam surrounding drop
Q_{dkn}	W/m^2	Heat generation per unit surface area from oxidation of drop
Q_g	J	Total heat generation in drop due to oxidation during time step
Q_{l1}	J	Amount of heat loss by conduction into fuel rod from drop during time that drop slumps distance equal to its diameter

Definitions of symbols in Table 4-16. (Continued)

Symbol	Units	Definitions
Q_{l2}	J	Amount of heat loss from drop to fluid surrounding it during time that drop slumps distance equal to its diameter
r_d	m	Effective radius of drop of slumping material
r_o	m	Outer radius of fuel rod
Δt	s	Time step
Δt_c	s	Length of time that a given point on cladding surface is covered with drop of Zr-U-O mixture.
T_c		Temperature of cladding just prior to time at which cladding surface is covered by flowing mixture of Zr-U-O
T_d	K	Temperature of drop Zr-U-O mixture when its leading edge is at elevation z
T_s	K	Temperature of steam that surrounds drop
u_d	m/s	Velocity of drop
α_c	m^2/s	Thermal diffusivity of metallic part of cladding
	m^2/s	Thermal diffusivity of cladding oxide layer, $\dfrac{k_o}{\rho_o c_{po}}$
σ	$W/m^2 \bullet K^4$	Stefan-Boltzmann constant (5.668×10^{-8})
ρ_d	kg/m^3	Density of drop of relocating mixture of Zr-U-O

$$Q_{ck} = (p^2 - \pi r_{ok}^2) H_{eff} ((w_{ck1} - w_{ck0}) / (\Delta t)) \qquad (4\text{-}84)$$

where

4-56

Q_{ck} = heat generation at axial node k due to oxidation of cohesive debris in axial node k (W)

p = pitch of fuel rods (m)

r_{ok} = outer diameter of fuel rod at axial node k (m)

w_{ck1} = weight gain of cohesive debris at axial node k (kg O_2/m^2)

H_{eff} = effective heat of reaction of cohesive debris as calculated by Equation 4-77

(J/kg of oxidized Zr and UO_2).

The intact fuel rod heat conduction model applies as a heat generation term for the cladding the heat generation that is due to oxidation of the cohesive debris. The model also accounts for the reduction in surface area due to the blockage caused by the relocated material at the location of the spacer grid. The oxidation of the cladding and the convective and radiative heat transfer at the surface of the cladding are calculated using this reduced surface area.

4.8   Liquefaction of Fuel Rod Cladding at Location of Inconel Grid Spacer

Grid spacers can have a significant impact on the progression of damage in a reactor core during a severe accident. The configuration of grid spacers varies from reactor to reactor. One design of a grid spacer is shown in Figure 4-18. The grid spacers are made of either zircaloy or Inconel. The impact of grid spacers on damage progression has been revealed by out-of pile experiments in Germany[54,55,59] and Japan,[60] in-pile experiments at the PBF facility in Idaho,[61] and by examinations of the damaged TMI-2 core.[62] The experiments in Germany and Japan have revealed the existence of chemical interactions between Inconel and zircaloy that take place at temperatures as low as 1,273 K, more than 200 K lower than the melting temperature of Inconel. Thus in a reactor core with Inconel grid spacers, the meltdown of the core may begin at the location of the grid spacers. Also, the PBF experiments and the examination of the TMI-2 core have revealed that grid spacers trap slumping liquefied material. If the location at which the material is trapped is sufficiently cool, the material will solidify at the location of the grid spacer, resulting in a blockage to coolant flow. These various ways in which Inconel grid spacers influence damage progression have made it necessary to incorporate models for the interaction of grid spacers with fuel rods.
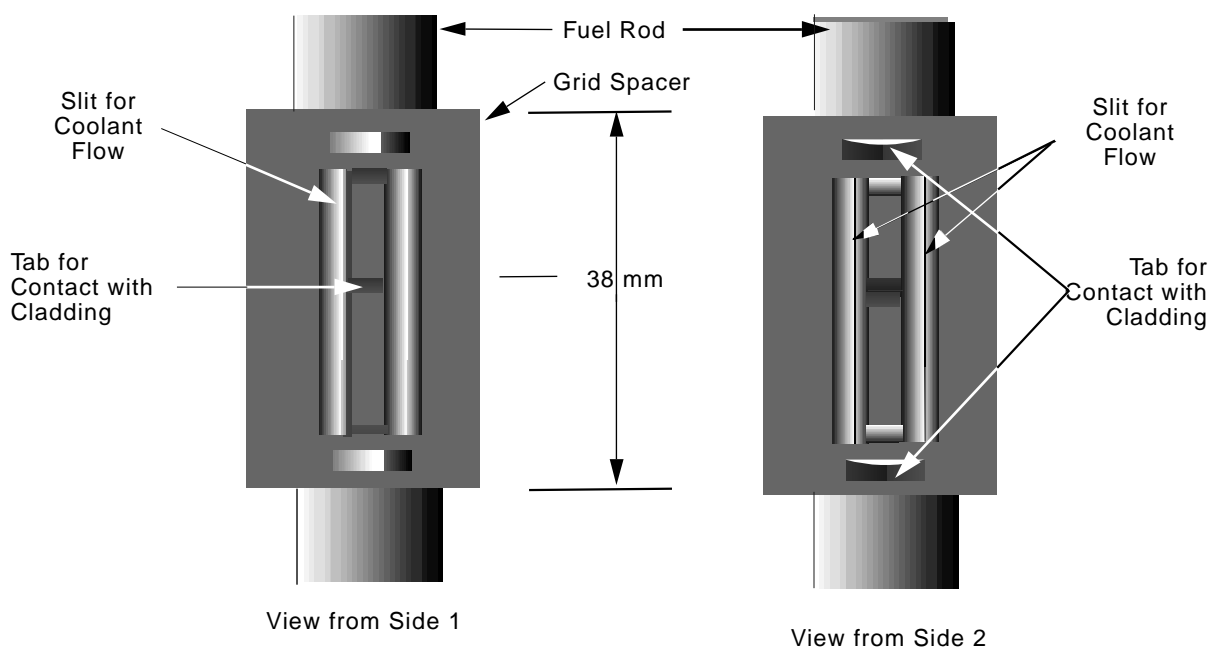
Figure 4-18. Configuration of grid spacer.

4.8.1 Impact of Grid Spacers on Damage Progression

Inconel grid spacers can influence the course of damage in a reactor core by: (a) reacting with fuel rod cladding so that it is weakened and can no longer contain the gases inside the cladding, (b) reacting with fuel rod cladding so that a large amount of cladding is liquefied and slumps, and (c) trapping slumping material and thus blocking coolant flow. These three ways in which Inconel grid spacers influence damage progression are discussed next.

The extent of ballooning of fuel rods in a reactor core can be a function of the timing and extent of the chemical reaction between Inconel grid spacers and the fuel rod cladding. For certain severe accident scenarios, the coolant pressure remains high until some time after the beginning of the chemical reaction between the grid spacers and fuel rod cladding. Fuel rod ballooning does not occur due to the large back pressure that the coolant applies to the fuel rods. If the pump seals then fail and leakage occurs, the coolant pressure will decrease to the point that cladding ballooning may occur. But the chemical reaction between Inconel and zircaloy may result in the weakening and failure of the cladding and thus the release of fuel rod gases prior to significant depressurization of the coolant. In this case, cladding ballooning does not occur.

Subsequent damage progression can be a strong function of whether the fuel rods have ballooned. If the fuel rods have not ballooned, the reactor core may continue to heat up at a moderate pace and the cladding may completely oxidize without experiencing any meltdown. But if the fuel rods have ballooned, the heatup may proceed at a rapid pace and the cladding may experience a significant amount of meltdown of metallic cladding and dissolved fuel.[63] Differences in the rate of heatup are due to differences in surface areas of the cladding for the two cases. In the case of the ballooned cladding, this surface area can be almost 2.6 times larger than when ballooning does not occur; as a result, the heat generated by oxidation is a factor of 2.6 times greater in the case of ballooned cladding. The factor of 2.6 is the result of the cladding

diameter increasing by up to a factor of 1.3 due to ballooning and the inside surface area of the cladding being exposed to steam after rupture, which doubles the surface area of the cladding that is oxidizing.[61] If the cladding does not begin to balloon until the outside surface of the cladding begins to rapidly oxidize and form an oxide skin that resists ballooning, then the diameter increase of the cladding may be less than 5 to 10%.[63]

The results of the CORA experiments, discussed in a companion paper,[64] show that even zircaloy grids with small Inconel tabs may cause a chemical reaction that liquefies a small part of the fuel rod cladding and causes a pin hole failure in the cladding.[65] In this case, the amount of material that liquefies is small, but the formation of the pin hole would result in the release fission products.

Cladding liquefied by chemical reaction with grid spacers will slump in response to gravity and relocate to a lower region of the reactor core. This slumping of liquefied material influences damage progression in several ways. First, the slumping of the cladding and the grid spacer material with which it has reacted results in the transfer of internal energy from a hotter part of the core to a cooler part of the core. This transfer of energy accelerates the heatup of the lower part of the core and brings this part of the core closer to the conditions for rapid oxidation. Second, the slumping material may be trapped at the location of the next grid spacer below it, solidify, and form a blockage to flow. Third, the extent of oxidation in the upper part of the core is reduced due to cladding slumping away from this region.

4.8.2 Liquefaction of Cladding at Location of Grid Spacers

This section presents models for calculating as a function of time the extent of liquefaction of fuel rod cladding and grid spacers due to chemical reaction between zircaloy and Inconel. The time at which this reaction begins is a function of the thickness of the oxide layer on the cladding and the rate of the reaction is a function of temperature.

The models are based on separate-effect experiments performed by Hofmann and his colleagues at the Kernforschungszentrum in Karlsruhe, Germany.[54] In these experiments, short rods composed of Inconel 718 (54 wt% Ni, 18 wt% Cr, 18 wt% Fe, 2.9 wt% Mo) were pressed into Zircaloy-4 capsules with an inner hole equal to the diameter of the Inconel rods. The oxide thickness on the inside surface of the Zr capsule was an experiment parameter. Experiments were performed on capsules with oxide layer thicknesses varying from 10 to 100 microns. The capsules were placed in a tube furnace with flowing argon and heated to varying levels of temperature (1,273 to 1,673 K) for varying periods of time. The capsules were then removed from the furnace and a measurement was made of the thickness of the reaction zone between the Inconel rod and the Zr capsule it interfaced. To measure the size of the reaction zones, the capsules were mechanically cut and metallographically prepared for examination with an optical microscope.

Correlations of the rate of reaction as a function of temperature and oxide thickness were obtained by linear regression using the method of least squares. Correlations as a function of oxide thickness and temperature were obtained of the delay in the initiation of the reaction caused by the oxide layer. The isothermal growth rates of the reaction zones were found to obey parabolic rate laws, indicating a diffusion-controlled process. The Zr in the zircaloy diffuses into the Inconel and the Ni in the Inconel diffuses into the zircaloy. For temperatures above 1,525 K, small amounts of Inconel were able to dissolve and liquefy large quantities of cladding.

Coefficients for the parabolic kinetics equation were derived from the experimental results to analytically describe the transient growth of the reaction zone on both sides of the interface between the Inconel and zircaloy. The configuration for which the parabolic kinetics equation applies is the one-dimensional slab shown in Figure 4-19. The equation used to determine the rate of growth of the reaction zone on each side of the interface is:

$$d_2 = \left[d_1^2 + A e^{\left[\frac{-B}{RT}\right]} \Delta t \right]^{0.5}$$
(4-85)

where

d_2 = position of boundary of reaction zone at end of time step (m)

d_1 = position at start of time step (m)

A,B = coefficients that vary with oxide thickness, temperature and whether the growth is being calculated in the Zr or Inconel field. These coefficients are defined in Table 4-17

R = universal gas constant [8.314 Pa.m^3/(g-mole $\cdot$ K)]

T = temperature of the reacting material (K)

Δt = time step (s).

The oxide (ZrO$_2$) layer between the metallic zircaloy and the Inconel was found to delay the start of the chemical reaction between the zircaloy and Inconel. The time to dissolve this layer and initiate the growth of the reaction zone into the metallic zircaloy is calculated by the equation

$$t_d = c_1 e^{\left[\frac{-c_2}{RT}\right]}$$
(4-86)

where

t_d = period of time for dissolution of the oxide layer (s)

T = temperature of cladding and grid spacer (K)

c_1, c_2 = coefficients defined in Table 4-18 and that are a function of oxide thickness.
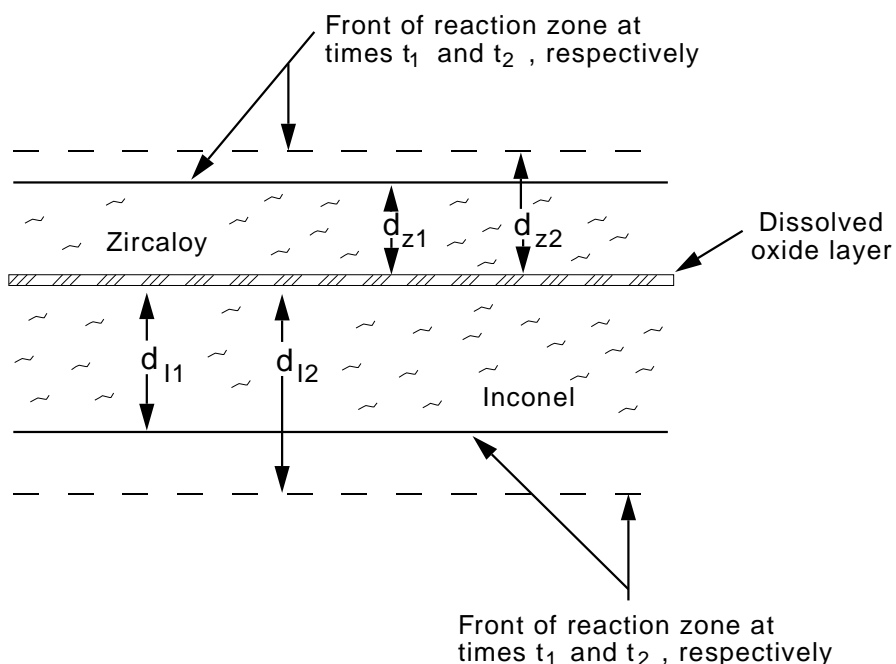
Figure 4-19. Configuration for which parabolic kinetics equation applies.

A method is next presented for applying Equation (4-85) to fuel rod cladding that interfaces with an Inconel grid spacer. Because the geometry of the two reacting materials in a fuel rod bundle is significantly different from the idealized geometry for which Equation (4-85) applies, two assumptions are required that simplify the calculation of the propagation of the reaction zone.

The first assumption is that the growth of the reaction zones in the grid spacer and cladding follows the paths shown in Figures 4-16 and 4-17. The reaction zone is assumed to first grow in a direction perpendicular to the surface of contact between the cladding and grid spacer. The cross sectional area of the reaction zone is assumed to stay equal to the area of contact until the reaction zone has propagated to the midplane of the grid spacer panel (line of symmetry between two adjacent fuel rods). After propagating through the thickness of the grid spacer panel, the reaction zone spreads as a circle with an increasing radius through the grid spacer panel. The propagation through the cladding is assumed to follow a similar path as shown in Figure 4-17. The reaction zone first propagates outward from the surface of contact in a perpendicular direction until the entire thickness of the cladding has reacted at the location of contact. Then the reaction zone grows at an equal rate in the circumferential and axial directions. After the reaction zone has spread around the entire circumference, the reaction zone then grows only in the axial direction. Due to the cladding contacting the grid spacer at four symmetrically located points, the propagation of the reaction zone in the circumferential direction is complete when the angle in Figure 4-17 equals $\pi/4$.

Table 4-17. Value of coefficients in equation for growth of reaction zone.

Oxide thickness (microns)	Inconel A (m^2/s)	Inconel B (N • m/g-mole)	Zircaloy A (m^2/s)	Zircaloy B (N • m/g-mole)
0	16.6127	-288100	4.6364	-252312
20	1.377 x 10^9	-504679	4.4792	-255162
45	3.489 x 10^{15}	-69392	4.321 x 10^5	-407522
100	0.8941	-253057	9.512 x 10^{-4}	-172165

Table 4-18. Value for coefficient in equation to calculate delay time due to oxide layer.

Oxide Thickness (microns)	Coefficient C1 (s)	Coefficient C2 (N • m/g-mole)
10	2.661 x 10^{-8}	2.68438 x 10^5
20	7.700 x 10^{-17}	5.24339 x 10^5
45	6.762 x 10^{-15}	4.75227 x 10^5
100	1.875 x 10^{-9}	3.29218 x 10^5
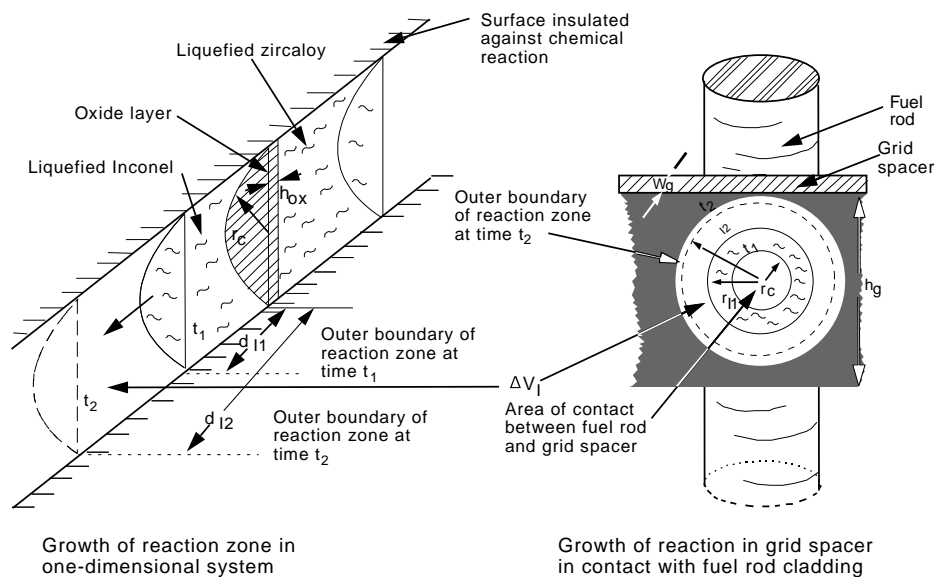
Figure 4-20. Growth of reaction zone in grid spacer.
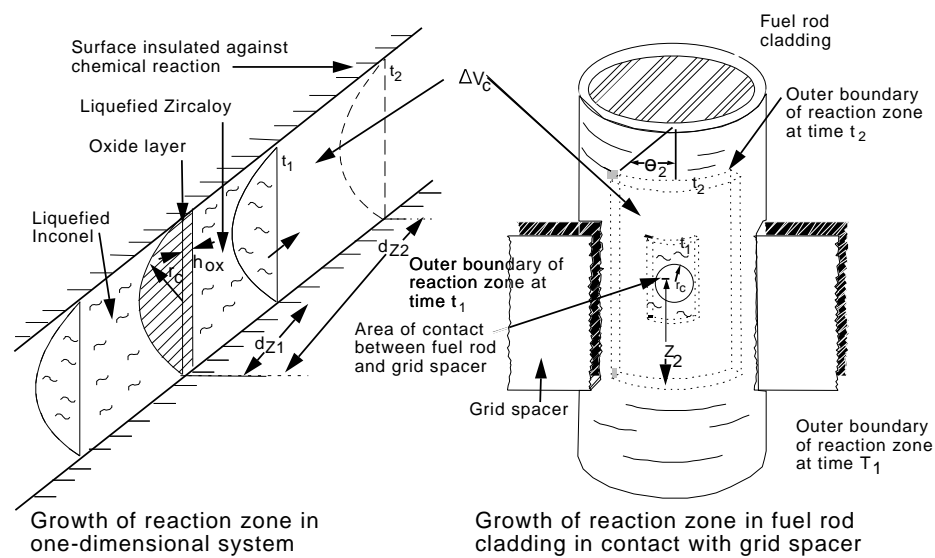
Figure 4-21. Growth of reaction zone in fuel rod cladding.

The second assumption applied to the model for growth of the reaction zone is the that rate of growth of the reaction zone is a function of the volume of the reaction zone but not the configuration of the reaction zone, provided that the area of contact between the Inconel and zircaloy is the same for each configuration. Figures 4-20 and 4-21 illustrate this determination of the growth of the reaction zones in the grid spacer panels and fuel rod cladding on the basis of the growth of the reaction zones in an equivalent one-dimensional system. The two geometrical systems are considered to be equivalent on the basis that they both have the same area of contact between the zircaloy and Inconel parts of the system. The application of this assumption allows the propagation of the reaction zone through the fuel rod cladding and grid spacer to be determined in a straight forward manner. The growth of the reaction zone in the one-dimensional system for which Equation (4-85) applies can be used to determine the growth of the reaction zone in the grid spacer and fuel rod cladding. The growth during one time step in the one-dimensional system is mapped into the actual in-core geometry to determine the growth of the reaction zone in the fuel rod cladding and grid spacer.

The equations for determining the growth of the reaction zone in the cladding and grid spacer can now be derived. The variables to be calculated are shown in Figure 4-20 and 4-21. First the growth of the reaction zone during a time step is calculated for the Inconel and zircaloy parts of a one-dimensional system. These growths are calculated by the equations

$$d_{i2} = \left[d_{i1}^2 + A_i e^{\left[\frac{-B_i}{RT}\right]} \Delta t \right]^{0.5} \tag{4-87}$$

$$d_{z2} = \left[d_{z1}^2 + A_z e^{\left[\frac{-B_z}{RT}\right]} \Delta t \right]^{0.5} \tag{4-88}$$

where

d_{i2}	=	position of leading edge of reaction zone in Inconel at end of time step (m)
d_{i1}	=	same as di_2 but for start of time step
A_i, B_i	=	coefficients for Inconel that are defined in Table 4-17
d_{z2}	=	position of leading edge of reaction zone in zircaloy at end of time step (m)
T	=	current temperature of reacting cladding and grid spacer (K)
A_z, B_z	=	coefficients for zircaloy that are defined in Table 4-17.

The increases in volume during a time step of the reaction zones in the Inconel and zircaloy are calculated by the equations

$$\Delta v_i = 0.5\pi \left(d_{i2} - d_{i1} \right) r_c^2 \tag{4-89}$$

$$\Delta v_z = 0.5\pi \left(d_{z2} - d_{z1} \right) r_c^2 \tag{4-90}$$

where

Δv_i = increase in volume of reaction zone in Inconel during time step (m^3)

Δv_z = increase in volume of reaction zone in zircaloy during time step (m^3)

r_c = radius of circle with same area as area of contact between grid spacer and fuel rod cladding (m).

The radius of the area of contact is a parameter that could be determined from experimental results. The initial value of this parameter is a function of the area of the grid spacer tab that contacts the fuel rod cladding. This area of contact may increase with time as liquefaction progresses. For the first part of this analysis the area is assumed to remain constant. A method for calculating the rate of melt progression considering a transient area of contact is presented later.

The coefficient of 0.5 in Equations (4-89) and (4-90) stems from the fact that due to symmetry only the growth of the reaction zone on one side of the line of symmetry needs to be considered.

The assumption shown in Figure 4-20 is next applied; this assumption is represented by the equation

$$\Delta v_g = \Delta v_i \tag{4-91}$$

where

Δv_g = increase in volume of the reaction zone in the grid spacer panel (m^3).

By applying Equation (4-91), the outer boundaries of the reaction zone in the grid spacer panel are then determined from the following equations:

$$w_{i2} = d_{f2} \text{ for } (w_{i2} < 0.5w_g) \tag{4-92}$$

$$r_{i2} = \left[r_{i1}^2 + \left(\frac{\pi}{4} \right) \frac{\Delta v_i}{w_g} \right]^{0.5} \tag{4-93}$$

where

w_{i2} = distance of propagation of reaction zone at time t2 into grid spacer panel in direction normal to area of contact (m)

r_{i2} = outer radius of reaction zone in grid spacer panel at time t7 (m)

r_{i1} = same as r_{i2} but for time t (m)

w_g = thickness of grid spacer panel (m).

Equation (4-92) applies until the reaction zone has propagated into the grid spacer panel a distance equal to half the thickness of the panel (0.5W9). After this time Equation (4-93) applies. Due to symmetry, the equations consider the reaction zone to be confined to half of the grid spacer panel.

Fuel Rod

The growth of the reaction zone in the fuel rod cladding is calculated in a manner similar to that used to calculate the growth in the grid spacer panel. The increase in volume of the reaction zone in the fuel rod cladding is calculated by the equation

$$\Delta v_c = \Delta v \tag{4-94}$$

where

Δv_c =   increase in volume during a time step of reaction zone in fuel rod cladding (m^3).

Until the reaction zone has penetrated the thickness of the fuel rod cladding, the outer boundary of the reaction zone is calculated by the equation

$$w_{z2} = d_{z2} \text{ for } w_{z2} < h_c \tag{4-95}$$

where

w_{z2} =   distance that reaction zone has penetrated into the cladding at time t_2 (m).

h_c =   thickness of metallic part of cladding (m).

After the reaction zone has penetrated the thickness of the cladding, the reaction zone then spreads in the circumferential and axial directions. As stated earlier, the assumption is made that the reaction zone spreads at an equal rate in the axial and circumferential directions. Referring to Figure 4-21, the outer boundaries of the reaction zone are defined by the variables Θ and z, where Θ is the measure of spread of the reaction zone in the circumferential direction (radians), and the variable z is the measure of the spread of the reaction zone in the axial direction (m). The change in volume of the reaction zone during a time step is then calculated by the equation

$$\Delta v_c = A_c(\Theta_1 + \Delta\Theta)(z_1 + \Delta z) - 0.5 A_c \Theta_1 z_1 \tag{4-96}$$

where

A_c =   cross-sectional area of one radian of metallic part of cladding (m^2)

Θ_1 =   angle defining outer boundary of propagation of reaction zone in circumferential direction at start of time step (radians)

$\Delta\Theta$ =   change during time step of angle defining propagation of reaction zone in circumferential direction (radians)

z_1 =   height of reaction zone at start of time step (m) where change in height of reaction zone during time step (m)

Δz =   change in height of reaction zone during time step (m).

The variable A_c is calculated by the equation

$$A_c = r_o^2 - (r_o - h_c)^2 \qquad (4\text{-}97)$$

where

r_o =   outer radius of metallic part of cladding (m).

Because the assumption has been made that the reaction zone is growing at equal rates in the circumferential and axial directions, the variable $\Delta\Theta$ is related to the variable Δz by the equation

$$\Delta\Theta = \frac{\Delta z}{r_o} \; . \qquad (4\text{-}98)$$

The value of Δz is then determined by substituting Equation (4-98) into Equation (4-96) and solving for Δz. The result is

$$\Delta z = 0.5 \left[\left(-b + \sqrt{b^2 - 4ac} \right) \right] \qquad (4\text{-}99)$$

The variables b and c in Equation (4-97) are calculated by the equations

$$b = r_o \left[0.5\Theta_1 + \frac{z_1}{r_o} \right] \qquad (4\text{-}100)$$

$$c = -r_o \frac{\Delta v_z}{A_c} \; . \qquad (4\text{-}101)$$

The outer boundaries of the reaction zone at the end of the time step are then determined by the equations

$$\Theta_2 = \Theta_1 + \Delta\Theta \Theta_2 = \Theta_1 + \Delta\Theta \qquad (4\text{-}102)$$

$$z_2 = z_1 + \Delta z \; . \qquad (4\text{-}103)$$

The spread of the reaction zone in the circumferential direction is complete when

$$\Theta_2 = \frac{\pi}{4} \; . \qquad (4\text{-}104)$$

After the spread of the reaction zone in the circumferential direction is complete, the reaction zone grows only in the axial direction. The rate of growth is calculated by the equation

Fuel Rod

$$z_2 = z_1 + \frac{\pi}{4} \frac{\Delta v_z}{A_c} .$$
(4-105)

The reaction between the grid spacer and cladding continues until the liquefied material slumps. The liquefied material is considered to slump when the reaction zone in the grid spacer has spread to the bottom of the grid spacer panel. This condition occurs when

$$r_{i2} = 0.5 h_g$$
(4-106)

where

h_g = height of grid spacer panel (m).

The liquefied material will slump downward into a cooler part of the reactor core and solidify.

The time between the onset of the chemical reaction and the slumping of material liquefied by the chemical reaction can be determined from Equations (4-86), (4-87), (4-89) and (4-106) for isothermal conditions. Equation (4-86) is used to calculate the time to dissolve the oxide shell and Equations (4-87), (4-89), and (4-106) are used to calculate the time to liquefy the grid spacer to the point where it slumps. Equation (4-106) defines the mass of grid spacer that must be liquefied before slumping occurs and Equations (4-86) and (4-89) define the time to liquefy this mass. This process is expressed by the equation

$$0.5 \frac{w_g}{2} (0.5 h_g)^2 = 0.5 \pi r_c^2 \left[A_i e^{\left(\frac{-B_i}{RT} \right)} (t_s - t_d) \right]^2$$
(4-107)

where

t_s = time after the beginning of the chemical reaction at which the liquefied grid spacer material slumps (s)

t_d = time for dissolution of the oxide shell (s) [calculated by Equation (4-86)].

In Equation (4-107), the left side of the equation defines the mass of grid spacer that must be liquefied before slumping occurs and the right side defines the mass of grid spacer liquefied as a function of time. The result of solving Equation (4-107) for the slumping time t_s is

$$t_s = 0.03125 \frac{w_g^2 h_g^4}{r_c^4} \left(\frac{1}{A_i e^{\left(\frac{-B_i}{RT} \right)}} \right)$$
(4-108)

Equation (4-108) shows that the slumping time is a strong function of the height of the grid spacer and the area of contact between the grid spacer and cladding.

In view of the importance of area of contact on the rate of liquefaction it is useful to develop a transient model for the area of contact. A simple transient model is one in which the area of contact is regarded as fixed until the reaction zone has completely penetrated the thickness of the grid spacer panel at the loca-

tion of the grid spacer tabs, and thereafter the area of contact increases proportional to the increase in the size of the reaction zone in the grid spacer. The model is illustrated in Figure 4-22.
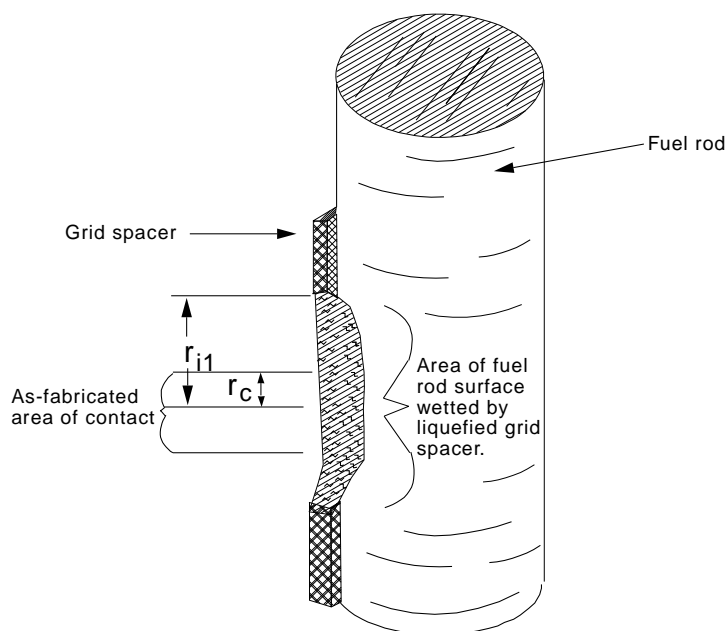
Figure 4-22. Variable area of contact between grid spacer and fuel rod cladding.

This modeling assumption is consistent with the concept of liquefied grid spacer material wetting the fuel rod surface that it faces. The model is expressed by the equations

$$r_c = r_{tab} \qquad \text{for} \qquad d_{12} < 0.5w_g \qquad\qquad (4\text{-}109)$$

$$r_c = r_{i1} \qquad \text{for} \qquad d_{i1} > 0.5w_g \qquad\qquad (4\text{-}110)$$

where

r_c	=	radius of circle with same area as area of contact between grid spacer and fuel rod cladding (m)
r_{tab}	=	area of circle with same area as area of tab on grid spacer (m)
d_{i2}, r_{i1}	=	variables defined for Equations (4-87) and (4-93), respectively.

The propagation of the reaction zone varies with location on the interface between the grid spacer and cladding. At the location of the grid spacer tab, the propagation is relatively slow because the reaction zone is already thick at that location. But the reaction zone propagates rapidly at its leading edge, because at that location the reaction zone is thin. Figure 4-23 shows the variation in the thickness of the reaction zone with respect to the location of the leading edge of liquefaction in the grid spacer. For simplicity, it is useful to have a single variable for Inconel and a single variable for zircaloy to measure the extent of propagation of the reaction in the grid spacer and cladding zones. In the case of a fixed area of contact, these

variables were d_{i2} and d_{z2} of Equation (4-87) and (4-88), respectively. In the case of a variable area of contact, a measure of the extent of growth of the reaction zone in the Inconel is provided by the variable d_{ia}, which is defined in Figure 4-23. The variable d_{ia} is the thickness of a uniform reaction zone that results in the same growth as a reaction zone of variable thickness, but the same volume as the uniform reaction zone. This variable is calculated by the equation

$$A_{w2}(d_{ia2} - d_{ia1}) = A_{w1}(d_{i2} - d_{i1}) + (A_{w2} - A_{w1})d_n \tag{4-111}$$

where

$\quad A_{w2} \quad = \quad$ area of contact between Inconel and zircaloy at end of time step (m^2)

$\quad A_{w1} \quad = \quad$ area of contact at start of time step (m^2)

$\quad d_{ia2} \quad = \quad$ value of equivalent depth of reaction zone in Inconel at end of time step (m)

$\quad d_{ia1} \quad = \quad$ same as d_{ia2}, but for start of time step (m)

$\quad d_n \quad = \quad$ depth of propagation of reaction zone at leading edge of reaction zone (m).
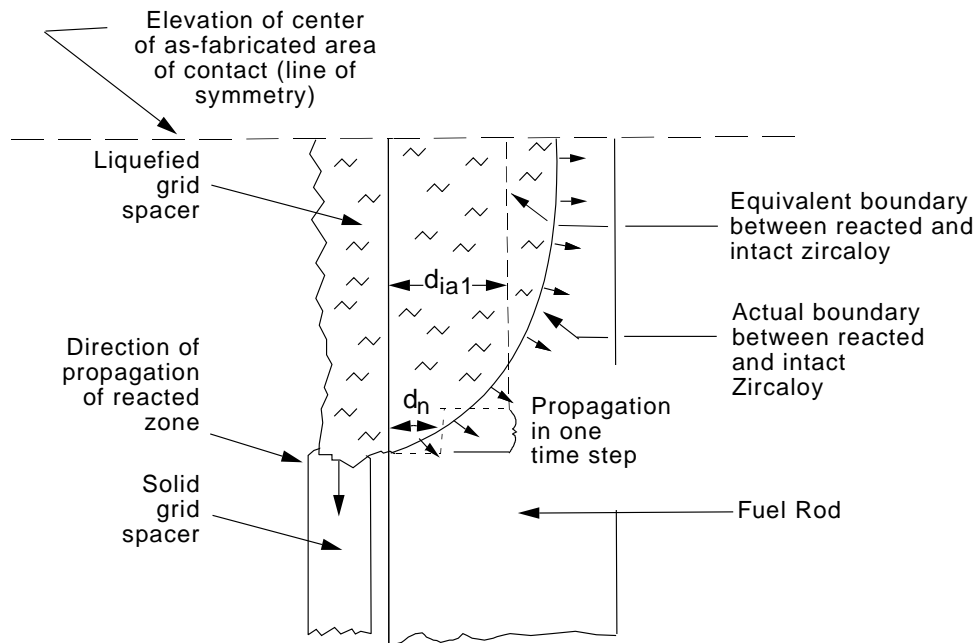
Figure 4-23. Definitions of equivalent thickness of reaction zone.

The change in location of each of the three fronts as shown in Figure 4-24 are given by the three equations

$$d_{i2} = \sqrt{d^2_{i1} + R_i} \tag{4-112}$$

$$d_{ia2} = \sqrt{d^2_{ia1} + R_i} \tag{4-113}$$

$$d_n = \sqrt{R_i} \tag{4-114}$$

where

$$R_i = A_i e^{\left[\frac{-B_i}{RT}\right]} \Delta t \tag{4-115}$$

After substituting Equations (4-112), (4-113), and (4-114) into Equation (4-111) and solving for d_{ia1}, the result is

$$d_{ia1} = 0.5 \left[\frac{R_i}{D_i} - D_i \right] \tag{4-116}$$

where

$$D_i = \frac{A_{w1}}{A_{w2}} [\sqrt{d^2_{i1} + R_i} - d_{i1}] + \frac{\sqrt{R_i}(A_{w2} - A_{w1})}{A_{w2}} \tag{4-117}$$

The calculation of the equivalent depth of the reaction zone in the zircaloy is parallel to that for the equivalent depth in Inconel. The result is

$$d_{za1} = 0.5 \left[\frac{R_z}{D_z} - D_z \right] \tag{4-118}$$

where

$$D_z = \frac{A_{w1}}{A_{w2}} [\sqrt{d^2_{z1} + R_z} - d_{z1}] + \frac{\sqrt{R_z}(A_{w2} - A_{w1})}{A_{w2}} \tag{4-119}$$

$$R_z = A_z e^{\left[\frac{-B_z}{RT}\right]} \Delta t \tag{4-120}$$

The calculation of the melt progression in the grid spacer and fuel rod cladding proceeds basically as shown for the case of a constant area between the grid spacer and cladding. The following differences are made. In Equations (4-87) through (4-90) d_{ia1} and d_{za1} are substituted for d_{i1} and d_{z1}, respectively. In equations (4-89), (4-90), (4-100), and (4-101) the variable r_c as calculated in Equation (4-110) is applied. The new positions of the melt fronts in the Inconel and zircaloy for the one-dimensional system are

$$d_{i2} = d_{i1} + d'_{i2} - d_{ia1} \tag{4-121}$$

$$d_{z2} = d_{z1} + d'_{z2} - d_{za1} \tag{4-122}$$

where

d'_{i2} =   location of melt front calculated using d_{ia1} instead of d_{i2} (m)

d'_{z2} =   location of melt front calculated using d_{za1} instead of d_{21} (m).
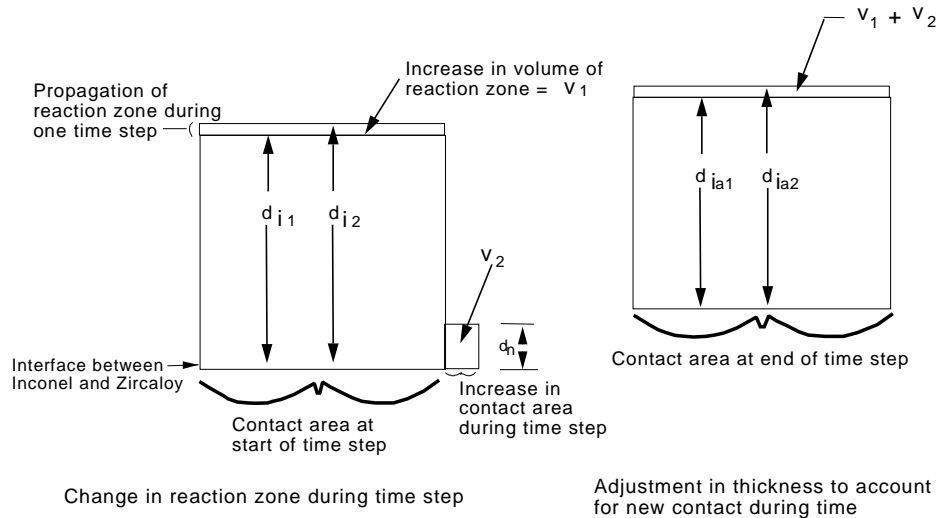
Figure 4-24. Adjustment in thickness of equivalent reaction zone to account for new contact during time step.

4.8.3 Equilibrium Temperature Model for Relocated Material

The lower and cooler part of a reactor core can heat up in response to the chemical reaction between an Inconel grid spacer and fuel rod cladding. This heatup is due to the transfer of thermal energy from the hotter to the cooler part of the core by the slumping of reacted and liquefied material to a grid spacer in the lower part of the core. Some of the slumping material may contact fuel rods as it slumps and thus lose thermal energy as it slumps. The rest of the slumping material will fall freely until it encounters the next grid spacer below the grid spacer at which the reaction took place. For SCDAP/RELAP5/MOD3.1, all of the material is considered to fall freely. A method is described for calculating the heatup of the region in which the slumping material encounters a grid spacer.

A jump in temperature occurs at the location of a grid spacer onto which material falls after slumping from a location that is at a hotter temperature. An equilibrium temperature model is used to calculate the magnitude of the jump in temperature. The equilibrium temperature is calculated in two steps: (1) Calculate the equilibrium temperature of a system consisting of the slumping material and the grid spacer that supports it, including material trapped earlier, and (2) calculate the equilibrium temperature of a system consisting of the grid spacer and material it supports (the combined system considered in Step 1), and the axial node in the two-dimensional (radial-axial) fuel rod heat conduction model that overlays the grid spacer at which the slumping material solidified. The model is illustrated in Figure 4-25. The equilibrium temperature from Step 2 is imposed as the temperature of the indicated axial node for the start of the next time step. The fuel rod heat conduction model then calculates the transient transport of heat from the slumped material into the portions of the fuel rod above and below the impacted grid spacer. The tempera-

ture at the location of the impacted grid spacer changes with time as indicated in Figure 4-26.

The temperature distribution in a reactor core can be affected in several ways by the relocation of fuel rod cladding that reacted with an Inconel grid spacer. First, the transfer of thermal energy from a location higher in the core to a location lower in the core can accelerate the oxidation in the lower part of the core and thus accelerate the heatup of the lower part of the core. Second, relocated cladding can block the flow of coolant and thus cause an increase in heatup of the portion of the reactor core above the location of the blockage. Third, slumping of the reacted cladding removes metallic material that is oxidizing at a relatively rapid rate and transfers the material to where it may oxidize at a slower rate due to a cooler temperature and more compact geometry.
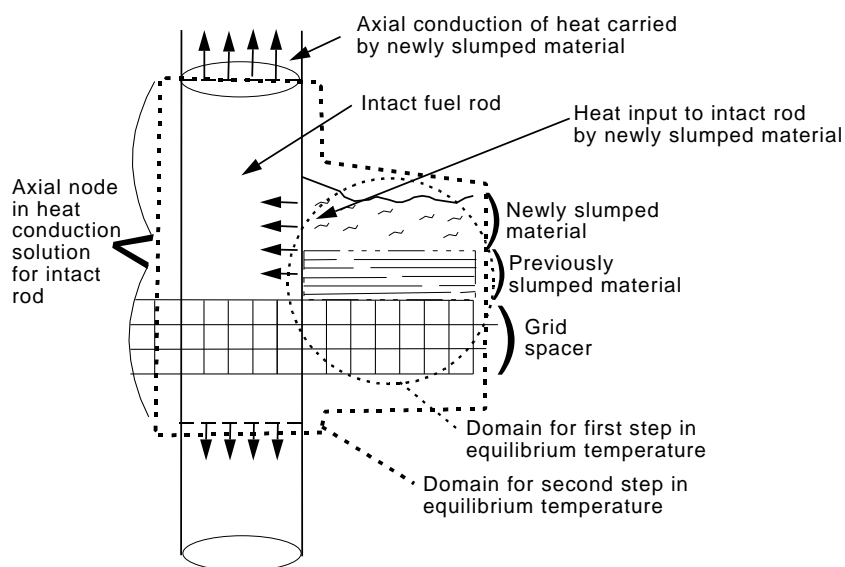
Figure 4-25. Location of materials considered to instantaneously reach equilibrium temperature following creation of newly slumped material.
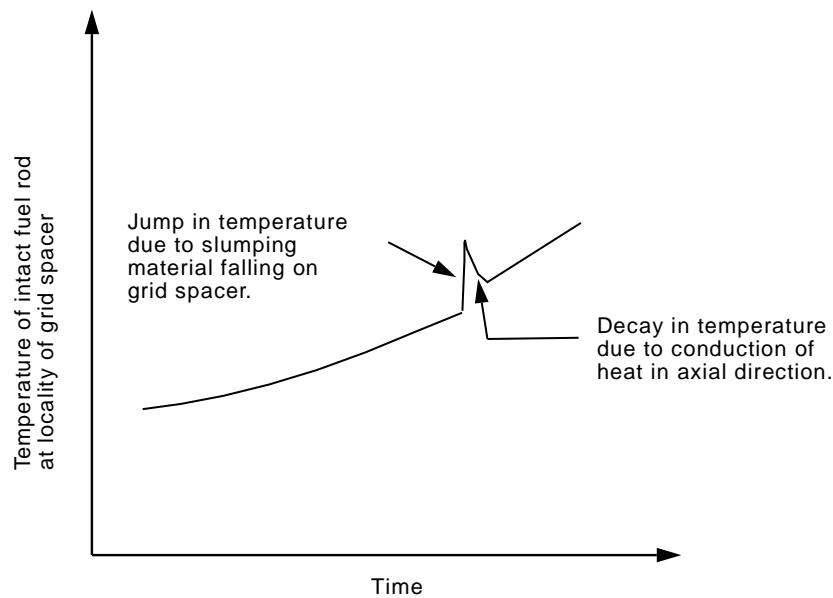
Figure 4-26. Temperature response of fuel rod following contact with hot material that slumped from above.

4.9   Oxidation of Porous Debris

Oxidation will occur in hot porous debris that contains fragments of metallic material, such as zirconium from fuel rod cladding. Fuel rods can disintegrate into porous debris after they are partially oxidized so as to become embrittled and are then rapidly cooled. If the resulting bed of porous debris become deficient in cooling, the metallic particles in the bed will oxidize with the result of an increase in the rate of heatup of the debris and the production of hydrogen.

4.9.1   Model Framework

The model for oxidation of porous debris is implemented into the model that calculates the change in temperature of porous debris during a time step. This model is programmed in the subroutine HEATDB and represents, as a lumped mass, the porous debris that exists at an axial node of a fuel bundle or any group of identical fuel rods. The content of the HEATDB model is shown in Figure 4-27. Cladding and fuel particles are assumed to be mixed together. The size and composition of the particles are defined by the fuel rod fragmentation model, which is programmed in subroutine RUBTRN. If the fuel rods have been heated to a temperature greater than the melting temperature of the cladding, then the cladding dissolves fuel. If the fuel rods later cool and fragment, the particles of cladding are composed of a mixture of Zr-U-O. The conduction of heat from a particle to its neighboring particles is not represented; all of the particles in the lumped mass are assumed to be at the same temperature, which is considered to be uniform within each particle. The temperature change of the lumped mass is calculated taking into account the decay heat in it and the rate of heat transfer between it and the fluid flowing through it. The model calculates the oxidation of the metallic particles within the porous debris and the effect that oxidation has on the thermal response of the porous debris.
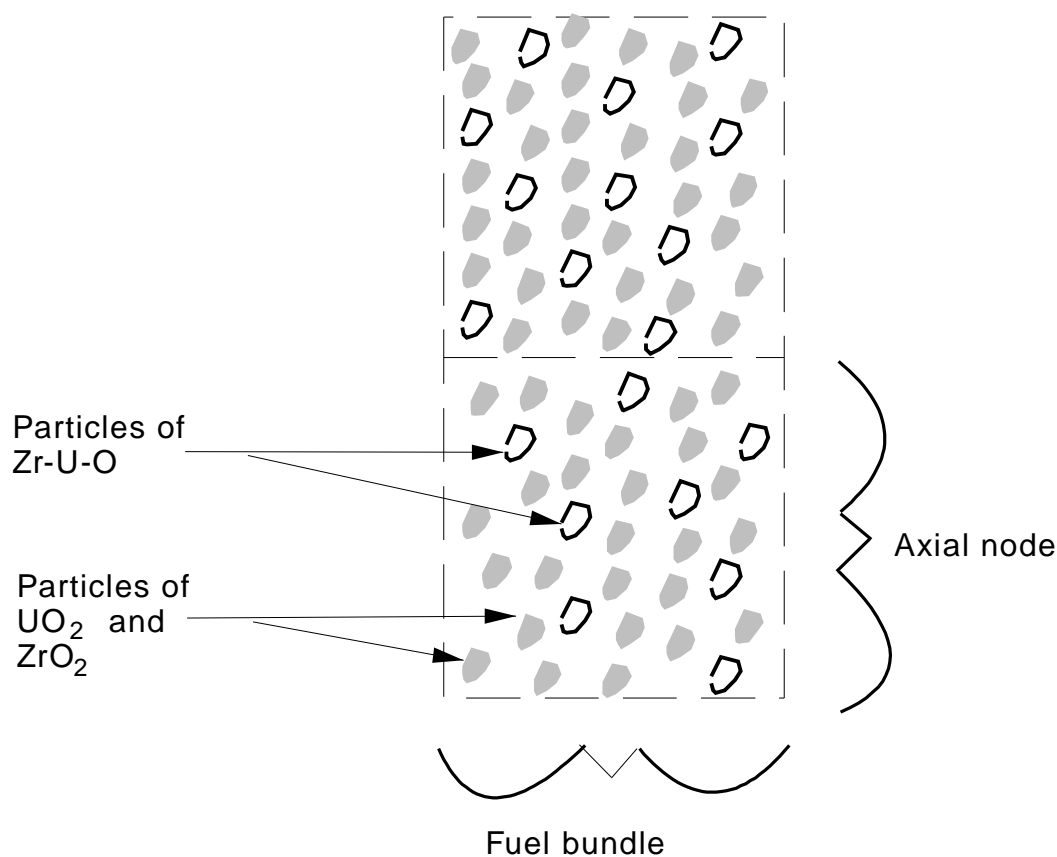
Figure 4-27. Content of model for oxidation of porous debris.

4.9.2 Basic Concepts and Assumptions

The same concepts for oxidation of a unit surface area of cohesive debris (presented in Section 3.3) will be applied for the oxidation of a unit surface area particles in porous debris bed. The model will consider the oxidation of particles that are composed of cladding material and particles that are composed only of fuel. The heat generated per unit surface area of debris particles will be calculated by Equation 2-37. The model for calculating the temperature of the porous debris (HEATB model) requires the volumetric heat generation in the porous debris. The volumetric heat generation due to oxidation is calculated by the equation

$$P_v = A_{ms}Q_m + A_{Us}Q_U \qquad (4\text{-}123)$$

where

P_v	=	volumetric heat generation due to oxidation in porous debris (W/m^3)
A_{ms}	=	surface area of debris particles that are composed of Zr or Zr-U-O (m^2/m^3)

Q_{mv} =   heat generated at surface of particles composed of Zr or Zr-O-U due to oxidation. This variable is calculated by Equation (2-37) with f equal to the mass fraction of UO_2 in the Zr-U-O particles (W/m^2)

A_{Us} =   surface area of debris particles that are composed of UO_2(m^2/m^3)

Q_U =   heat generated at surface of particles that are composed of UO_2. This variable is calculated by Equation (2-37) with f equal to 1 (W/m^2).

A representation of the geometry of porous debris is required in order to model the oxidation of porous debris. The particle size and shape of each material constituent are required. Since a model is not available that calculates the size and shape of the debris resulting from disintegration, an *ad hoc* assumption is applied of the size and shape of a disintegrated fuel rod. The assumption that is applied to define the configuration of a disintegrated fuel rods is shown in Figure 4-28. The left side of Figure 4-28 shows the configuration of the rod before disintegration, and the right side of Figure 4-28 shows the configuration of the rod after disintegration. When the fuel rod is still intact, it consists of three material regions: cladding oxide, metallic cladding with dissolved fuel, and fuel. Upon disintegration, each of the material regions is assumed to separate from each other and break up into particles that are cubic in shape. In the outer two regions, the width of one face of the particle is assumed to equal the thickness of the annulus of the material region just before disintegration. This assumption on particle size is reasonable in view of the small particles observed in the portion of the TMI-2 core that was quenched. The average particle size of the debris in this portion of the core was 0.87 mm[56], which is of the same magnitude of size as the as-fabricated cladding thickness, which was 0.67 mm.
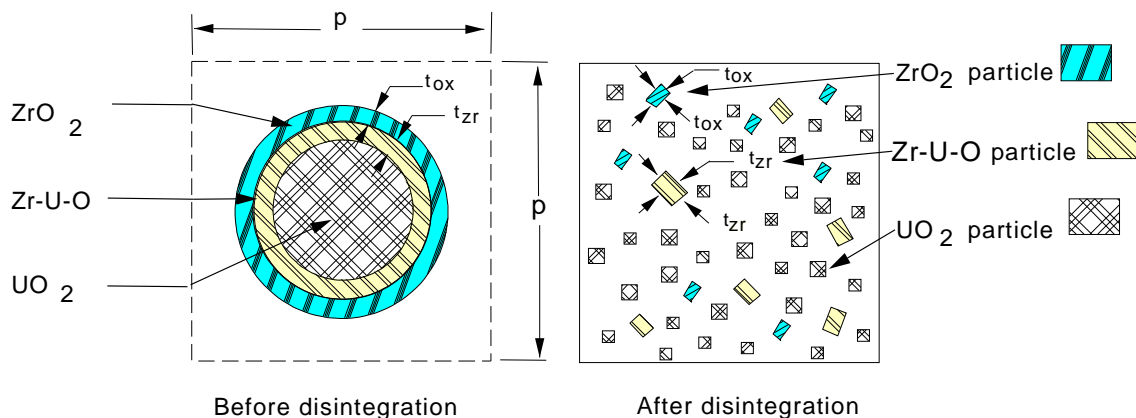
M167-BDR-0293-014

Figure 4-28. Configuration of disintegrated fuel rod.

The surface area of the zircaloy and fuel particles per unit volume of debris is required in order to calculate the volumetric rate of heat generation due to oxidation. The surface area is calculated in two steps. First, the surface area per particle is calculated; second, the number of particles per unit volume of

porous debris is calculated. The surface area per metallic particle (particles composed of Zr or Zr-U-O) is calculated by the equation

$$A_p = 6t_{zr}^2 \qquad\qquad (4\text{-}124)$$

where

      t_{Zr} =   thickness of annular region of Zr-U-O (cladding and dissolved fuel)(m^2)

      A_p =   surface area of one particle of metallic material (m^2).

    The volume of one particle is calculated by the equation

$$V_p = t_{Zr}^3 \qquad\qquad (4\text{-}125)$$

where V_p is the volume of one particle (m^3). The number of particles per unit height of one fuel rod is calculated by the equation

$$n_r = \frac{\pi (r_o^2 - r_i^2)}{V_p}$$

where

      n_r =   number of particles per unit height of one fuel rod

      r_o =   outer radius of annular region of Zr-U-O(m)

      r_i =   inner radius of annular region of Zr-U-O(m)

      $(r_o\text{-}r_i)$ = t_{Zr}=thickness of annular region of Zr-U-O(m).

    The core volume per unit height of fuel rod is given by the equation

$$V_c = p^2 \qquad\qquad (4\text{-}126)$$

where

      V_c =   volume of core per unit height of one fuel rod (m3/m)

      p =   pitch of fuel rods (m).

    The number of particles per unit of core volume occupied by fuel rods is then given by the equation

$$n_p = \frac{n_r}{V_c} \qquad\qquad (4\text{-}127)$$

where n_p is the number of particles per unit volume of core occupied by fuel rods (particles/m3).

A compaction or expansion of materials may take place when fuel rods disintegrate, causing the number of particles per unit volume of debris to be different than the number of particles per unit of core volume occupied by fuel rods. The ratio of these two particle densities is given by the equation

$$\gamma = \frac{\varepsilon_r}{\varepsilon_d} \tag{4-128}$$

where

γ	=	ratio of particle density at porosity of intact core to particle density at porosity of disintegrated core
ε_r	=	porosity of core with intact fuel rods
ε_d	=	porosity of porous debris.

The porosity of porous debris is assumed to equal the average porosity of the upper debris bed in the postaccident TMI-2 reactor core, which was 0.54.[56] The porosity of a core with intact fuel rods is given by the equation

$$\varepsilon_r = 1 - \frac{\pi r_c^2}{P^2} \tag{4-129}$$

where r_c is the outer radius of as-fabricated fuel rods (m). Typical values of r_c and p are 0. 5461×10^{-2} m and 1.4427×10^{-2} m, respectively. So, the typical value of ε_r is 0.55. This value is similar to the porosity measured for the upper debris bed in the TMI-2 core. The similar values indicate that there is no significant compaction or expansion of that portion of a reactor core in which the fuel rods disintegrate. Thus, the parameter γ is set equal to 1.

The surface area of metallic particles per unit volume of debris is then given by the equation

$$A_{ms} = n_p A_p = \frac{6\pi (r_o + r_i)}{p^2} \tag{4-130}$$

where A_{ms} is the surface area of metallic debris per unit volume of debris (m^2/m^3). This variable is applied in Equation (4-123).

A perspective of the amount of surface area of Zr particles in a disintegrated core can be obtained by comparing this surface area to that of the surface area of Zr in an intact core. In an intact core with single-sided oxidation, the surface of Zr exposed to steam per unit volume of core is approximately

$$A_c = \frac{\pi (r_o + r_i)}{p^2} \tag{4-131}$$

where A_c is the surface area of metallic material exposed to coolant per unit volume of core (m^2/m^3). By taking the ratios of A_{ms} to A_c, it is seen that when fuel rods disintegrate, the surface area exposed to steam increases by a factor of six over intact rods with single-sided oxidation.

The surface of fuel particles per unit volume of porous debris [variable A_s in Equation (4-123)] is calculated in a manner similar to that for metallic particles. Fuel particles are assumed to have a particle size of 0.87 mm, which corresponds with the average particle size of debris in the upper debris bed of the postaccident TMI-2 core.[56]

Some debris models, such as those for flow resistance, require an effective particle size for a debris bed with a range of particle sizes. The three types of material in the porous debris--namely, ZrO_2, Zr-U-O (metallic cladding and dissolved UO_2) and UO_2--each have a different particle size. The Fair-Hatch formula[57] is applied to calculate the effective particle diameter. This formula is

$$d_e = f_s \left(\sum_{i=1}^{3} \frac{f_i}{d_i} \right)^{-1}$$

(4-132)

where

(4-133)

d_e = effective diameter of particles (m)

f_s = shape factor

f_i = volume fraction of material type i. For i = 1, the material is zircaloy; for i = 2, the material is Zr-U-O; and for i = 3, the material is UO_2

d_i = size of particles in material type i (m).

The shape factor f_s is 0.78 for rough particles and 1.0 for spheres; the shape factor for rough particles will be applied. The value of d_1 is equal to t_{ox} (the thickness of the sh ell of ZrO_2).. The value of d_2 is equal to $t_{Z r}$ (the thickness of the annulus of Zr-U-O). The value of d_3 is 0.87 mm, which is the average size of the debris particles in the upper debris bed in the postaccident TMI-2 reactor core.

4.9.3   Model Implementation

The model for oxidation of debris is implemented into the HEATDB model, which calculates the thermal response of the porous debris. The HEATDB model calculates the volumetric heat generation in the debris due to decay of fission products in the debris, adds this heat generation to the heat generation due to fission product decay, and then applies the sum of these two sources of heat in calculating the thermal response of the debris.

Given a unit surface area of debris, the debris oxidation model calculates the weight gain in oxygen and the heat generation in the debris as a function of the debris temperature and its composition and as a function of the conditions of the fluid in contact with the debris. The rate of oxidation is limited to the maximum possible rate of oxygen transfer from the bulk coolant to the surface of the debris particles. This mass transfer limit is calculated by Equation 3-10 of Section 3.1 of this report. Since the debris at an axial node is represented as a lumped mass, the heat generation due to oxidation of metallic particles is assumed to be uniformly distributed within the axial node. This heat generation is added to the uniformly distributed value of the heat generation from fission product decay to obtain the overall rate of heat generation in the porous debris. The hydrogen produced by oxidation in the porous debris is added to the source term for noncondensable gases in the RELAP5 part of the code.

Fuel Rod

5. MODELS FOR OTHER CORE COMPONENTS

5.1 Ag-In-Cd Control Rod Models

Control rod temperatures are computed using the heat conduction model described in Section 2.1 on page 1. User-specified nuclear heating, chemical heating due to oxidation of the zircaloy guide tube, and convective and radiative heat transfer from the coolant and adjacent fuel rods are considered.

In order to model non-standard control rod configurations, the ability to specify material by indices has been added. In order to maintain backward compatibility, the default material configuration remains as:

- Control rod absorber material (Ag/In/Cd in PWR's),

- Stainless steel,

- Zircaloy.

5.1.1 Control Rod Material Interaction

A parabolic kinetics model is applied to represent the chemical reaction that takes place between the stainless steel cladding of a pressurized water reactor (PWR) control rod and the Zr guide tube adjacent to it. This chemical reaction causes the cladding and guide tube to liquefy at temperatures below their respective stand-alone melting temperatures. The model calculates the growth of a zone of liquefied material due to the chemical reaction between the iron in the stainless steel cladding of the absorber material and the zirconium in the control rod guide tube. The situation in which the model is applied is shown in Figure 5-1. The stainless steel cladding of the absorber material is assumed to be in contact with the guide tube that surrounds it. The chemical reaction that takes place between the stainless steel and the zirconium is a strong function of temperature. Since the temperature of the control rod varies in the axial direction, the radial extent of the reaction zone also varies in the axial direction. The objective of the model is to calculate, as a function of time, the inner and outer radii of the reaction zone. If the outer radius of the reaction zone reaches the outer radius of the guide tube, then a breach is formed; and liquefied material will slump through the breach.

The outer radius of the reaction zone will be calculated as a function of time by the equation[58]

$$r_{soN2} = \left[r_{soN1}^2 + A\,exp\left(-\frac{B}{RT}\right) \Delta t \right]^{0.5} \tag{5-1}$$

where

r_{soN2} =   outer radius of reaction zone at end of time step for axial node N (m)

r_{soN1} =   outer radius of reaction zone at start of time step (m)

A,B   =   coefficients that are a function of temperature and are defined as 2.78e-15 m^2/s and -642864, respectively

R   =   universal gas constant (8.314 Pa•m^3/(g-mole•K)

T =   temperature of reacting materials (K)

Δ t =   time step size (s).

  The equation for calculating the inner radius of the reaction zone, namely variable r_{sin} of Figure 5-1, is the same as that used to calculate the outer radius, except that the coefficients A and B are defined as 1.08e-15 m ^{2}/s and -688790 (unitless).
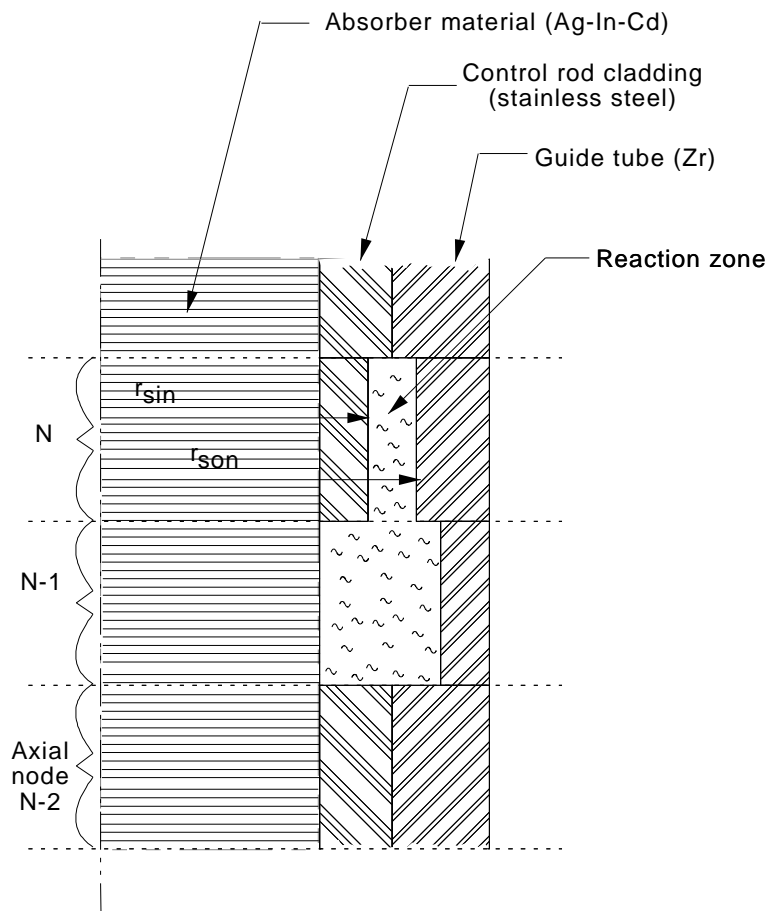
M167-BDR-1292-004

Figure 5-1. Chemical reaction between control rod cladding and guide tube.

  The binary alloy phase diagram of the Fe-Zr system is used to limit the rate of growth of the reaction zone to that which keeps the material in the reaction zone liquefied. The phase diagram of the Fe-Zr system is shown in Figure 5-2. The symbol L in the top part of the diagram designates the phase that is liquid. The curve below L defines the boundary between a liquefied and solidified mixture as a function of the temperature of the mixture and the fraction of Fe in the mixture. The curve indicates that a liquefied reaction zone begins when the temperature of the control rod cladding and guide tube exceeds 1201 K. If the Fe content in the reacted zone stays at 24 at. % Fe, then the reaction zone continues to grow at the rate predicted by the kinetics equations. If, on the other hand, the fraction of Fe in the zone increased to 40 at.

% Fe, then the reaction zone in the control rod cladding could not continue until the temperature increased to 1740 K or until enough Zr had liquefied that the fraction of Fe in the mixture was reduced to 24 at. %.
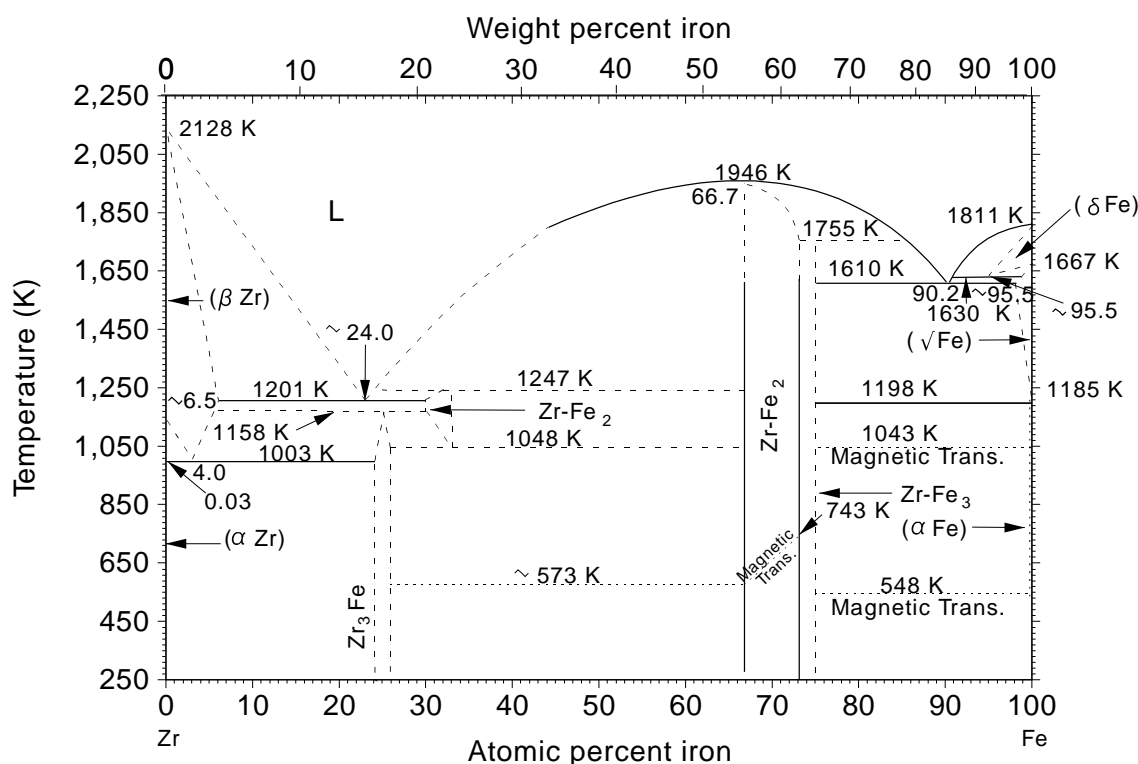
Figure 5-2. Binary alloy phase diagram of the system Fe-Zr.

5.2   BWR B₄C Control Blade and Channel Box Component Model

The BWR blade/box component model was developed at Oak Ridge National Laboratory (ORNL).[66] The model is designed to meet two general design requirements. First, the component must be able to represent all BWR geometries of interest, including full-size BWR cores and experimental facilities. Figure 5-3 shows the basic geometry considered. Second, the component must contain sufficient detail to account for all important phenomena, yet use computer resources efficiently. This section provides brief descriptions of the models used to represent the control blade and channel box.

5.2.1   Nodal Geometry

The BWR blade/box component is based on the nodal configuration shown in Figure 5-4. At each axial location, three radial temperature nodes are used for the control blade and two temperature nodes for the channel box. The actual control blade configuration of small rodlets inside a stainless steel-blade sheath is converted into an equivalent slab geometry. The solid structures of the component interact with two RELAP5 hydrodynamic volumes: one for the interstitial region and the other for the fuel bundle region. The gap between the blade sheath and rodlets is modeled. This gap communicates with the intersti-

tial coolant volume through a series of holes in the blade sheath (refer to Figure 5-3). The gap results in two additional surfaces for stainless steel oxidation and also imposes an additional thermal resistance between the blade sheath and rodlets.
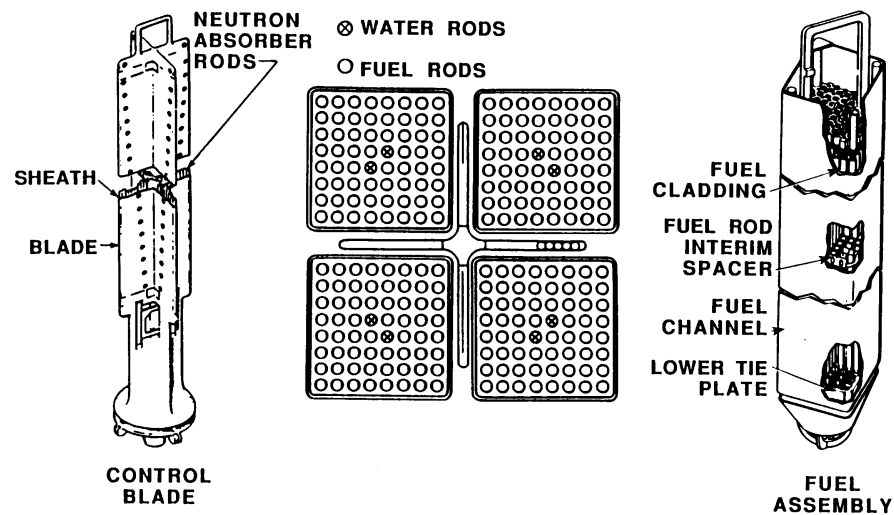
Figure 5-3. A typical BWR control blade and fuel assembly.

The thermal calculations for the BWR blade/box component take advantage of symmetry. The three control blade temperature nodes actually represent only half of a control blade; the other half is identical. The dashed line surrounding the component in Figure 5-4 represents an adiabatic surface. This adiabatic surface is shown as a triangular-shaped symmetrical region on the sketch of a typical BWR core in Figure 5-5. Figure 5-5 also highlights the need for modeling the channel box with two segments. One segment is adjacent to the control blade and the other is adjacent to another channel box.
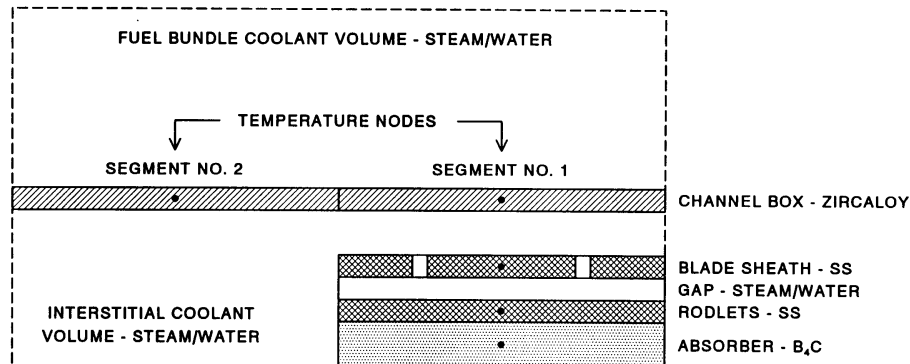
Figure 5-4. BWR control blade and channel box component with five temperature nodes and equivalent slab geometry (radial cross-sectional view).
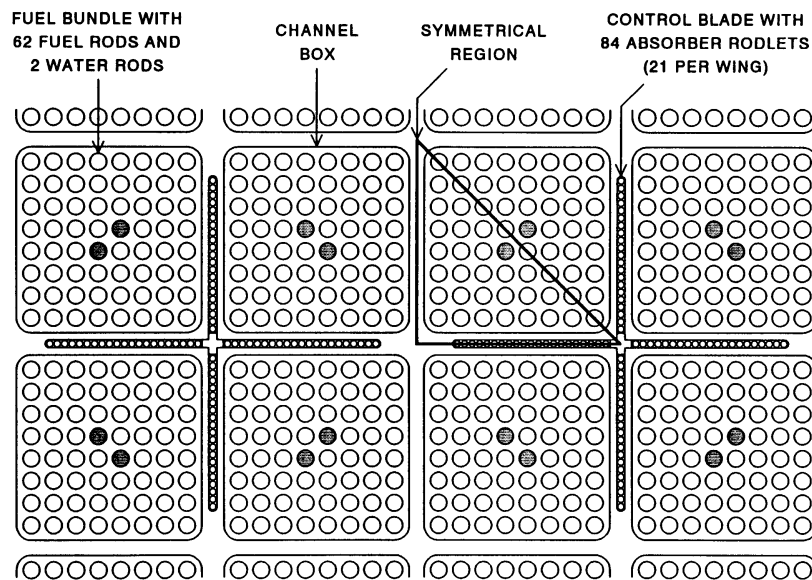
Figure 5-5. Arrangement of fuel assemblies and control blade in typical BWR core.

5.2.2 Energy/Conduction Equation

A finite difference formulation is used to model the thermal responses of the control blade and channel box structures. Using the nomenclature in Figure 5-6, the energy/conduction equation (radial direction) for a channel box node is:

$$AX(TBOX_{new} - TBOX) = AO(TBKO - TBOX_{new}) + AI(TBKI - TBOX_{new}) + QBOX. \qquad (5-2)$$

All quantities in this equation are evaluated at the previous time step except for the new channel box temperature, $TBOX_{new}$. The equation is solved implicitly for $TBOX_{new}$.

For the control blade, similar equations are derived for each of the three radial nodes. The three equations are solved implicitly for the new temperatures $TCB1_{new}$, $TCB2_{new}$, and $TCB3_{new}$.

As a control blade melts and relocates, some nodes become blocked and others disappear. The BWR blade/box model includes logic to use different energy/conduction equations that depend upon the local situation, including recognition of these blocked/missing nodes. For example, at an axial elevation where there is a blockage in the interstitial volume between the control blade and channel box, there is a radial conduction path through five nodes. The temperatures of these five nodes are solved implicitly.

Axial conduction is included in the BWR blade/box model, but is calculated differently than radial conduction. Axial conduction heat transfer rates are calculated explicitly using previous time step information. These axial conduction rates are then added to the net energy transfer rates (QBOX, QCB1, QCB2, or QCB3) in the energy/conduction equations.
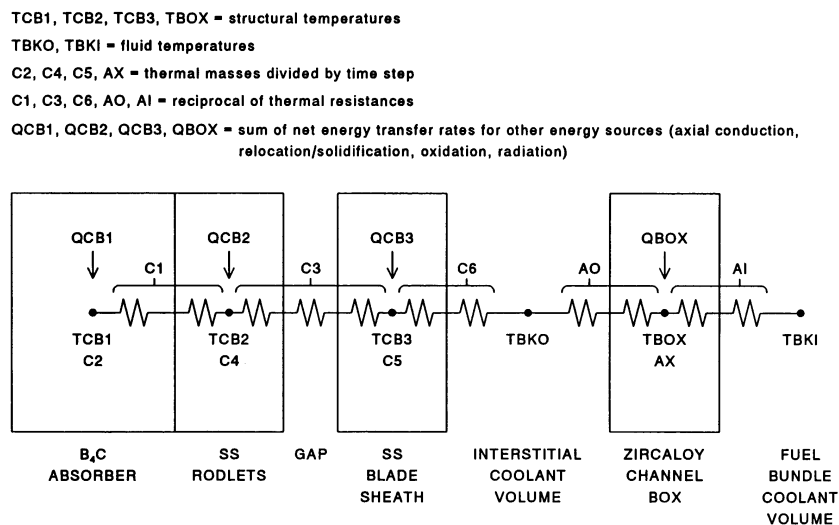
Figure 5-6. Nomenclature used for solution of energy/conduction equations in radial direction.

5.2.3   Melting and Material Interaction Models

An approximate solution method is used to solve the melting terms in the energy equations. At the end of each time step, the new temperatures calculated from the energy/conduction equations (see Section 5.2.2) are compared with their associated melting temperatures. If a nodal temperature is greater than its melting temperature and the node also contains solid material, then the nodal temperature is adjusted downward to equal its melting temperature and the associated sensible heat is used to melt an appropriate amount of the solid material. This temperature adjustment is not made if the node does not contain any

solid material (i.e., if it contains only liquid material).

An approximate method is used to simulate the liquefaction of B_4C/stainless steel and stainless steel/ zircaloy eutectics. Material compositions are tracked in each solid node. When B_4C and stainless steel, or stainless steel and zircaloy, are present in a node, these material pairs are allowed to react, using Hofmann's reaction kinetics.[59,67] After a eutectic interaction has occurred in a node, a failure (liquefaction) temperature is used in the melting calculations rather than the melting temperature of the pure material. The code does not contain correlations for these failure (liquefaction) temperatures; they must be specified by the code user. Based on ORNL analyses of the DF-4 and CORA experiments, the recommended failure (liquefaction) temperature for stainless steel that has reacted with B_4C is 1,505 K. The recommended failure (liquefaction) temperature for zircaloy that has reacted with stainless steel is 1,523 K.

5.2.4   Relocation/Solidification Models

The relocation of molten material is assumed to be controlled by solidification rates. The effects of liquid viscosity and momentum are assumed to be negligible. As molten material relocates downward over an underlying solid structure, it will solidify and transfer heat to the underlying solid. In the BWR blade/ box model, molten material is allowed to relocate downward until it either solidifies or moves past the bottom of the defined core. Solidification heat transfer rates at each axial node are calculated explicitly using previous time step information. These solidification rates are then added to the net energy transfer rates (QBOX, QCB1, QCB2, or QCB3) in the energy/conduction equations (see Section 5.2.2).

The code does not contain correlations for heat transfer between molten material and the underlying solid. The code user must specify heat transfer coefficients for molten stainless steel and for molten zircaloy. Based on ORNL analyses of the DF-4 and CORA experiments, the recommended heat transfer coefficients for both stainless steel and zircaloy are 3,400 $W/(m^2 \cdot K)$.

The relocation logic in the BWR blade/box model allows for horizontal movement of molten material when a blockage inhibits downward movement. For example, if there is a blockage in the interstitial volume between the control blade and channel box, and the adjoining channel box node has failed, then molten control blade material is allowed to relocate through the original location of the channel box wall and into the fuel-bundle region. If the adjoining channel box node has not failed, and the region beyond the tip of the control blade remains open, then molten material is allowed to relocate laterally from segment No. 1 to segment No. 2. If both horizontal directions are blocked, then molten material is allowed to pool up on top of the interstitial blockage.

5.2.5   Oxidation Models

The oxidation of stainless steel, zircaloy, and B_4C is included in the BWR blade/box model. Oxidation heat generation rates at each axial node are calculated explicitly using previous time step information. These oxidation rates are then added to the net energy transfer rates (QBOX, QCB1, QCB2, or QCB3) in the energy/conduction equations (see Section 5.2.2). Hydrogen production rates are also calculated at each axial node. The correlations provided in the model are described below.

__5.2.5.1   Stainless Steel.__ Stainless steel at high temperatures (close to its melting point) reacts vigorously with steam to yield metal oxides and large quantities of hydrogen. The reaction is similar to that

of Zr/H_2O, but the reaction energy is considerably less than that of Zr/H_2O per unit mass of metal reacted. In addition to iron, the oxidation of Cr and Ni is considered because these elements make up 18% and 8%, respectively, of stainless steel. Note that the oxidation of Cr is the major contributor to the total reaction energy.

Baker's criteria[68] is used for determining steam rich, hydrogen excess, or steam lean conditions. The oxidation correlations used for these three conditions are described below. For a situation where the reaction rate is controlled by gaseous diffusion, the Baker/Just approach[69] is used.

For steam rich conditions, White's kinetic correlation[68,70] is used. The essential chemical reactions for these conditions are:

$$2Cr + 3H_2O \rightarrow Cr_2O_3 + 3H_2 \tag{5-3}$$

$$3Fe + 4H_2O \rightarrow Fe_3O_4 + 4H_2 \tag{5-4}$$

$$Ni + H_2O \rightarrow NiO + H_2 \tag{5-5}$$

$$3FeO + H_2O \rightarrow Fe_3O_4 + H_2 \,. \tag{5-6}$$
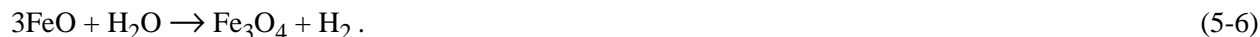
For hydrogen excess conditions, Baker's correlation[68] is used. Ni does not react under these conditions. The oxidation of steel will form a "spinal" compound:

$$2Cr + Fe + 4H_2O \rightarrow FeO*Cr_2O_3 + 4H_2 \,. \tag{5-7}$$

For steam lean conditions, a mean of the above steam rich and hydrogen excess correlations is used. Ni does not react under these conditions. The essential chemical reactions are:

$$2Cr + 3H_2O \rightarrow Cr_2O_3 + 3H_2 \tag{5-8}$$

$$Fe + H_2O \rightarrow FeO + H_2 \,. \tag{5-9}$$

5.2.5.2   Zircaloy. The following parameters are calculated: (a) ZrO_2 layer growth, (b) alpha-Zr-oxygen saturated layer growth, and (c) total Zircaloy weight gain. No reaction is considered for temperatures <923 K. For temperatures >923 K, three temperature regions are considered:

- 923 -1,173 K, oxide layer approximately obeys cubic kinetics

- 1,323 -1,853 K, oxide layer follows parabolic kinetics

- >1,853 K, reaction accelerates because of changes in oxide microstructure.

The region between 1,173-1,323 K is approximated by logarithmic interpolation between the low and middle regions. At low temperatures (923-1,173 K), the Spnigfields No. 2[71] oxidation correlation is

used. At medium temperatures (1,323-1,853 K), the Cathcart and Pawel[74] oxidation correlation is used. At high temperatures (>1,853 K), the Urbanic/Heidrick oxidation correlation[73] is used.

5.2.5.3 Boron Carbide. B_4C oxidation/reduction predictions are obtained from the advanced $B_4C/H_2/H_2O$ chemistry package, which performs a chemical equilibrium calculation using a free energy minimization solution method. The package was developed by E. C. Beahm of ORNL's Chemical Technology Division. It is based on the SOLGASMIX code.[75] Beahm's package was modified so that it could be interfaced with the BWR blade/box model. The equilibrium calculation includes the following chemical species: H_2, $H_3B_3O_6$, O_2, H_2O, HBO_2, B_4C (l), CO, BH_3, B_2O_3 (l,s), CH_4, B_2H_6, B, CO_2, BOH, C, B_2O_3 (g), O, Ar.

5.2.6 Radiation Models

Radiation calculations on the fuel-bundle side of the channel box are performed externally by the SCDAP radiation model. The two segments of the channel box are treated independently within the SCDAP radiation model. Radiation calculations on the interstitial side of the channel box are performed internally by the BWR blade/box model. Radiation is modeled in the radial direction between the control blade and the two channel box segments.

When the local fluid void fraction is greater than a user-specified value, radiation heat transfer rates at each axial node are calculated explicitly using previous time step information. These radiation rates are then added to the net energy transfer rates (QBOX, QCB1, QCB2, or QCB3) in the energy/conduction equations (see Section 5.2.2).

5.2.7 Hydrodynamic Models

All hydrodynamic parameters used in the BWR blade/box model are obtained from the RELAP5 database. These hydrodynamic parameters are shown in Figure 5-7 along with the other interface information that is exchanged with SCDAP/RELAP5. The steam, hydrogen, and inert (primarily argon) mass flow rates, along with the fluid pressures, are used in the oxidation models to calculate the partial pressures of steam and hydrogen. The fluid temperatures, convective heat transfer coefficients, and time step are used in the energy/conduction equations (see Section 5.2.2). The fluid void fractions are used in the radiation models to determine when radiation heat transfer should be included. The radiation heat transfer rates on the fuel-bundle side of the channel box (both segments) are obtained from the SCDAP radiation model.

The parameters returned from the BWR blade/box model to SCDAP/RELAP5 are shown in the lower half of Figure 5-7. The average wall temperatures, which are used as boundary conditions by RELAP5, are calculated as weighted averages relative to the surface areas of the nodes exposed to each coolant volume. Blocked/missing nodes will sometimes reduce the number of nodes exposed to a coolant volume. For example, at an axial elevation where there is a blockage in the interstitial volume between the control blade and channel box, segment No. 2 of the channel box will be the only node exposed to the interstitial volume. This situation is properly accounted for in the average wall temperature calculations. The blockage will also reduce the flow area of the coolant volume, and this information is returned to RELAP5.

Parameters Obtained From SCDAP/RELAP5

Parameters Returned To SCDAP/RELAP5
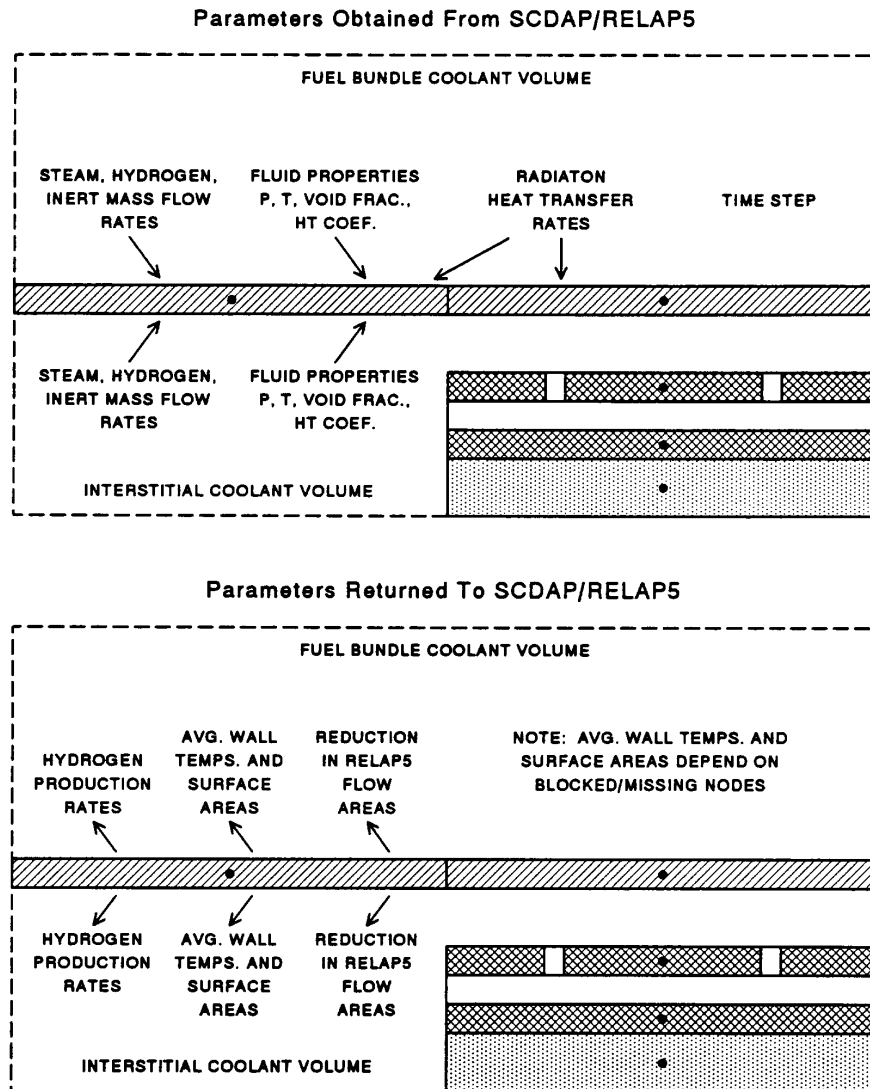
Figure 5-7. Interface information exchanged between SCDAP/RELAP5 and the BWR blade/box model.

5.3 B$_4$C Control Rod Model

Section 5.2 on page 3 describes a new BWR B$_4$C control blade and channel box model, available in SCDAP/RELAP5/MOD3.1, which will eventually replace the older B$_4$C control rod model. However, to accommodate older running input decks, the older model will be available in as part of SCDAP/RELAP5/ MOD3.1. This section describes the older B$_4$C control rod model.

The existence of significant amounts of control rod material in a BWR core might have an important influence on the overall behavior of core degradation and fission product transport during a severe accident

event. The stainless steel cladding/sheath and the boron carbide (B_4C) control rod absorber can be oxidized in the high temperature steam environment. The exothermic oxidation can raise the core temperature, thus increasing the core heatup rate. The combustible gases, such as H_2, CO, and CH_4, generated through control rod oxidation might pose an additional threat to the containment integrity. The borates, produced in the B_4C oxidation, can react to produce cesium borates and alter the distribution of iodine between cesium iodide, hydrogen iodide, and elemental iodine. In order to address these possible impacts, a BWR control rod model has been developed. The model describes the oxidation of the stainless steel cladding/sheath, the B_4C absorber, the heatup, the melting, and the relocation of the B_4C control rods during a BWR severe accident event.

5.3.1   Model Description

This section describes the typical BWR fuel assemblies and control rod module and the possible geometrical modeling of the actual configuration. It also presents the theory for the oxidation kinetics of the stainless steel cladding/sheath and the B_4C absorber. Models for describing the control rod temperature response, control rod melting and relocation, and the slumping of unsupported control rod segments are also provided.

A typical BWR control rod consists of a sheathed cruciform array of stainless steel tubes filled with B_4C powder. Each control rod is surrounded by four fuel assemblies. The absorber tube sheath and the tube cladding are made of Type 304 stainless steel. The B_4C powder in the absorber tubes is compacted to about 70% of the theoretical density. The B_4C is longitudinally separated into individual compartments by stainless steel balls held in place by a slight crimp in the tube. The control rods are cooled (heated during accident conditions) by the core bypass flow. The tube sheaths are perforated to allow the coolant to circulate freely about the absorber tubes.

Due to the complexity of the actual configuration, a cylindrical rod geometry is assumed in this model. For each B_4C control rod, the equivalent stainless steel cladding outer radius and thickness are used to represent both tube cladding outer radius, thickness, and the associated portion of the stainless steel sheath for this tube. There are several types of nodalizations that can be used to model the geometry of fuel assemblies and the control rod module, as shown in Figure 5-8. As shown in Figure 5-8a, the control rod module together with the four surrounding fuel assemblies are considered as a single channel. The enclosure of the channel is modeled by an equivalent shroud component. The four fuel assemblies can be modeled by one to four individual fuel components. The control rod module is modeled by a BWR control rod component. Figure 5-8b shows a different type of nodalization. Each of the four fuel assemblies is modeled by a fuel component and an enclosure shroud component which forms an individual channel. The control rod module is modeled by a control rod component and its bypass core flow to form an additional channel. The third type of nodalization is shown in Figure 5-8c. The four fuel assemblies are modeled by a representative channel with a fuel component and a surrounding shroud component. The control rod module is modeled by a core bypass channel with a control rod component.
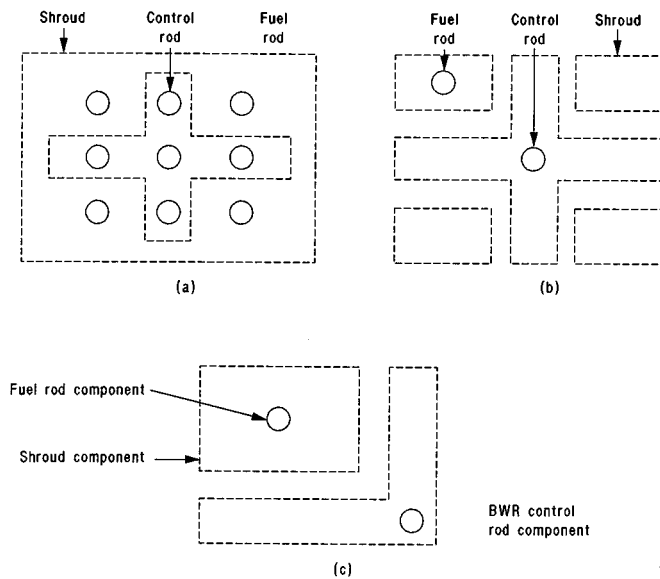
Figure 5-8. Nodalization for fuel assemblies and control rods.

5.3.2   Oxidation

The stainless steel oxidation considers the following chemical reaction:

$$Fe + H_2O \longrightarrow FeO + H_2 . \tag{5-10}$$

The stainless steel weight gain and the FeO layer growth are defined by Equation (3-1). Hydrogen production and heat generation are handled by the oxidation model described in Section 3.

For the oxidation of B_4C absorber, the current model considers the following chemical reaction:

$$B_4C + 7 H_2O \longrightarrow 2 B_2O_3 + 7 H_2 + CO . \tag{5-11}$$

Due to the lack of experimental data, an exponential oxidation model is used and is described by the following equations:

$$\frac{dM_{BC}}{dt} = -R(T) M_{BC} \tag{5-12}$$

$$R(T) = CT + D \tag{5-13}$$

where

M_{BC} =   mass of B_4C at time t (kg)

$R(T)$ =   reaction rate coefficient, assumed to be a linear function of the B_4C temperature (T).

The reaction rate coefficient is further assumed to be zero when the B_4C temperature is < 1,700 K (stainless steel cladding melting point) and 1.0 at 2,700 K (B_4C melting point). Thus, the linear fitting constants, C and D, are 1.0 E-3 and -1.7, respectively. The reaction rate coefficient $R(T)$ as a function of B_4C temperature is shown in Figure 5-9. If the B_4C temperature is assumed to be constant during a time step, t , the above equation can be integrated to obtain

$$M_{BC} = M_{BC,O}e^{[-R(T)\Delta t]} \tag{5-14}$$

where $M_{BC,O}$ is the mass of B_4C at the beginning of the current time step. Once the mass of oxidized B_4C during the current time step is known, the oxidation heat generation can be obtained from the reaction heat.

Both the stainless steel and B_4C oxidation consider the unoxidized mass limitation and the steam supply limitation during each time step advancement.
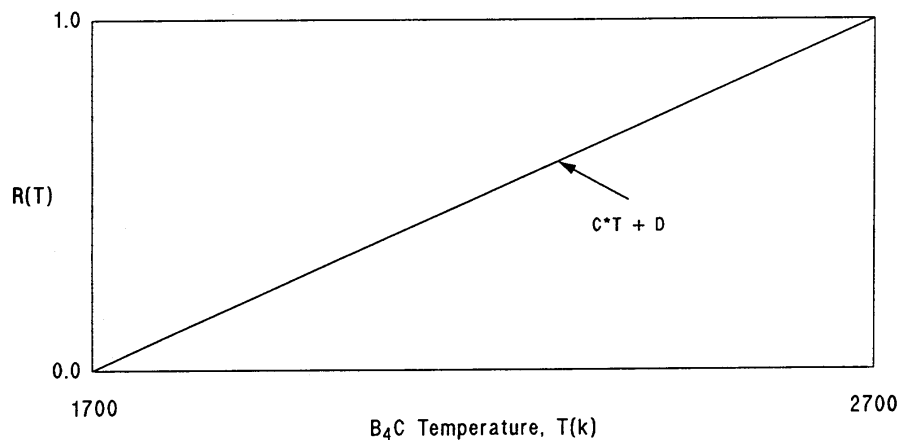
Figure 5-9. B_4C oxidation rate coefficient as a function of temperature.

5.3.3 Temperature Response

A one-dimensional, two region energy balance equation is used to predict the absorber and cladding temperature responses. The schematic nodalization for the temperature response calculation is shown in Figure 5-10. The differential equations that govern the region temperature response can be written as:

Core Components

$$M_1 C_1 \frac{dT_1}{dt} = Q_{cond} + Q_{ox, 1} \tag{5-15}$$

$$M_2 C_2 \frac{dT_2}{dt} = -Q_{cond} + Q_{conv} + Q_{rad} + Q_{ox, 2} \tag{5-16}$$

where

M_1, M_2	=	mass of absorber and cladding, respectively
C_1, C_2	=	specific heat of absorber and cladding, respectively
t	=	time
Q_{cond}	=	conduction heat transfer rate at the interface between the absorber and the cladding regions
Q_{conv}	=	convective heat transfer rate at the control rod surface
Q_{rad}	=	radiation heat transfer rate at the control rod surface
$Q_{ox,1}$	=	B_4C oxidation heat generation rate
$Q_{ox,2}$	=	stainless steel oxidation heat generation rate.
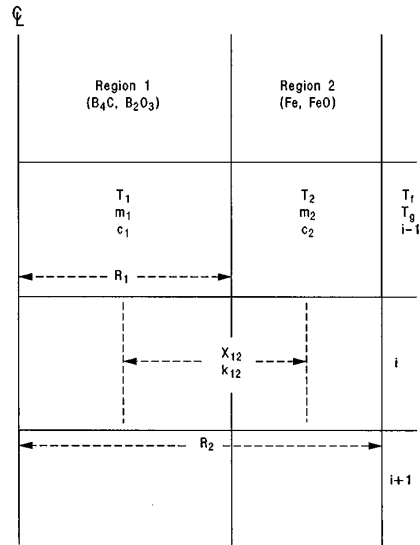
Figure 5-10. One-dimensional, two region nodalization for temperature response calculation.

The convective and conductive heat transfer rates can further be expressed as

$$Q_{conv} = A_2[(h_f (T_f - T_2) + h_g (T_g - T_2)] \tag{5-17}$$

$$Q_{cond} = k_{12} A_1 (T_2 - T_1)/X_{12} \tag{5-18}$$

where

A_1, A_2	=	surface areas of absorber and cladding, respectively
h_f, h_g	=	convective heat transfer coefficients between rod surface and liquid phase coolant, and between rod surface and vapor phase coolant, respectively
T_f, T_g	=	temperatures for the liquid phase and vapor phase coolant
k_{12}	=	effective conductivity across the absorber and the cladding regions
X_{12}	=	effective conduction distance.

The convective heat transfer rate between the control rod surface and the surrounding coolant is calculated using the RELAP5 heat transfer package. The calculation of radiation heat transfer rate depends on the geometric model. For the first type of model, as shown in Figure 5-8a, the radiation heat transfer rate is calculated as in the original SCDAP radiation model. For the other types of geometrical models, as shown in Figures 5-8b and 5-8c, radiation heat exchange between two parallel planes (fuel canister wall and control rod sheath) is assumed. The radiation heat transfer rate on one of the control rod surfaces can be expressed as:

$$Q_{rad} = \frac{\frac{\sigma A}{n}(T_s^4 - T_2^4)}{\frac{1}{\varepsilon_s} + \frac{1}{\varepsilon_2} - 1} \tag{5-19}$$

where

$\varepsilon_s, \varepsilon_2$	=	surface emissivities for fuel assembly canister wall and control rod sheath
A	=	surface area for fuel assembly canister wall or control rod sheath which are facing each other
T	=	temperature at the outer surface of the fuel assembly canister wall
n	=	number of control rod tubes within a control rod module
σ	=	Stefan-Boltzmann constant.

During a time step, Δt, Equations (5-15) and (5-16) can be expressed in difference forms

$$M_1 C_1 (T_1^{(n)} - T_1^{(o)}) = \frac{k_{12} A_1 \Delta t (T_2^{(n)} - T_1^{(n)})}{x_{12}} + Q_{ox,1}^{(n)} \Delta t \tag{5-20}$$

$$M_2 C_2 (T_2^{(n)} - T_2^{(o)}) = \frac{-k_{12} A_1 \Delta t (T_2^{(n)} - T_1^{(n)})}{x_{12}}$$

$$+ A_2 \Delta t [h_f^{(n)} (T_f^{(n)} - T_2^{(n)}) + h^{(n)} (T_g^{(n)} - T_2^{(n)}) + Q_{rad}^{(n)} \Delta t + Q_{ox,2}^{(n)} \Delta t] \tag{5-21}$$

The end timestep temperatures, $T_1^{(n)}$ and $T_2^{(n)}$, can be solved in terms of the beginning timestep temperatures, $T_1^{(o)}$ and $T_2^{(o)}$, explicitly.

When the control rod cladding is melted away, the B_4C absorber is then exposed to the coolant. The temperature response of the B_4C region is predicted according to a lumped parameter calculation. The difference equation during the timestep, t, is

$$M_1 C_1 (T_1^{(n)} - T_1^{(o)}) = A_1 \Delta t [h_f^{(n)} (T_f^{(n)} - T_1^{(n)}) + h_g^{(n)} (T_g^{(n)} - T_1^{(n)}) + Q_{rad}^{(n)} \Delta t + Q_{ox,1}^{(n)} \Delta t] \ . \tag{5-22}$$

The end timestep temperature, $T_1^{(n)}$, can then be obtained.

5.3.4 Melting and Relocation

Following the conduction solution, should melting occur during the current time step, the amount of material melted is calculated. Since the melting of the materials is not implicitly calculated in the conduction solution, the actual temperature is recalculated through balancing the material internal energy and the heat of fusion.

The downward movement of the molten material is calculated based on the well developed, incompressible viscous film flow over a cylindrical geometry. Considering a cylindrical geometry, as shown in Figure 5-11, the force balance for the liquid film can be expressed as:

$$\frac{d}{dr}(\gamma \zeta_{\gamma z}) = \gamma \rho g \tag{5-23}$$

where

$$\zeta_{\gamma z} = -\mu \frac{dV_z}{d\gamma} \ . \tag{5-24}$$
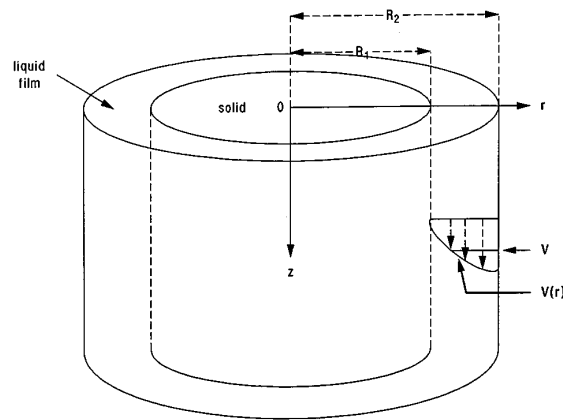
Figure 5-11. Incompressible, viscous film flow over cylindrical geometry.

The boundary conditions are

$$\xi_{yz} = 0 \text{ for } \gamma = R_2 \tag{5-25}$$

$$V_z = 0 \text{ for } \gamma = R_1 \tag{5-26}$$

where

γ	=	the radial coordinate
ρ	=	the liquid film density
g	=	gravitational acceleration
μ	=	the liquid film viscosity
ξ_{yz}	=	viscous shear force
R_1, R_2	=	outer radii for the solid and liquid layers
$V_z(\gamma)$	=	downward liquid film velocity.

From the above equations, the liquid film velocity profile can be obtained as

$$V_z(\gamma) = \frac{\rho g}{4\mu}(R_1^2 - \gamma^2) + \frac{\rho g R_2^2}{2\mu}\ln\left(\frac{\gamma}{R_1}\right) . \tag{5-27}$$

After integrating the velocity profile across the liquid film, the average film velocity, V, is

$$V = \frac{R_1^4}{R_2^2 - R_1^2} + \frac{\rho g}{\mu} + \frac{4x^2 - 1 - 3x^4}{8} + \frac{x^4}{2}\ln(x) \tag{5-28}$$

where $x = R_2/R_1$. Thus, during a time step Δt, the liquid film will travel a distance of $V\Delta t$.

During a time step, the actual computation process starts from the top elevation of the control rod. If melting and relocation occur at the top elevation, the molten material moves to the next lower elevation. The internal energy associated with the relocated molten material is assumed to instantly exchange with the internal energy of the material at this lower elevation. Should the liquefied material at this new elevation still appear, the downward moving calculation for the liquefied material is continued. The process is repeated until the lowest elevation is reached. The amount of molten material dripped below the bottom of the control rod is also tracked for each time step.

5.3.5 Slumping

If the material, which is located anywhere in the middle section of a control rod, has depleted during a time step, then the unsupported control rod segment, located above the empty section, is assumed to fill the empty section and leave an empty region at the top. This slumping process is shown in Figure 5-12. All of the hydraulic volume connections, the changes of the coolant flow area, and the coolant hydraulic diameter are also updated.
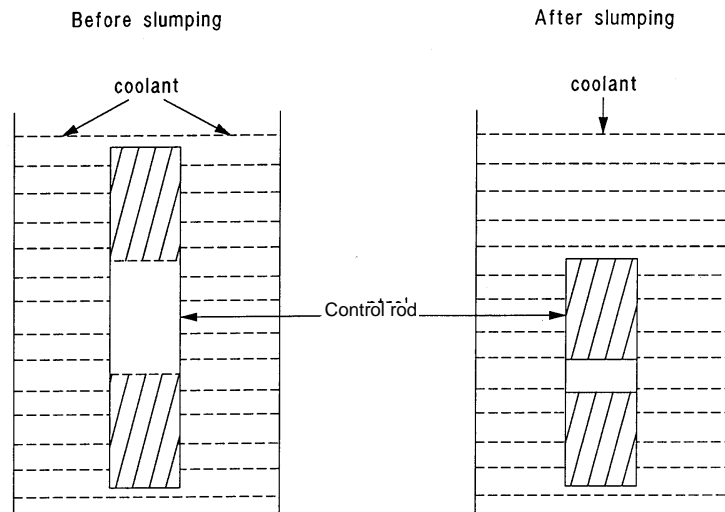
Figure 5-12. Slumping process for unsupported control rod segment.

5.4   Shroud/Reflector Model

Structures in the core, other than fuel and control rods, can be modeled with the shroud/reflector component. This component is intended to be loosely defined within SCDAP/RELAP5, thereby imposing as few assumptions upon the code user as possible. This approach implies that the code user will supply as much information as possible, and does impose restrictions upon the analysis, particularly when loss of geometry is modeled.

5.4.1   Model Description

This component models a structure within the reactor core as an infinite slab, using the basic heat conduction equation described in the section entitled 'Two-Dimensional Heat Conduction Governing Equation'. An internal heat generation term can be specified by the user, identically to that of the fuel rod component. The structures can be defined by multiple layers of materials, with the oxidation and relocation of exterior layers due to melting considered.

The shroud/reflector component requires two to three sets of boundary conditions, depending on the configuration specified by the user. In the minimum configuration, the user must specify a hydrodynamic volume on the internal (reactor) side of the component, as well as on the external side. Additionally, the

user may specify a hydrodynamic volume representing flow channels embedded within the structure.

5.4.2 Oxidation

Oxidation is modeled using the parabolic rate equations described in the section entitled "Parabolic Rate Equation" on page 13.1. Because of the generalization of this component, oxidation is limited to three types of materials. These types of materials are zircaloy based materials (material indices 1 through 3 in "User Specified Materials" on page 101), iron based materials (material indices 18 and 19) and user-specified materials (indices 50 through 59). Zircaloy layers are oxidized using the same kinetics as described for fuel rods.

The stainless steel oxidation considers the following chemical reaction:

$$Fe + H_2O \longrightarrow FeO + H_2 \, . \tag{5-29}$$

The stainless steel weight gain and the FeO layer growth are defined by Equation (3-1). Hydrogen production and heat generation are handled by the oxidation model described in Section 3.

5.4.3 Melting and Relocation

In the situation where the component reaches melting and relocation conditions, and the primary material is zircaloy, the molten zircaloy relocates downward to a region where the structural surface temperature is 200 K less than the solidus temperature of zircaloy.

In the situation where the primary is stainless steel, the material melts and relocates as described in the section 7.4 entitled "Interaction of Molten Pool with Structures at Periphery of Core"

Structures with exterior layers or composed entirely of non-zircaloy/non-iron materials can also be modeled; however, oxidation rate equations must be user specified and no material relocation or loss of geometry can be considered. Both melting and nonmelting models can be used for the structures outside the core as well. The same material limitations apply.

Core Components

6. TWO-DIMENSIONAL DEBRIS AND SURROUNDING STRUCTURES MODEL

A model based upon the COUPLE[4] code is used to calculate the heatup of the debris and/or surrounding structures. This model takes into account the decay heat and internal energy of newly fallen or formed debris and then calculates the transport by conduction of this heat in the radial and axial directions to the wall structures and water surrounding the debris. Perhaps the most important use of this model is to calculate the heatup of the vessel wall so that the time at which the vessel may rupture can be determined. Notable capabilities include the modeling of the following phenomena and conditions: (a) spatially varying porosity, (b) thermal conductivity of porous material, (c) a debris bed whose height grows sporadically with time, (d) radiation heat transfer in a porous material, and (e) the melting or freezing of debris. The limitations of this model are: (a) molten material remains in the location where predicted, (b) oxidation does not occur in the debris bed, and (c) fission product release does not occur in the debris bed.

6.1   COUPLE Description

The COUPLE code is a two-dimensional, finite element, steady state and transient heat conduction code. The code was developed to solve both plane and axisymmetric type heat transfer problems with anisotropic thermal properties, subject to boundary conditions of the first kind (Dirichlet), second kind (Neumen), and third kind (combination of the first and second), and/or nonlinear boundary conditions such as radiation. A boundary condition of the first kind implies that the temperatures are prescribed along the boundary surface. A boundary condition of the second kind implies that the normal derivatives of the temperatures are prescribed at boundary surface. The code solves the following two-dimensional energy equation:

$$(\rho C_v)_e \frac{\partial T}{\partial t} = \frac{\partial}{\partial x}(K_e \frac{\partial T}{\partial x}) + \frac{\partial}{\partial y}(K_e \frac{\partial T}{\partial y}) + Q \qquad (6\text{-}1)$$

where

$$(\rho C_v)_e = P(\rho C_v)_l + (1-P)(\rho C_v)_s (\rho C_v)_e = P(\rho C_v)_l + (1 - P)(\rho C_v)_s \qquad (6\text{-}2)$$

ρ	=	density (kg/m^3)
C_v	=	constant volume specific heat
K	=	thermal conductivity
Q	=	volumetric heat generation rate (W/m^3)
T	=	temperature
P	=	porosity (pore volume/total volume)
e	=	equivalent
l	=	liquid
s	=	solid.

6.2   Variable Element Porosity

The COUPLE code allows each element in the debris bed model to have its own value of porosity. The porosity of each element can also be varied as a function of time. The thermal property of each element is determined by

$$\Phi = P\phi_f + (1 - P) \phi_s \tag{6-3}$$

where

Φ	=	average thermal property value, such as thermal conductivity or specific heat
ϕ	=	thermal property
P	=	porosity
f	=	fluid
s	=	solid.

If the porosity is zero, the element represents a volume containing solid debris material, whereas a porosity value of 1.0 means the element is completely filled with coolant. A value between 0.0 and 1.0 indicates that the volume contains both coolant and debris material.

6.3   Thermal Conductivity Model

The heat transfer in a dry porous bed involved both conduction and radiation. The overall thermal conductivity of the bed can be represented as

$$K_{et} = K_{ec} + K_r \tag{6-4}$$

where

K_{et}	=	total effective conductivity
K_{ec}	=	effective conductivity (conduction only)
K_r	=	radiation conductivity.

A number of thermal conductivity models have been proposed for modeling a dry porous bed. Reference 76 gives a good review and comparison of five such models. The Imura-Takegoshi[77] model combined with the Vortmeyer[78] radiation model yields the best overall results and produces an upper bound on the temperature.

The Imura-Takegoshi model[77] in equation form is given as follows:

$$K_{ec} = \Psi + \frac{1 - \Psi}{\phi + \dfrac{1 - \phi}{\nu}} \tag{6-5}$$

$$\phi = 0.3P^{1.6}\upsilon^{-0.44} \tag{6-6}$$

$$\upsilon = \frac{K_g}{K_s} \tag{6-7}$$

$$\Psi = \frac{P - \phi}{1 - \phi} \tag{6-8}$$

where

K_g =   gas or vapor thermal conductivity

K_s =   solid thermal conductivity

P   =   porosity.

The Vortmeyer model[78] is given as

$$K_r = 4\eta\sigma DT^3 \tag{6-9}$$

where

η =   radiation exchange factor

σ =   Stefan-Boltzmann constant

D   =   particle diameter

T   =   temperature.

The combined Imura-Takegoshi and Vortmeyer model is input into the CNDUCT subroutine of COUPLE. The combined model calculates the effective thermal conductivity of porous debris by the following three equations:

$$k_{eff} = k_g(k_{ec} + k_r) \tag{6-10}$$

$$k_r = ((1 + \varepsilon) / (1 / k_{ec} + k_g / k_a)) + \varepsilon k_a \tag{6-11}$$

$$k_a = (\pi / 4) \, dp \, (0.277 / (2 / \varepsilon - 0.264)) \, (T / 100.)^3 \, (10)^{-6} \tag{6-12}$$

where

k_{eff} =   effective thermal conductivity of porous debris (W/m•k)

k_r =   term to account for radiation

k_{ec} =   factor to account for solids

k_a =   effective conductivity for radiation (W/m•K)

ε =   emissivity of debris (user-defined)

d_p =   particle size of debris (m).

A lower bound model is available which combines a conduction model by Wilhite[79] with a radiation model by Luikov.[80] This lower bound model has not been applied by the COUPLE model.

6.4   Phase Change Model

At the present time, there are two generally accepted ways of numerically approximating a phase change problem. One method uses a moving mesh technique. At this time, the moving mesh technique has been mainly applied to one-dimensional problems. This technique is not easily applied to two-dimensional problems because mesh distortion may result.

The other method uses a fixed mesh and is usually referred to as an enthalpy method. The particular method that has been chosen is described in Reference 76. The method consists of using the material enthalpy to determine an effective density times specific heat (ρC_p) value to use in Equation (6-1). The enthalpy change per unit volume is defined as

$$dH = \rho C_p dT \tag{6-13}$$

thus,

$$\rho C_p = dH/dT \tag{6-14}$$

which can be written as

$$\rho C_p = \left(\frac{dH}{dX}\right)\left(\frac{dX}{dT}\right) \tag{6-15}$$

where X is the coordinate boundary of a phase change (m).

For computational purposes, it is easier to calculate dH/dX and dX/dT than it is dH/dT directly. The necessary coding required to use this approach is contained in the subroutine USERP.

6.5   Dryout of Debris

The COUPLE model uses a simplified model based on the volume fraction of liquid in the open porosity of the debris to determine whether the debris is in a state of dryout. The volume fraction of liquid is calculated by RELAP5. If the void fraction of liquid in the open porosity of the debris is equal to zero, then the debris is in a state of dryout. If the fraction of liquid is greater than zero, then the debris is considered to be quenched. In this case, all of the heat generation in the debris is applied to boiling off the liquid water in the open porosity of the debris. The amount of heat transferred from debris to coolant is added to the energy term for the RELAP5 control volume modeling the fluid in the open porosity of the debris and the amount of coolant boiloff is added to the vapor generation term for this RELAP5 control volume. If all of the water is boiled off, then the debris is considered to be in a state of dryout. In this case, the COUPLE model calculates debris heatup considering steam in the voids in the debris bed. The COUPLE model has the O-d Lipinski equation,[81] which calculates dryout as a function of debris power density, depth, porosity,

particle size, and coolant properties. This equation, however, is not applied in the calculation of the heatup of the debris in the lower plenum.

6.6   Heat Transfer at Surface of COUPLE Finite-Element Mesh

Convective and radiative heat transfer boundary conditions may be applied at all external surfaces of a finite-element mesh. Convective heat transfer coefficients and radiation sink temperatures will be provided at the surfaces of the COUPLE finite element mesh through interfaces with the RELAP5 code.[82] The boundary conditions are

$$(-K_{et}) \frac{\partial}{\partial n} T(z_b, r_b) = h_c(z_b, r_b) [T(z_b, r_b) - T_c(z_b, r_b)] + q_{rad}(z_b, r_b) \tag{6-16}$$

where

$T(z_b,r_b)$ = temperature of external surface of node on COUPLE finite element mesh with coordinates of z_b, r_b (K)

z_b = elevation of node on external surface of finite element mesh (m)

r_b = radius of node on external surface of finite element mesh (m)

n = coordinate in direction normal to external surface (m)

$h_c(z_b,r_b)$ = RELAP5-calculated convective heat transfer coefficient for node on external surface with coordinates z_b,r_b (W/m^2•K)

$T_c(z_b,r_b)$ = RELAP5 calculated (K)

$q_{rad}(z_b,r_b)$ = radiation heat flux (W/m^2).

6.7   Natural Convection of Liquefied Debris

Debris may liquefy and mix due to natural convection. This mixing will cause a pool of liquefied debris to have a nearly uniform temperature. The effect of natural convection on the heat transfer at the interface of a molten pool and the structural material supporting it is modeled. This model is the same as that described in Reference 83. If the object is to only calculate the heat transfer effect associated with natural convection in the molten pool, an empirical correlation can be used to determine the convective heat transfer coefficient to be applied at the liquid-solid interface. Since COUPLE is strictly a heat conduction code, an effective conductivity was used to simulate the convective heat flux at the phase change interface. The effective conductivity, k_e, in the liquid portion of the phase change element was calculated by requiring that the conduction heat flux in the liquid portion of the element $k_e \frac{\partial T}{\partial n}$ be the same as the imposed convective heat flux [h(T_p - T_s)]. Hence the effective conductivity becomes

$$k_e = \frac{h(T_p - T_s)}{\frac{\partial T}{\partial n}} \tag{6-17}$$

where

h = convective heat transfer coefficient

COUPLE

T_p	=	molten pool temperature
T_s	=	interface temperature (material melting temperature)
$\dfrac{\partial T}{\partial n}$	=	temperature gradient in the liquid normal to the solid-liquid interface.

For fully liquid elements, the element conductivity is set to a large number (factor of 100 greater than that before melting) to simulate a well mixed, highly turbulent pool.

To determine the transfer coefficients used in Equation (6-17), knowledge is required of the heat flux at the phase change interface. As discussed by Epstein,[84] this requires a heat transfer correlation for natural convection in the molten pool at temperatures greater than the melting temperature of the liquefied material. However, no such data exist for high-temperature, hemispherical, molten pools.

Following Epstein's approach, the correlations for Mayinger et al.[85] was used to calculate the required heat transfer coefficient for Equation (6-17). These correlations were developed using low-temperature water pools in semicircular geometry. The correlations were applied by Epstein and Fauske[72] to the analysis of the molten pool of reactor material that evolved during the heatup stage of the TMI-2 accident. The correlations assume that the pool is in steady state. If the pool is rapidly increasing in temperature, the heat loss from the molten pool is overpredicted.

The correlation in Reference 86 yields a mean upward heat transfer coefficient to the upper crust covering the molten pool of

$$h_u = \frac{k}{R} 0.36 \mathrm{Ra}^{0.23} \tag{6-18}$$

and a mean downward heat transfer coefficient of

$$h_d = \frac{k}{R} 0.54 \mathrm{Ra}^{0.18} \tag{6-19}$$

where

k	=	thermal conductivity of the melt in the boundary layer adjacent to the phase change interface (W/m•K)
R	=	effective radius[a] of the molten region (m)
Ra	=	Rayleigh number associated with the molten pool.

The Rayleigh number is defined as

$$\mathrm{Ra} = \frac{g\beta Q R^5}{\alpha v k} \tag{6-20}$$

where

---

a. Only one molten pool is considered for the entire debris bed. By summing the volume of elements that are melted, and by assuming a hemispherical geometry, the effective radius is calculated.

g = gravitational constant (9.8m/s^2)

Q = volumetric heat generation rate (W/m^3)

β = coefficient of volumetric expansion (1/K)

α = thermal diffusivity (m^2/s)

ν = kinematic viscosity of the molten materials (m^2/s).

Experimental results published by Jahn and Reineke[86] indicate that the local downward heat transfer coefficient is a function of the angular position from the centerline of the molten pool. Their result show that the ratio of the local Nusselt number to the mean Nusselt number (NU_l/NU_m) varies from 0.2 at $\theta = 0.0$ to 2.0 at $\theta = 90.0$. For modeling purposes, their results were approximated as shown in Figure 6-1, where θ is determined as shown in Figure 6-2. The elements which are determined to be in the process of phase change are identified by the code; and the appropriate upward and downward heat transfer coefficient [as determined by using Equations (6-18) and (6-19) and an analytical representation of Figure 6-1 are applied to the appropriate elements.
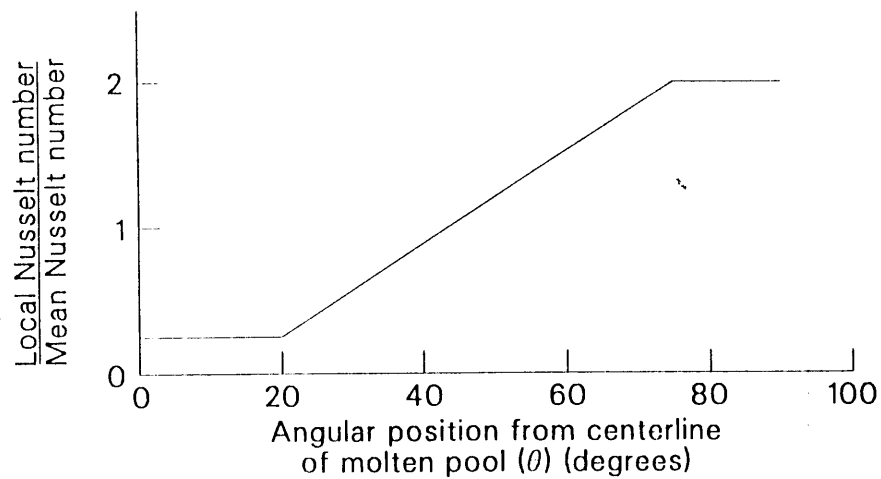
Figure 6-1. Nusselt number ratio as a function of the angle from core centerline.
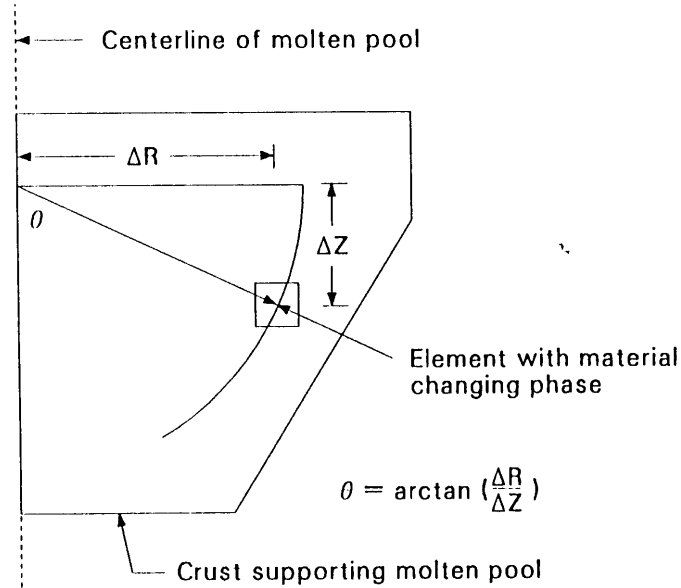
Figure 6-2. Schematic defining the location of a typical phase change element.

6.8   Heat Transfer at Interface of Debris Region and Structure

The rate of heat transfer from a debris region into a structure in contact with the debris is a strong function of the conditions at the interface between the debris and structure. The modeling of this heat transfer is performed using the concept of a null element, which is an element with zero volume and whose nodes overlay the interface between the debris and the structure. Null elements are defined by the code user along possible interfaces between debris and structure. The heat transfer through the null elements is calculated by the equation

$$q_i = h_{gap} (T_d - T_s) \tag{6-21}$$

where

$$q_i \qquad = \qquad \text{heat flux across the interface}$$

$$h_{gap} \qquad = \qquad \text{gap heat transfer coefficient (W/m}^2\text{•K)}$$

$$T_d \qquad = \qquad \text{temperature of rods in debris at the interface (K)}$$

$$T_s \qquad = \qquad \text{temperature of corresponding rods in the structure at the interface (K).}$$

The debris and structure node have the same coordinates but different identification numbers. The debris node is part of a finite element modeling the debris and the structure node is part of a finite element modeling the structure in contact with the debris. The heat flux calculated by Equation (6-21) is applied at both the surface of the finite element with debris that faces the structural element and the surface of the

structural element that faces the debris element.

The modeling of the gap heat transfer coefficient is divided into two regimes: (1) solidified debris, and (2) liquefied debris. The two regimes are illustrated in Figure 6-3. For the solidified debris regime, the heat transfer is a function of the surface roughness of the debris and structure and of other parameters. For this regime, the debris model does not attempt to calculate the gap heat transfer coefficient. Instead, the gap heat transfer coefficient is defined from user input. In the liquefied debris regime, a gap heat transfer coefficient is calculated based on the rate of heat transfer through the thermal boundary layer between the liquefied debris and the structure in contact with the liquefied debris. For an interface at the bottom surface of a part of liquefied debris, the gap heat transfer coefficient is calculated by

$$h_{gap} = 2.06 \frac{k}{R} Ra^{0.095} \qquad (6-22)$$

where

k = thermal conductivity of liquefied debris (W/m·K)

R = effective radius of liquefied debris (m)

Ra = Rayleigh number of liquefied debris.

For an interface along a vertical surface, the gap heat transfer coefficient is calculated by

$$h_{gap} = 1.32 \frac{k}{R} Ra^{0.19} . \qquad (6-23)$$

Figure 6-3. Modeling of heat transfer across structure-debris interface.

7. SIMPLIFIED CORE REGION LUMPED PARAMETER DEBRIS MODELING

Damage mechanisms exist during a severe accident in an LWR that can change a reactor core from an array of distinct cyli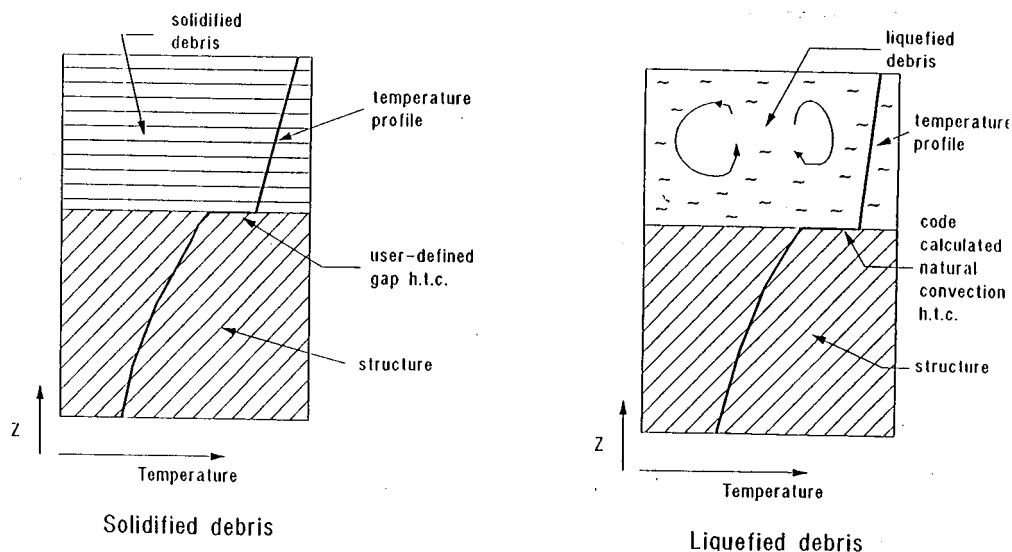ndrical fuel rods located in the center of the reactor vessel to a deep debris bed located in the bottom of the vessel. The reactor vessel itself becomes vulnerable to heatup and damage after the core has relocated to the lower head. The TMI-2 accident[62] and severe fuel damage experiments[20,61,87,88,89,90] have shown that reactor core damage proceeds through several stages before the core slumps to the lower head. These stages of damage progression include (a) embrittlement of cladding due to oxidation, (b) melting of metallic cladding and dissolution of fuel in contact with liquefied cladding, (c) slumping of liquefied cladding and dissolved fuel due to failure at the oxide shell containing the liquefied mixture, (d) solidification of the slumped mixture at a lower and cooler location in the core and concurrent formation of a nonporous debris region that blocks the flow of coolant, (e) meltdown of the reactor core into a molten pool supported by the nonporous debris, and (f) melt-through of the nonporous debris and slumping of the molten pool to the bottom of the reactor vessel. An hour or more of time may elapse before damage has progressed through these six stages. This order of damage progression is established by the differences in melting temperatures of the metallic and ceramic parts of the reactor core. It is also established by the fact that the lower part of the reactor is the last part of the core to be uncovered by water and that this part has a lower level of decay heat than the center of the core.

The damage progression can be either abated or intensified by the injection of water into the reactor vessel. On one hand, the injected water may cool the damaged core and stop damage progression. On the other hand, the injected water may shatter embrittled fuel rods so that the fuel rod fragments slump into the configuration of a porous debris bed.

Models to predict the progression of reactor core damage have been developed and incorporated into SCDAP/RELAP5. These models calculate the changes in the configuration of the reactor core as damage progresses. The models also calculate the heatup and progression of melting in the damaged regions of the reactor core. This section describes these models for damage progression.

The reactor core can change into three basic configurations as damage progresses during a severe accident. In the first configuration, nonporous debris supported by intact fuel rods extends radially across the core. This configuration is the result of the meltdown of the metallic part of the reactor core. In the case of the TMI-2 accident, this nonporous debris was in the shape of a crucible.[91] The second basic configuration is that of a porous debris bed. The third basic configuration is that of a molten pool supported and contained by the nonporous debris. Before damage has occurred, the configuration of the core is characterized by parameters such as rod spacing and rod diameter. After damage has occurred, the configuration is characterized by parameters such as depth and porosity of debris. If the porosity is large and the debris is covered with water, then most of the decay heat in the debris can be removed by convective cooling. But, if the porosity is small and the debris bed is deep, then a large molten pool may develop. At this stage, there is the potential for rapid slumping of a large amount of hot material onto the lower head of the reactor vessel and the possibility of a vigorous thermal attack of the lower head.

The damage thresholds that result in the formation of debris are shown in Figures 7-1 to 7-4. Each of these figures show part of a reactor core that is nodalized with three axial nodes and two rod groups. The bottom part of these figures show variables that describe the state of the core in this region. Each change in

the state of the reactor core that causes a local change in configuration of the reactor core is identified with a configuration change number. A total of five configuration changes are identified in these figures.

The variables in Figure 7-1 are defined as follows. The variable T(2,1) is the temperature of the material at axial node 2 of Rod Group 1. The variable Δr_β (2,1) is the thickness in mm of the beta phase of the zircaloy in the cladding at axial node 2 of Rod Group 1. The variable Δr_{ox} (2,1) is the thickness in mm of the oxide layer of the cladding at axial node 2 of Fuel Rod Group 1.

Figure 7-1 shows damage thresholds that result in intact fuel rods changing into rubble debris. This figure uses the location of the core at axial node 2 of Rod Group 1 as an example. The figure shows two different changes in the state of the reactor core at axial node 2 of Fuel Rod Group 1 that result in the rods at this location in the reactor core changing from the configuration of intact rods to that of rubble debris. Two different changes in state of the fuel rods can result in the formation of rubble debris. The first change is the result of the temperature of embrittled fuel rods decreasing to where it is less than the fragmentation temperature, which is defined to be the saturation temperature plus 100 K. The second change applies to fuel rods that have not significantly oxidized. In this case, if the temperature at this location exceeds the melting temperature of the zircaloy cladding, then the fuel rods disintegrate into rubble debris. The third damage threshold involves a change in configuration of the rods adjacent to the bottom and top of axial node 2 of Rod Group 1. If the adjacent material is rubble debris, then the material between the two locations with rubble debris is also considered to change to the configuration of rubble debris.

Figure 7-2 shows the change in state that results in a location of the reactor core having cohesive debris. In this figure, the variable d is the thickness (mm) of material that has slumped and frozen and that completely fills in the space between fuel rods. If the thickness is less than 0.05 m, the relocated material is regarded as not being coplanar, and thus, as not blocking the flow of coolant. If this thickness exceeds 0.05 m, then the slumped material is regarded as cohesive debris that blocks the flow of coolant in the axial direction. The cohesive debris does not block flow in a direction perpendicular to the longitudinal axis of the fuel rods. At an axial node with cohesive debris, the portion of the node above the cohesive debris continues to be represented as intact fuel rods.

Figures 7-3 and 7-4 show the changes in state of the reactor core that result in the formation of a molten pool. Figure 7-3 shows molten pool formation due to temperature change. If the temperature at any location in the reactor core exceeds the melting temperature of the mixture of UO_2 and ZrO_2 at that location ($T_{melt\ Zr-U-O}$), then that location of the core is regarded as having molten material and is subsequently represented by the molten pool model. The example shown in Figure 7-3 has the location that became molten previously being rubble debris. The same change to the configuration of a molten pool would have occurred if the material at that location was in the configuration of intact fuel rods at the time that its temperature exceeded the melting temperature of the mixture of UO_2 and ZrO_2 at that location. Figure 7-4 shows the case of a location with rubble debris being supported by a crust at the top of molten material beneath it. If the thickness of this crust (ΔZ) decreases to a value of less than 5 mm, then the rubble debris is regarded as sinking into the molten pool and becoming part of the molten pool.

The spreading of a molten pool due to gravity driving the molten material through adjacent porous regions can also result in locations in a reactor core changing from the configuration of intact fuel rods or rubble debris to the configuration of a molten pool. This process for changing the configuration of a reactor core is described in Section 7.3.3.
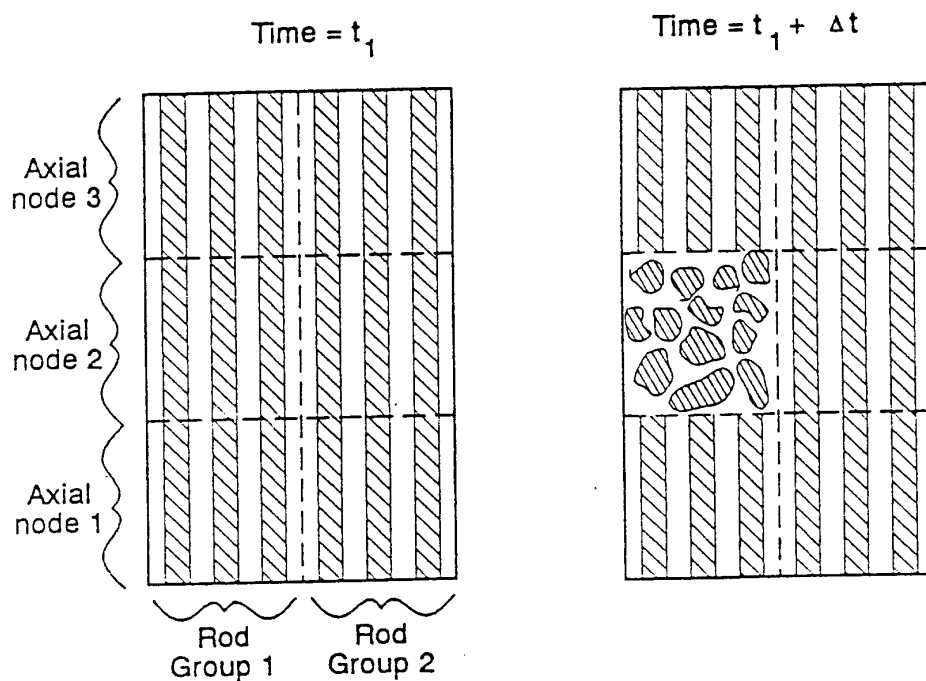
Core state change that results in change in configuration
for axial node 2 of Rod Group 1

Configuration Change No.	Time = t_1	Time = $t1 + \Delta t$
1	$T(2,1) > T_{frag}$ $\Delta r_\beta(2,1) < 0.1$	$T(2,1) < T_{frag}$ $\Delta r_\beta(2,1) < 0.1$
2	$T(2,1) < T_{Zr\,melt}$ $\Delta r_{ox}(2,1) < 1.E-5$	$T(2,1) > T_{Zr\,melt}$ $\Delta r_{ox}(2,1) < 1.E-5$

Figure 7-1. Damage thresholds for changing local configuration of core from intact rods to rubble debris.
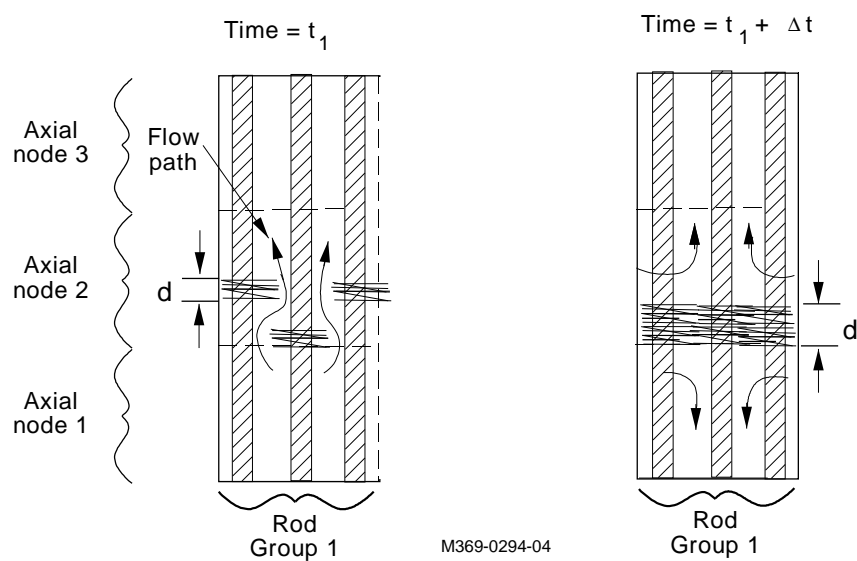
Core state change that results in change in configuration
for axial node 2 of Rod Group 1

Configuration Change No.	Time = t_1	Time = t1 + Δt
3	$d < 0.05$ m	$d \geq 0.05$ m

Figure 7-2. Damage threshold for changing local configuration of core from intact rods to cohesive debris.
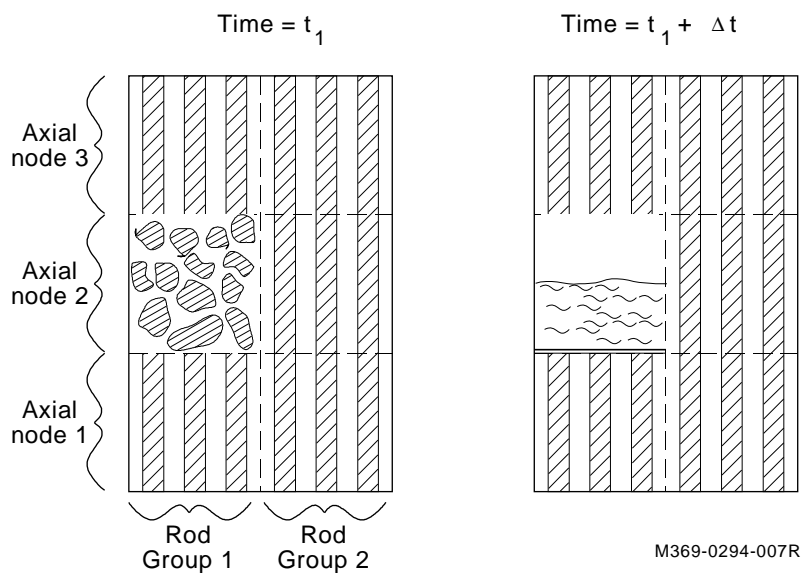
Time = t$_1$ Time = t$_1$ + Δt

Axial node 3

Axial node 2

Axial node 1

Rod Group 1   Rod Group 2

M369-0294-007R

Core state change that results in change in configuration
for axial node 2 of Rod Group 1

Configuration Change No.	Time = t$_1$	Time = t1 + Δt
4	$T(2,1) < T_{melt\ Zr-U-O}$	$T(2,1) \geq T_{melt\ Zr-U-O}$

Axial node —— / \ —— Rod group

Figure 7-3. Damage threshold for changing local configuration of core from intact rods or rubble debris to molten pool.
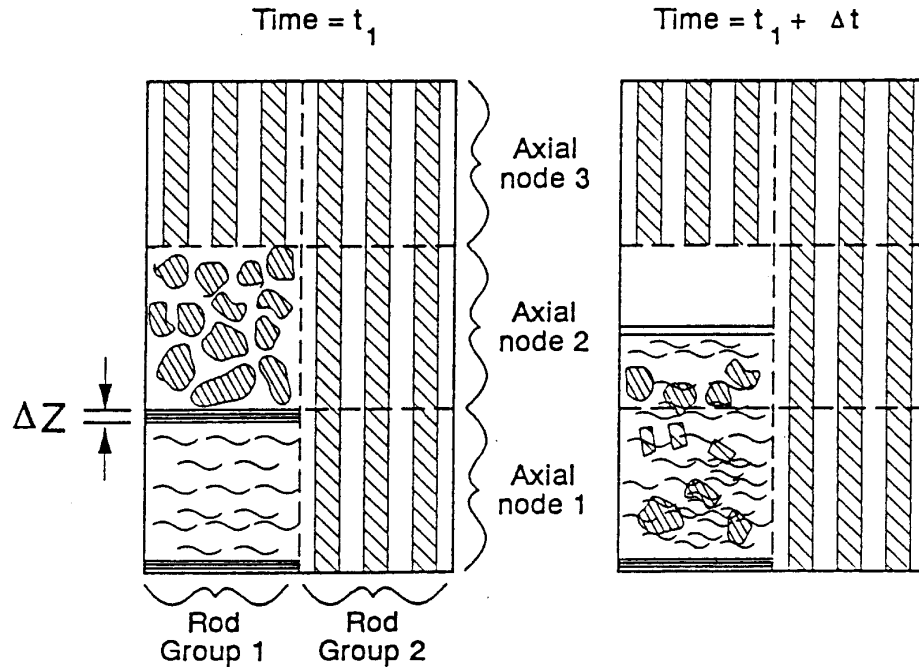
Core state change that results in change in configuration
for axial node 2 of Rod Group 1

Configuration Change No.	Time = t_1	Time = $t1 + \Delta t$
5	$\Delta Z \geq .5$ mm	$\Delta Z < .5$ mm

Figure 7-4. Damage threshold for changing local configuration of core from intact rods or rubble debris to molten pool.

7.1   Formation and Heatup of Nonporous Debris

The degeneration of part of the reactor core into nonporous debris is a state of damage caused by the meltdown of control rods and the metallic part of fuel rods. The meltdown may begin as soon as a region of the core exceeds the temperature for eutectic melting of stainless steel clad control rods with Ag-In-Cd absorber material. This temperature is about 1,500 K. The meltdown becomes widespread when a region of the reactor core exceeds the melting temperature (about 2,200 K) of the fuel rod cladding. The meltdown and subsequent solidification of the relocated metallic material may completely fill in the space between fuel rods and result in a nonporous debris bed that consists of a metallic hardpan with embedded, intact fuel rods. The thickness varies depending upon the extent of oxidation of the cladding and the extent of fuel dissolution by the liquefied cladding. In the case of the TMI-2 accident, the metallic nonporous debris was 0.05 - 0.10 m thick. The nonporous debris usually begins to form first in the hot center part of the core and then spreads radially outward as the outer portions of the core oxidize and melt down.

The layer of slumped and solidified material that results from fuel rod meltdown is treated as a nonporous debris bed with a thickness varying in the radial direction. Figure 7-5 shows the configuration of nonporous debris and the heat transfer considered to take place within the debris. The thickness of the debris is constant within each user defined group of fuel rods. A fuel rod group is a collection of fuel rods defined by the code user to have identical behavior. The behavior of one representative rod in the group is calculated, and all of the other rods are considered to behave in identical behavior. The temperature variation in the axial direction in the nonporous debris is calculated. The temperature gradient in the radial direction in the nonporous debris is assumed to be negligible. Based on this simplifying assumption, the heatup and melting of the nonporous debris within each fuel rod group is calculated, taking into account axial heat conduction and the transfer of heat by convection and radiation from the bottom and top surfaces of nonporous debris. The internal heat generation in the embedded fuel rods is also taken into account.

The heatup of nonporous debris is calculated by the heat conduction model for intact fuel rods from the time of debris formation until the intact fuel rods immediately above the nonporous debris become molten. After this, a heatup model specific to the nonporous debris is employed. The heatup model for intact fuel rods takes into account the presence of nonporous debris. The surface area of fuel in contact with the coolant and that may oxidize is reduced to account for the part of the intact rods that have been covered with the nonporous debris. The heat generation in the nonporous debris is taken into account. The hydrodynamic model takes into account the blockage caused by the nonporous debris.

After the nonporous debris supports molten material, an integral method is used to calculate the heatup of nonporous debris. The heatup is calculated by

$$\alpha \left[\frac{\partial}{\partial z} T\left(\delta, t\right) - \frac{\partial}{\partial z} T\left(0, t\right) \right] = \frac{\partial}{\partial t}\left[\int_0^\delta T\left(z, t\right) dz \right] - \frac{\delta \dot{q}}{\rho C_p} \tag{7-1}$$
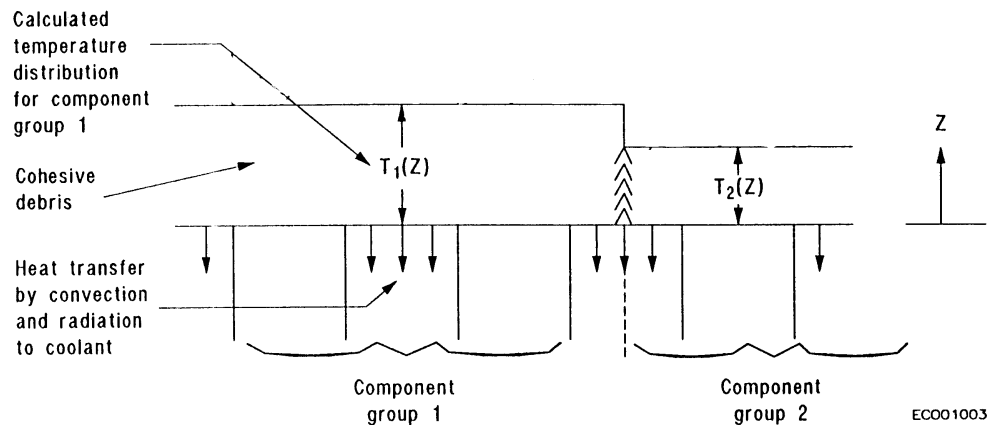
Figure 7-5. Heat conduction process modeled for cohesive debris.

where

α = thermal diffusivity of nonporous debris (m^2/s)

δ	=	thickness of nonporous debris (m)
$T(z,t)$	=	temperature of nonporous debris (K)
t	=	time (s)
z	=	elevation (m); $z = 0$ = bottom surface of debris; $z = \delta$ = top surface
$\dot{q}$	=	volumetric heat generation rate in debris, including heat generation of fuel rods embedded in debris (W/m^3)
ρ	=	density (kg/m^3)
C_p	=	heat capacity (J/kg $\cdot$ K).

The boundary conditions applied to Equation (7-1) are:

$$k\frac{\partial}{\partial z}T(0, t) = \varepsilon\sigma[T^4(0, t) - T^4_{cool}] + h_{conv}[T(0, t) - T_{cool}] \tag{7-2}$$

$$k\frac{\partial}{\partial z}T(\delta, t) = q_d \tag{7-3}$$

where

k	=	thermal conductivity (W/m $\cdot$ K)
ε	=	emissivity
σ	=	Stefan-Boltzmann constant (5.668 E^{-8} W/m^2 $\cdot$ K^4)
T_{cool}	=	coolant temperature (K)
h_{conv}	=	convective heat transfer coefficient (W/m^2 $\cdot$ K)
q_d	=	heat flux from molten pool into nonporous debris (calculated as shown in Section 7.3.1) (W/m^2).

The temperature distribution in the nonporous debris is assumed to be parabolic:

$$T(z,t) = a + bz + cz^2 . \tag{7-4}$$

Coefficients a, b, and c in Equation (7-4) are obtained by the simultaneous solution of Equations (7-1) through (7-3). A solution for the temperature distribution is performed at each time step for each component group of fuel rods where nonporous debris is located.

A modification is required for the case of melting in the nonporous debris layer. In this case, the rate of melting of the nonporous layer must be calculated. The temperature at the upper surface of the crust is equal to the melting temperature of the material in the layer. The boundary condition for the top surface of the nonporous debris defines the rate of melting due to contact with the molten pool. Thus, the boundary conditions as given by Equation (7-3) is changed to the following two equations:

$$(d\delta/dt)h_{fus}\, \rho = k(\partial T(\delta,t)/\partial z) - q_d \qquad (7\text{-}5)$$

$$T(\delta,t) = T_{melt} \qquad (7\text{-}6)$$

where

k	=	thermal conductivity of the nonporous debris (W/m • K)
h_{fus}	=	heat of fusion of the nonporous debris (J/kg)
ρ	=	density of the nonporous debris (kg/m^3)
T_{melt}	=	melting temperature of the nonporous debris (K).

The coefficients a, b, and c in Equation (7-4) and the thickness of the layer of nonporous debris (δ) are obtained by simultaneous solution of Equations (7-1), (7-2), (7-5), and (7-6). A solution for the temperature distribution and thickness is performed at each time step for each group of fuel rods that contain a segment of the nonporous debris that supports the molten pool.

A crust thick enough to support a debris bed may form above a pool of molten material. The crust may also insulate the molten pool from coolant covering the molten pool. The thickening and thinning of this upper crust is modeled using the same integral method that is used for modeling the bottom crust. The melting of the crust is coupled with both the temperature of the molten pool and the thermal-hydraulic conditions above the molten pool. The crust is calculated to thin when the heat it receives from the molten pool is greater than the heat it transfers to the coolant. If the opposite case holds, the crust is calculated to thicken. If a debris bed above the molten pool is calculated to slump into the molten pool and the equilibrium temperature of the mixture is less than its solidus temperature, then the thickness of the upper crust is set equal to half the depth of the molten pool.

7.2   Formation and Heatup of Porous Debris

The thermal shocking by reflood water of a reactor core embrittled by oxidation results in the formation of porous debris. This section describes models for the formation and heatup of porous debris.

A study performed by Haggag[92] concluded that the Chung and Kassner model[93,94] accurately predicts the embrittlement and fragmentation of oxidized fuel rods. According to this model, cladding is embrittled when

$$\Delta r_{beta} < 0.1 \qquad (7\text{-}7)$$

where Δr_{beta} is the thickness of the cladding in the beta phase (mm).

Embrittled fuel rods are considered to break into particles during cooldown when the cladding temperature has decreased to

$$T_{clad} < T_{sat} + 100K \qquad (7\text{-}8)$$

where

T_{clad} = the temperature of the cladding (K)

T_{sat} = the saturation temperature of the coolant (K).

The porosity and particle size of the debris resulting from fragmentation is assumed to be the same as that formed by thermal shock during the TMI-2 accident. Analysis[95,96] of this debris determined that it had an average porosity of 0.54 and an average particle diameter of 0.87 mm. The characteristics of the TMI-2 debris varied spatially, but these variations are not taken into account in the modeling.

Flow resistance may increase a factor of 100 at a location where fuel rods have broken into particles. This increase of flow resistance is in part due to the fact that fluid in a debris region contacts more surface area than fluid in a rodlike region. The hydraulic diameter defines the surface area per unit of fluid volume. If a RELAP5 control volume contains fuel rods that have changed from rodlike configuration to porous debris, then the hydraulic diameter of that volume is changed from a value corresponding to rodlike diameter to a value corresponding to porous debris. The hydraulic diameter corresponding to porous debris is calculated by

d_h = 4 (bed fluid volume) / (surface area of particles)

$$= 0.666 \varepsilon d_p / (1. - \varepsilon) \tag{7-9}$$

where

d_h = hydraulic diameter (m)

ε = porosity of the debris

d_p = diameter of the debris particles (m).

A second mechanism for fragmentation of a reactor core is instigated by the melting of cladding with a very thin oxide layer and a small enough amount of dissolved oxygen that it will not wet the fuel. Evidence for this mechanism is the debris formation that occurred in the upper part of the fuel bundle in the PBF Severe Fuel Damage Experiment 1-4.[97] Little oxidation occurred in this part of the fuel bundle due to steam starvation. The results of postirradiation examination for this experiment indicate that the debris in this part of the bundle had characteristics similar to the upper debris bed in the damaged TMI-2 core. This mode of debris formation is modeled to occur when

$$T_{clad} > T_m \text{ and } t_{ox} < 1 \times 10^{-2} \tag{7-10}$$

where

T_m = the melting temperature of the metallic cladding (approximately 2,200 K)

t_{ox} = the thickness of the cladding oxide (mm).

The heatup of porous debris is calculated using a lumped mass approach. The debris particles at an axial node of a fuel rod group are considered to constitute one lumped mass. Convective heat transfer between the debris particles and the fluid in the debris porosity is considered to be the only mechanism that can remove heat from the debris. The debris heatup is calculated by the equation

$$(M_1 C_{p1} + M_2 C_{p2} + ...)_{ij} \ (dT_{ij}/dt) = P_{ij} A_{ij} \ \Delta z_{ij} + Q_{rij} \tag{7-11}$$

where

M_{1ij}	=	mass of a type of material 1 at axial node i of fuel rod group j (kg)
C_{p1ij}	=	constant pressure specific heat of material 1 at axial node i of fuel rod group j (J/kg•K)
T_{ij}	=	average temperature of the debris particles at axial node i of fuel rod group j (K)
P_{ij}	=	volumetric heat generation rate (W/m^3)
A_{ij}	=	cross-sectional area (m^2)
Δz_{ij}	=	height of the i-th axial node (m)
Q_{rij}	=	rate of heat transfer between the fluid and the debris particles at the i-th axial node of fuel rod group j (W).

The method used to calculate the latter variable is described below. The heatup model accounts for decay heat in the debris particles but does not account for any oxidation of the particles. The model accounts for the heat of fusion of each material in the debris. The model is applied when the temperature of the debris is less than the melting temperature of the fuel and cladding oxide. After ceramic melting begins, the debris temperature is calculated by the molten pool model described in the following section.

An arbitrary distribution of porous debris throughout the reactor core region is taken into account in the modeling. At each time step, a map is constructed of the debris regions resulting from degeneration of segments of fuel rods into porous debris. This map is constructed in two steps. In the first step, an examination for fragmentation is made of each axial node of each fuel rod group defined by the code user. An identification is made of each axial node that satisfied the criteria for fragmentation. In the second step, each axial node with fragmented fuel rods is examined to determine whether it is contiguous at its bottom or top surface with another axial node with fragmented fuel rods. The axial nodes that are contiguous are combined into one debris region. An example of debris region mapping is shown in Figure 7-6. In the example, the reactor core was discretized into two groups of fuel rods, each of which was discretized into four axial nodes. In the example, fuel rod fragmentation has occurred at axial nodes 3 and 4 of Rod Group 1. These two fragmented fuel rods are combined into one debris region.

A fuel rod group defined by the code user may contain control rods. Any residue of control rods in that group is considered to be well mixed with the fuel rod debris.
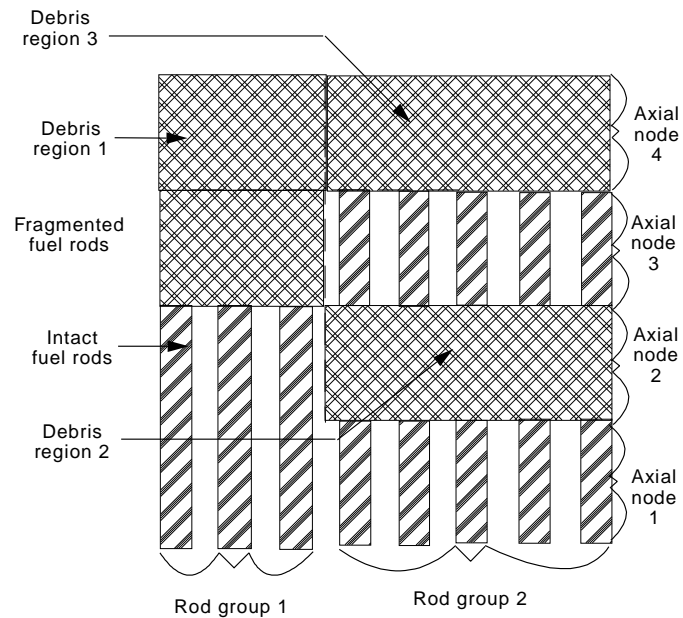
M222-BDR-1093-001

Figure 7-6. Example of calculated layout of rodlike and cohesive debris regions.

The method used to calculate the heat removal term Q_{rij} in the debris heatup equation is presented next. The calculation requires that the code user defines a RELAP5 control volume for each axial node of each group of fuel rods. Three states of the debris are identified, and an equation for the rate of heat removal is presented for each state. The three states of the debris are (a) debris in state of dryout, (b) debris in process of being quenched, and (c) debris in state of quench. The determination of the state of the debris is based upon the coolant void fraction and the debris temperature. The debris is considered to be in a state of dryout when

$$a_g > 0.9999 \tag{7-12}$$

where a_g is the volume fraction of fluid coolant in the vapor phase in the RELAP5 control volume containing the debris.

The debris is considered to be in a state of quench when

$$a_g < 0.9999 \tag{7-13}$$

$$T_{ij} < T_{sat} \tag{7-14}$$

where T_{ij} is the temperature of the debris (K). The debris is considered to be in a transition state when

$$a_g < 0.9999 \tag{7-15}$$

$$T_{ij} > T_{sat} \,. \tag{7-16}$$

For debris in a state of dryout, the heat transfer between the debris and vapor is calculated taking into account that the vapor has a small heat capacity relative to the debris and that the ratio of surface area to flow area is large. The assumption is made that vapor fluxing through a RELAP5 control volume attains the same temperature as the debris in that volume. This assumption applies for vapor velocities typical of those in a severe accident (0.01 to 0.1 m/s). The rate of heat transfer between the debris and vapor is calculated using the equation

$$Q_{rij} = \varepsilon A_{ij} \rho_{ij} v_{ij} [h(T_{ij}, P_{ij}) - h(T_{in}, P_{ij})] \quad Q_{rij} = \varepsilon A_{ij} \rho_{ij} v_{ij} [h(T_{ij}, P_{ij}) - h(T_{in}, P_{ij})] \tag{7-17}$$

where

ε = porosity of the debris

ρ_{ij} = density of the fluid (kg/m^3)

v_{ij} = velocity of the fluid (m/s)

$h(T,P)$ = enthalpy of the fluid (J/kg) at a temperature of T (K) and pressure of P (Pa)

T_{in} = temperature of the fluid as it fluxes into the RELAP5 control volume at the i-th axial node of the j-th fuel rod group (K).

The modeling of heat transfer in debris that is in a state of transition between dryout and quench is based on the idea of a quench front passing through the debris. The presence of such a quench front has been observed in experiments.[98,99,100,101] The modeling assumes that the rate of heat removal from the debris is proportional to the velocity of the quench front. For a top down quench, the quench front velocity is limited by the interphase drag between vapor fluxing upward and liquid fluxing downward.

The quench front velocity is calculated taking into account the force balance between flooding water and vapor produced by contact of flooding water with hot debris. Figure 7-7 shows the process that is modeled. Debris at the location of the quench front is considered to immediately transfer all of its stored thermal energy to the flooding water and generate vapor. The velocity of the quench front and the rate of vapor generation increase until the interphase drag between the vapor and liquid limits the rate at which liquid fluxes downward in response to gravity. The velocity of the quench front is related to the RELAP5 calculated rate of change of the volume fraction of liquid in the control volume containing the debris. The velocity is calculated by

$$\frac{dz_q}{dt} = \frac{[\alpha_f(t + \Delta t) - \alpha_f(t)]}{\varepsilon A_{ij} dt} \tag{7-18}$$

where

z_q = elevation of the quench front (m)

$\alpha_f(t)$ = volume fraction of liquid in the RELAP5 control volume at time t

Δt = the time step (s).
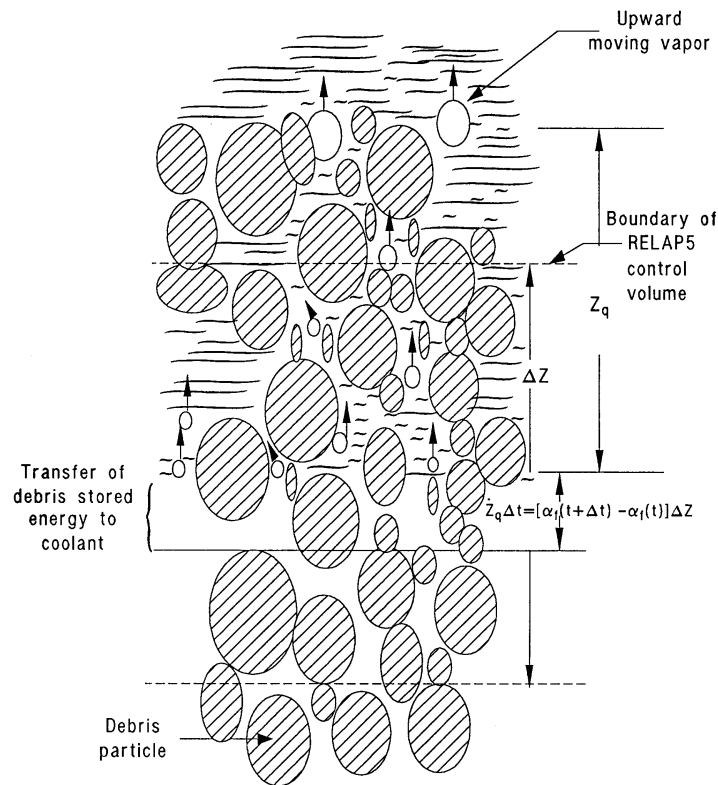
Figure 7-7. Configuration of partially quenched debris bed.

Because debris at the location of the quench front is considered to immediately transfer all of its stored thermal energy to the coolant, the rate of heat removal from the debris is proportional to the velocity of the quench front. This rate of heat removal is calculated by

$$Q_{fij} = u_{ij}(1 - \varepsilon)A_{ij}(dz_q/dt) \tag{7-19}$$

where

Q_{fij} =   rate of heat transfer from previously un-quenched debris to the liquid at the location of the quench front (W)

u_{ij} =   internal energy of the debris with reference to the saturation temperature of the liquid (J/m^3).

The rate of heat transfer from debris to liquid in the part of the RELAP5 control volume through which the quench front has already propagated is calculated by

$$Q_{qij} = P_{ij}\varepsilon A_{ij}a_f\Delta z_{ij} \tag{7-20}$$

where Q_{qij} is the heat transfer from debris that was already quenched at the start of the time step (W).

The total heat removed from the debris is calculated by

$$Q_{rij} = Q_{fij} + Q_{qij} \tag{7-21}$$

where Q_{rij} is the total rate of heat removal from debris at axial node i of fuel rod group j (W).

The volumetric vapor generation rate in a RELAP5 control volume through which the quench front is passing is calculated by

$$C_g = Q_{rij}/h_{fg}\varepsilon A_{ij}\Delta z_{ij} \tag{7-22}$$

where C_g is the volumetric vapor generation rate (kg/m^3•s).

In the portion of the RELAP5 control volume beyond the quench front, heat transfer between debris and coolant is considered to be negligible.

For a control volume through which a quench front has completely passed and all of the debris is thus in a state of quench, the rate of heat transfer from debris to coolant is calculated assuming that heat generated in the debris is immediately transferred to the coolant. The calculation takes into account the possibility that the rate of heat transfer is increased by a decreasing coolant pressure, and thus a decreasing saturation temperature. The rate of heat transfer is calculated by

$$Q_{rij} = P_{ij}A_{ij}\Delta z_{ij} + h_s A_{sij}\Delta z_{ij}(T_{ij} - T_{sat}) \tag{7-23}$$

where

h_s = heat transfer coefficient at the surface of the debris particles (W/m^2•K)

A_{sij} = surface area of debris per unit volume of debris bed for axial node 1 of fuel rod group j (m^2/m^3).

The variable h_s is assumed to have a constant value of 1,000 W/m^2•K. This simplification is justified because T_{ij} is almost equal to T_{sat}, and thus the second term in the above equation is small in magnitude compared to the first term.

The volumetric vapor generation rate at a location i at which all of the debris is quenched is calculated by

$$C_g = Q_{rij}/h_{fg}A_{ij}\Delta z_{ij} \, . \tag{7-24}$$

7.3 Molten Pool

The first occurrence of the melting of fuel and cladding oxide (ceramic melting) marks a significant advancement in the severity of an accident. If the melting has been driven by decay heat and not by oxidation, then in the absence of core reflood, melt progression will steadily progress from this time onward. The molten material does not immediately slump from the core region. Instead, the liquefied material either permeates into a colder region of the core and freezes or the movement of the liquefied material is blocked by the nonporous debris formed during the metallic meltdown of the core. But, as liquefaction continues the possibility increases that the pool may melt the material supporting it and a large amount of molten material may suddenly slump into the lower head of the reactor vessel. Thus, the unabated melting of fuel can lead to a thermal attack of the reactor vessel and a significant increase in the severity of an accident.

The situation of a partially molten reactor core is shown in Figure 7-8. In the case shown in the figure, the reactor core was nodalized into four axial nodes and three flow channels in the axial direction. The material in axial nodes 2 and 3 of flow channel 1 has been heated to the point where it is molten (ceramic melting). Gravitational forces provide the potential for the spreading of this molten material. If the region around the molten material is significantly cooler than the freezing temperature of the molten material, then a stable crust of previously molten material is formed that holds the molten material in place. If the region around the molten material is hot, then a stable crust does not form and the force of gravity causes the molten material to spread downward and laterally. In the example shown in Figure 7-8, models are applied to calculate the rate of spreading of molten material from flow channel 1 to flow channel 2 and from axial node 2 to axial node 1. The potential for spreading of the molten material is also a function of the volume of the molten material and its temperature. The larger the volume of molten material and the hotter its temperature, the more potential there is for the molten material to melt the crust at its boundary and spread.

The modeling of the heatup and the spreading of the molten material is performed by the molten pool model. Figure 7-9 shows the situation being represented by the model. The molten material in the molten pool is assumed to be mixed together due to turbulent natural convection. The molten pool model has the purpose of calculating the transient temperature of the molten pool and the rate of spreading of the molten pool. The model performs its calculations at each time step of the code in four steps. In the first step, the heat fluxes on the inner surfaces of the crust containing the molten pool are calculated. These heat fluxes vary with location; the heat flux on the upper part of the crust is significantly larger than that on the bottom part. In the second step, the stability of the crust containing the molten pool is determined based on the relative values of the heat fluxes on its inner and outer surfaces. If the crust is stable, the molten material stays in place. Otherwise, the molten material spreads. In the third step the rate of spreading of the molten pool at each location of its boundary is calculated. For locations of the boundary where the crust is stable, the rate of spreading is equal to zero. Finally, in the fourth step, the temperature of the molten material is calculated based on the difference between the heat generated in the molten pool and the heat transferred from the molten pool at its boundary. The calculations performed in each of these four steps are described below.

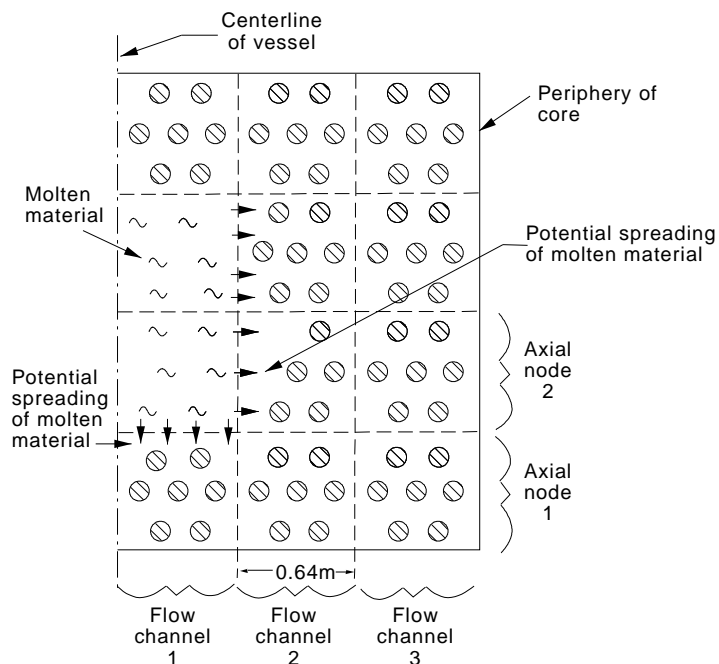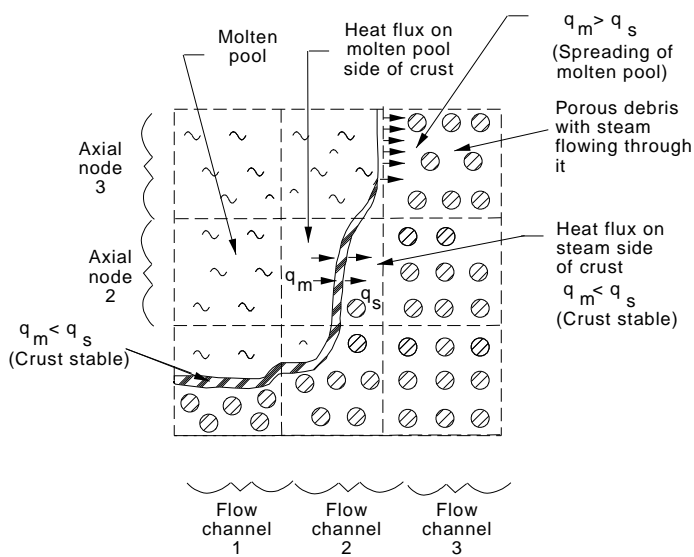**Figure 7-8.** The potential for spreading of the molten pool.

M158-BDR-1092-002

Figure 7-9. Physical process being represented by spreading model.

7.3.1 Heat Flux on Inner Surface of Crust

The heat fluxes on the inner surface of any portion of the crust that supports the molten pool are calculated using correlations developed by Jahn and Reineke.[102] These correlations were developed from the

results of experiments that measured the natural convection heat transfer coefficients at the boundary of a pool of fluid with internal heat generation. The correlations were applied by Epstein and Fauske[84] to the analysis of the molten pool of reactor material that evolved during the heatup stage of the TMI-2 accident. The correlations assume that the pool is in steady state. If the pool is rapidly increasing in temperature, the heat loss from the molten pool is overpredicted. The correlations calculate the heat flux at the bottom and top surfaces of the molten pool and at the sides of the molten pool. The heat fluxes at the various locations on the boundary of the pool are calculated by the equations

$$q_u = 0.36Ra^{0.23}k\Delta T / R \qquad\qquad (7\text{-}25)$$

$$q_b = 0.54Ra^{0.18}k\Delta T / R \qquad\qquad (7\text{-}26)$$

$$q_l = 2q_b \qquad\qquad (7\text{-}27)$$

where

q_u	=	heat flux from molten pool to crust at top of molten pool (W/m^2)
q_b	=	heat flux from molten pool to crust at bottom of molten pool (W/m^2)
q_l	=	heat flux from molten pool to crust at side of molten pool (W/m^2)
Ra	=	Rayleigh number of the liquid in the molten pool
k	=	thermal conductivity of the liquid in the molten pool $(W/m\bullet K)$
ΔT	=	difference in temperature between temperature of molten pool and its melting temperature (K)
R	=	effective radius of molten pool (m).

According to the analysis of Jahn and Reineke,[102] the heat flux on the bottom surface varies with location. The maximum downward heat flux is at the upper edge of the pool, and the minimum heat flux is at the bottom center of the pool. The heat flux at the upper edge is double the average heat flux on the bottom surface.

The effective radius of the molten pool is equal to the radius of a hemisphere that has the same volume as the volume of the molten pool. The effective radius is calculated by the equation

$$R = (1.5V_{pool}/\pi)^{0.33333} \qquad\qquad (7\text{-}28)$$

where

V_{pool}	=	volume of molten pool (m^3).

7.3.2 Stability of Crust Supporting Molten Pool

The model for calculating the stability of the crust is based on the framework shown in Figure 7-10. The crust at a location at the periphery of the molten pool is regarded as stable when the heat flux on the molten pool side of the crust is less than the heat flux on the steam side of the crust. If the heat flux on the molten pool side exceeds the heat flux on the steam side, then the crust melts and the molten material spreads in a direction perpendicular to the surface of the crust. The stability is checked at each axial node of each flow channel within which the crust resides. The crust at any locality is considered to stay in place when the following condition is satisfied:

$$q_{sij} > q_{mij} \tag{7-29}$$

where

$$q_{sij} \quad = \quad \text{heat flux on steam side of crust in flow channel i of axial node j (W/m}^2)$$

$$q_{mij} \quad = \quad \text{heat flux on molten pool side of crust in flow channel i of axial node j (W/m}^2).$$
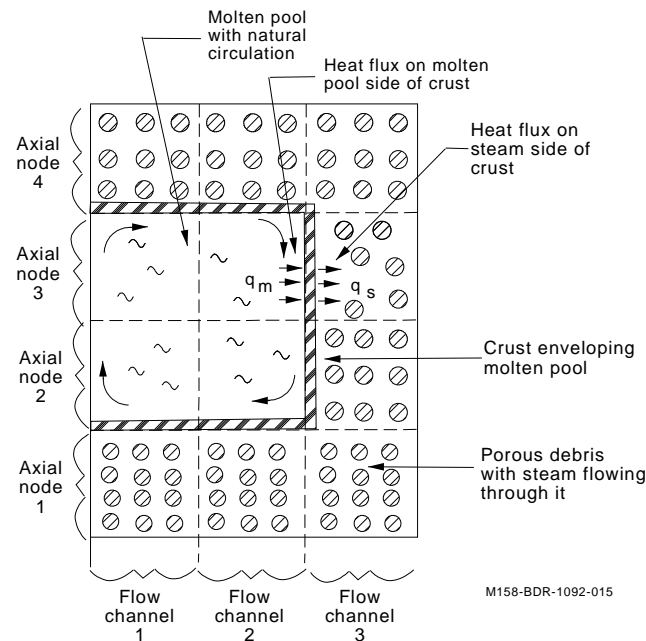
Figure 7-10. Framework for model calculating stability of crust.

The variable q_{sij} is calculated assuming the temperature of the crust on its steam side is at the solidus temperature of the crust. This assumption is appropriate for calculating the heat flux from the surface of a melting crust. The heat flux due to convection is assumed to be small compared to that due to radiation. The heat flux is calculated by the equation

$$q_{sij} = \varepsilon e \sigma \left(T_D^4 - T_{sij}^4 \right) \tag{7-30}$$

where

ε	=	porosity of debris
e	=	emissivity of surface
σ	=	Stefan-Boltzmann constant = 5.67 x 10^{-8} W/(m^{2}K^4)
T_D^4	=	solidus temperature of crust (K)
T_{sij}^4	=	temperature of steam at axial node j of flow channel i (K).

The variable q_{mij} is calculated by the molten pool model as a function of several variables, including location of the crust, temperature, size, and Rayleigh number of the molten pool. The equations for calculating q_{mij} are similar to the equations presented in Section 7.3.1.

7.3.3   Rate of Spreading of Molten Pool

The model for calculating the rate of spreading of molten material is based on the concept of a sporadically moving crust enveloping the pool; the crust experiences repeated cycles of melting, flowing, and freezing. After the molten material penetrates some distance into the porous debris, its leading edge is cooled to the point of freezing and the spreading temporarily stops. The spreading resumes when the material between the original position of the crust and its current position has completely melted and is mixed with the other material in the molten pool.

The physical process being represented by the spreading model consists of five steps, as shown in Figure 7-11. The modeling of these five steps defines the movement and the thickness of the boundary layer that envelopes the molten pool. In the first step, the crust enveloping the molten pool melts through at some point. The melting occurs at any location where the heat flux on the molten pool side of the crust is greater than the heat flux on the steam side of the crust. In the second step, the molten material spreads into the porous debris. Because the porous debris is cooler than the molten material, heat is removed from the spreading molten material and transferred to the porous debris. In the third step, the leading edge of the spreading molten material freezes and temporarily plugs the spreading of the molten material. In the fourth step, the region penetrated by the spreading material, namely the region between the previous location of the crust and its current location, is assumed to heat up adiabatically. The region is a mixture of solid and liquid material and is assumed to not be mixed with the molten pool until all of the solid material in the zone has melted. The melting is caused by decay heat in the solid material and in the molten material that penetrated the porous debris. In the fifth step, the molten pool expands to the inner surface of the crust formed by the freezing of the leading edge of the spreading molten material. The material through which the molten material spread is mixed into the molten pool. The modeling of this five step process results in a model that calculates the rate of spreading of molten material as a function of the temperature and size of the molten pool, the flow rate and temperature of the fluid flowing through the porous debris adjacent to the molten pool, and the porosity and particle size of the porous debris adjacent to the molten pool.

The material at the leading edge of the spreading molten pool is assumed to not mix with the molten material behind it. Furthermore, the thickness of the leading edge is assumed to have a thickness equal to the diameter of the particles in the porous debris. The material at the leading edge is assumed to instantly heat the porous debris that it contacts to the temperature of the material at the leading edge; which is assumed to be the liquidus temperature of the molten material. The porous debris is assumed to have the

same liquidus temperature as the molten material. As the molten material spreads into relatively cold porous debris, its leading edge is eventually cooled to the point where it is completely frozen.
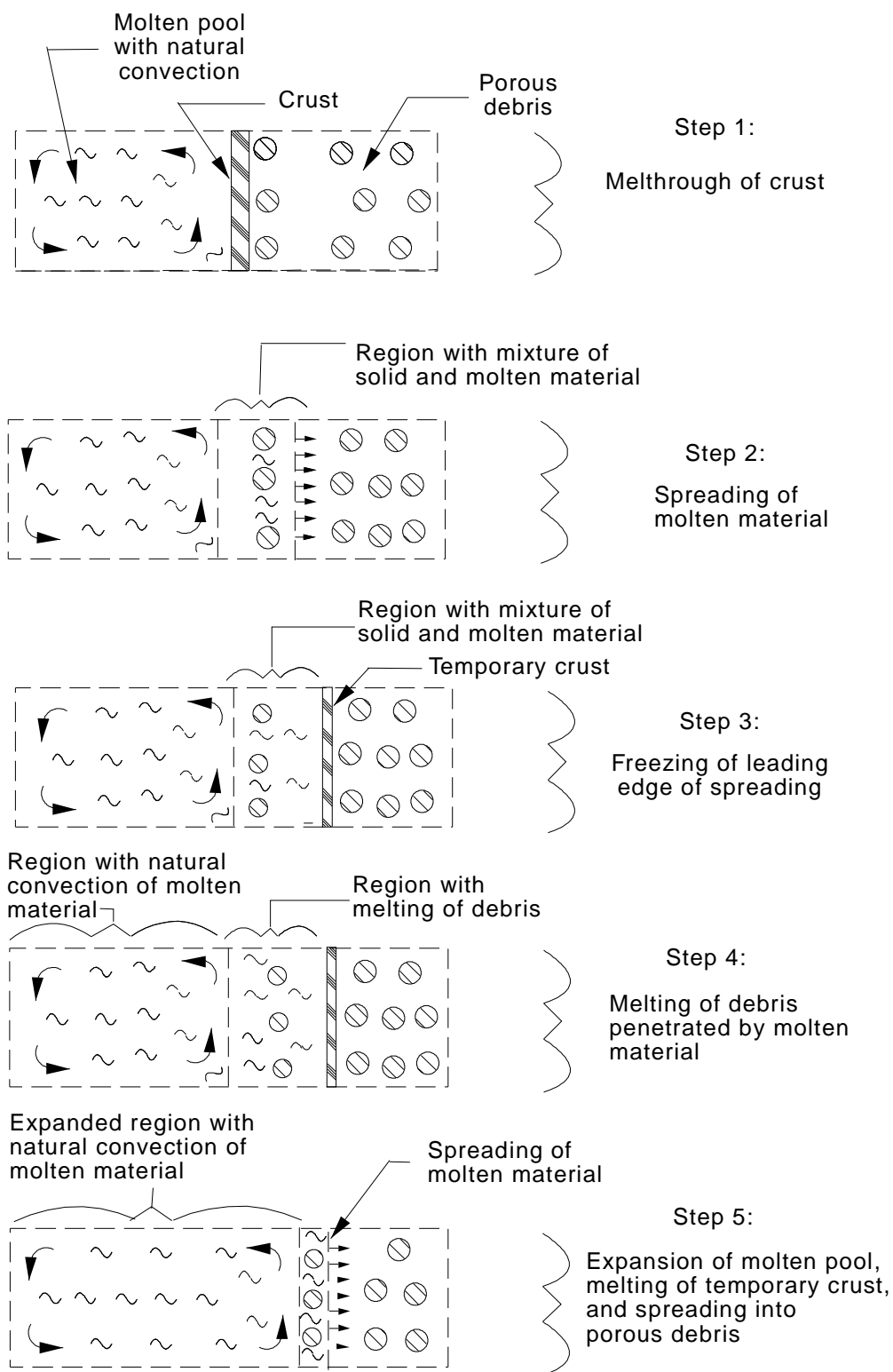

Figure 7-11. Sequences in process being represented by spreading model.

Figure 7-12 shows in schematic form the concept in heat transfer that is being used. In the top part of the figure, molten material has begun to spread into the porous debris. The molten material is spreading from left to right. The temperature distribution in the porous debris is shown below the schematic representation of the spreading molten material. The temperature of the porous debris is initially less than the liquidus temperature of the molten material, which is represented by the symbol T_L. Thus, the porous debris is a sink for the heat in the leading edge of the spreading molten material. As the leading edge advances, it is continually cooled and eventually becomes completely frozen. This state of the spreading process is shown in the bottom part of Figure 7-12. The advancement is then temporarily stopped until the solid material behind the leading edge is completely melted and mixed with the molten pool. Then, if the heat flux on the molten pool side of the crust is still greater than the heat flux on the steam side, the crust again melts and the spreading of the molten material continues.

The model for calculating the rate of spreading of molten material has two parts: (1) calculation to determine how far molten material spreads before its leading edge is frozen, and (2) calculation of time to melt the solid porous material through which the leading edge moved and which is left behind the leading edge. This solid material was heated to its melting temperature when the leading edge contacted it, but it is not melted until its internal energy increases by the value of its heat of fusion. The derivation of the equations to calculate each of these parts of the model are presented next.

The model is next derived for calculating the distance that the leading edge of the molten material moves before freezing. The movement is assumed to be plugged when the leading edge becomes completely frozen. The change in internal energy of the leading edge of molten material spreading into porous debris is calculated by the equation

$$du = \frac{(1 - \varepsilon) A_w \rho_D c_p [T_L - T_D(x)] dx}{\varepsilon A_w \rho_m \Delta x_c} \tag{7-31}$$

where

|		
A_w	=	cross-sectional area of molten material that is penetrating porous medium (m^2)
$T_D(x)$	=	temperature of debris at position x (K)
x	=	distance that leading edge of molten material has penetrated into porous debris (m)
ρ_m	=	density of molten material (kg/m^3)
ρ_D	=	density of material constituting the porous debris (kg/m^3)
T_L	=	liquidus temperature of molten pool and of porous debris (K)
Δx_c	=	length of leading edge (m).
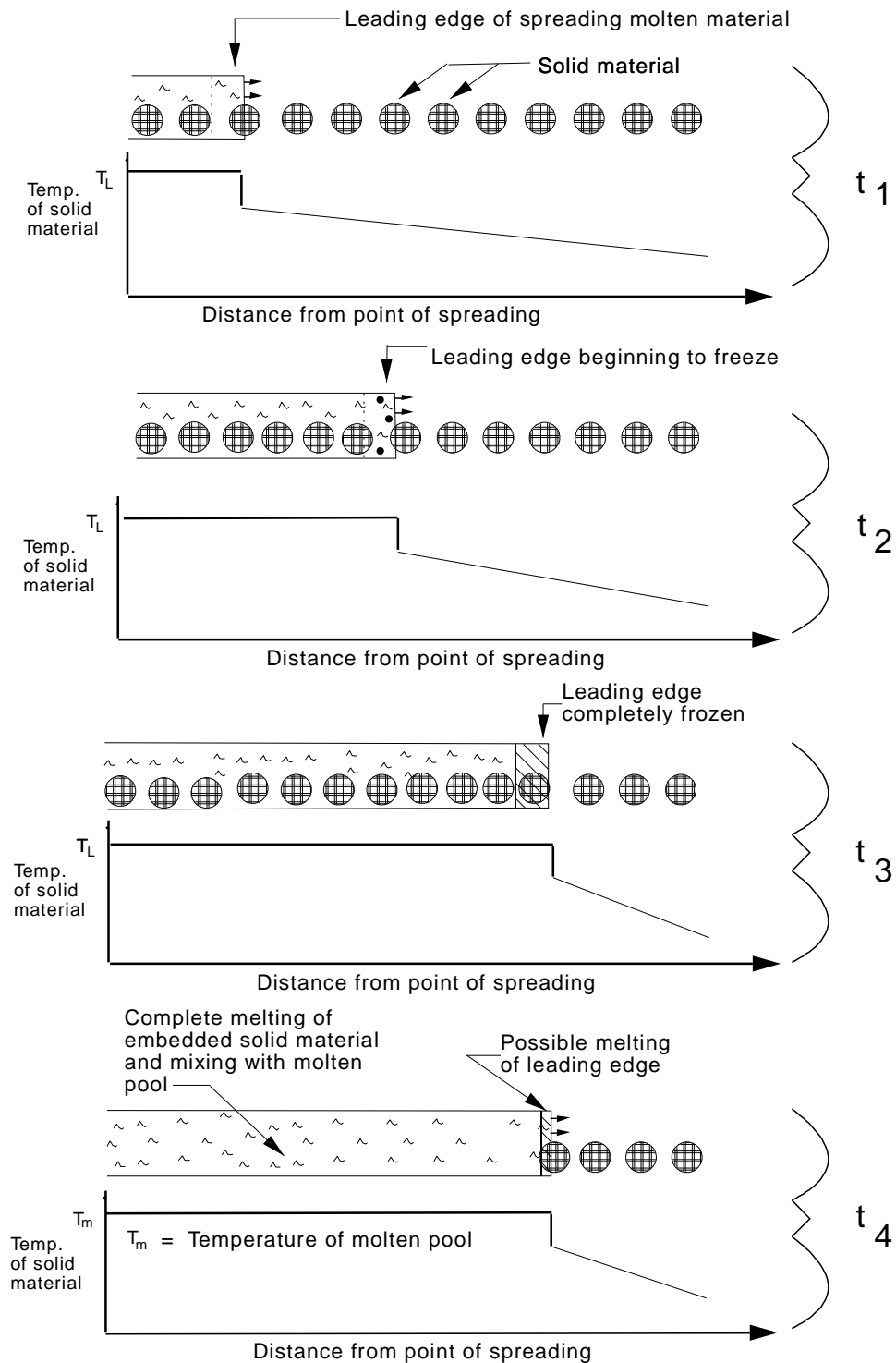
Figure 7-12. Conditions assumed by model for calculating distance of penetration of molten material into porous debris.

In Equation (7-31), the term $(1 - \varepsilon) A_w \rho_D c_p [T_L - T_D(x)]$ dx represents the energy (J) removed from the leading edge of the spreading molten material after it has spread the distance dx into the porous debris. This energy is transferred to the porous debris and heats the porous debris to the temperature T_L. The mass receiving this energy is represented by the term $(1 - \varepsilon) A_w \rho_D$ dx. The mass of the leading edge of the spreading molten material is represented by the term $\varepsilon A_w \rho_m \Delta x_c$.

The variable Δx_c is assumed to be a function of the size of the particles in the porous debris. In particular, Δx_c is assumed to be defined by the equation

$$\Delta x_c = 2r_p \tag{7-32}$$

where

r_p $\qquad = \qquad$ radius of particles constituting the porous debris (m).

Applying the definition of the leading edge, Equation (7-31) becomes

$$du = \frac{(1 - \varepsilon) \rho_D c_p [T_L - T_D(x)] \, dx}{2 \varepsilon \rho_m r_p} \quad . \tag{7-33}$$

The temperature distribution in the porous debris is assumed to decrease with distance from the crust in a linear manner. The distribution is given by the equation

$$T_D(x) = T_L - \frac{\partial T}{\partial x} x \quad . \tag{7-34}$$

Substituting Equation (7-34) into Equation (7-33) results in the equation

$$du = \frac{(1 - \varepsilon) \rho_D c_p \left[T_L - \left(T_L - \frac{\partial T}{\partial x} x \right) \right] dx}{2 \varepsilon \rho_m r_p} = \frac{(1 - \varepsilon) \rho_D c_p \frac{\partial T}{\partial x} x \, dx}{2 \varepsilon \rho_m r_p} \quad . \tag{7-35}$$

Integration of Equation (7-35) results in

$$u = \frac{(1 - \varepsilon) \rho_D c_p \frac{\partial T}{\partial x} x^2}{4 \varepsilon \rho_m r_p} \quad . \tag{7-36}$$

The spreading is assumed to be plugged when the energy removed from the spreading material equals the heat of fusion of the molten material. The distance of spreading that causes plugging due to freezing is thus given by the equation

$$h_f = \frac{(1 - \varepsilon) \rho_D c_p \frac{\partial T}{\partial x} \Delta x_p^2}{4 \varepsilon \rho_m r_p} \tag{7-37}$$

where

h_f =   heat of fusion of molten material (J/kg)

Δx_p =   distance that molten material spreads into porous debris (m).

Solving Equation (7-37) for Δx_p, the result is

$$\Delta x_p = \left[\frac{4\varepsilon\rho_m r_p h_f}{(1-\varepsilon)\rho_D c_p \frac{\partial T}{\partial x}} \right]^{0.5} . \tag{7-38}$$

    The second part of the spreading model calculates the period of time required to melt the porous debris through which the molten material has spread. The simplifying assumption is made that no heat is conducted or convected out of the porous debris through which the molten material has spread. In other words, the porous debris is heated adiabatically. The porous debris was heated to its liquidus temperature by the leading edge of the porous debris. So the melting of the porous debris is complete when the internal energy of the porous debris has increased by the value of the heat of fusion of debris. The heat to melt the porous debris is supplied by the decay heat in the molten material and porous debris. The heat balance equation is thus

$$[(1 - \varepsilon)\, q_D + \varepsilon q_m]\, V\Delta t_m = (1 - \varepsilon)\rho_D h_{fD} V \tag{7-39}$$

where

q_D =   volumetric heat generation rate in the porous debris (W/m^3)

q_m =   volumetric heat generation rate in the molten material (W/m^3)

V =   volume of molten material and porous debris (m^3)

h_{fD} =   heat of fusion of porous debris (J/kg)

Δt_m =   time to melt the porous debris (s).

    The left side of Equation (7-39) represents the heat input to the porous debris and the right side represents the energy required to melt the porous debris.

Solving Equation (7-39) for the time to melt the porous debris, the result is

$$\Delta t_m = \frac{(1-\varepsilon)\,\rho_D h_{fD}}{(1-\varepsilon)\,q_D + \varepsilon q_m} . \tag{7-40}$$

    The rate of spreading of molten material can now be determined by combining Equations (7-38) and (7-40). Equation (7-38) calculates the distance the molten material spreads before it is plugged by freezing of the material at its leading edge. Equation (7-40) calculates the time required to melt the porous debris penetrated by the molten material. After the porous debris has melted, natural convection heat transfer in

the molten pool can again melt the crust formed by the freezing of the leading edge of the spreading molten material. If the heat flux on the molten pool side is still greater than the heat flux on the steam side, then the crust melts again. The rate of spreading of the molten material is calculated by the equation

$$
\tilde{v} = \frac{\Delta x_p}{\Delta t_m} = \frac{(1-\varepsilon)\, q_D + \varepsilon q_m}{(1-\varepsilon)\, \rho_D h_{fD}} \left[\frac{4\varepsilon \rho_m r_p h_f}{(1-\varepsilon)\, \rho_D c_p \dfrac{\partial T}{\partial x}} \right]^{0.5} .
\tag{7-41}
$$

The rate of spreading is a function of the porosity and particle size of the porous debris, the temperature gradient in the porous debris, and the volumetric heat generation rate in the molten material and porous debris. The rate of spreading decreases with decreasing porosity and particle size. The rate of spreading also decreases with an increasing temperature gradient in the porous debris. The rate of spreading increases with an increasing volumetric heat generation rate in the porous debris and molten material.

Equation (7-41) is applied wherever gravity can drive molten material through porous debris. It is applied at the sides and bottom of the molten pool at the locations at which the crust is not in a state of thermal stability. It is not applied at locations along the top surface of the molten pool. It is also not applied at locations where the molten pool is supported by cohesive debris resulting from the metallic meltdown of fuel rods. At these locations the time to melt through the cohesive debris is calculated by the model presented in Section 7.1. If melt-through of the cohesive debris is calculated to occur, then the spreading of the molten pool is calculated by Equation (7-41).

7.3.4 Temperature of Molten Pool

Heat is transferred by natural convection from the interior to the exterior of a pool of molten core material. Figure 7-13 shows the overall heat loss from a molten pool.
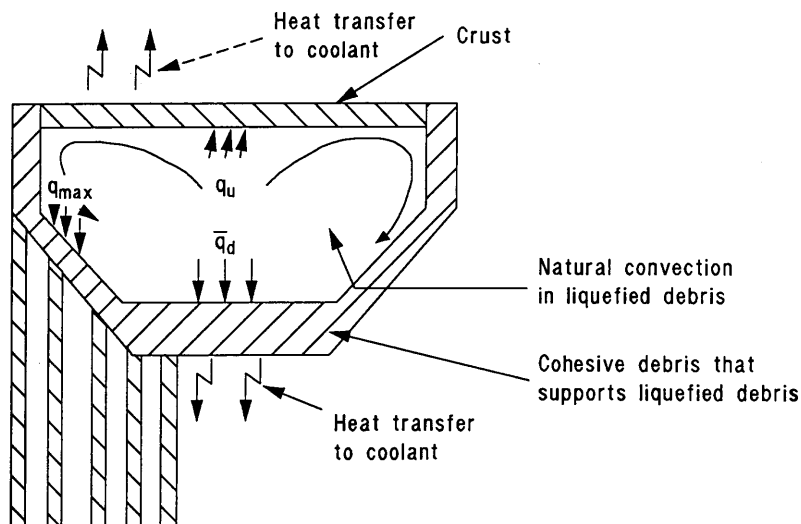

Figure 7-13. Heat transfer from pool of molten debris.

The change in temperature of the molten pool during a time step is calculated by

$$\Delta T_{pool} = (V_l Q_l - q_u A_u - q_d A_d)\Delta t - \Delta m c_m (T_0 - T_m))/\rho_l c_{pl} V_l \tag{7-42}$$

whereΔ

ΔT_{pool} =   temperature change of the molten pool during a time step (K)

V_l =   volume of the molten pool (m^3)

Q_l =   volumetric heat generation in the molten pool (W/m^3)

q_u =   heat flux from the molten pool into the crust above the pool (W/m^2)

q_d =   average heat flux from the outer surface of the crust that supports the pool at bottom and sides (W/m^2)

A_u =   area of the top surface of the molten pool (m^2)

A_d =   area of the bottom and sides of the molten pool (m^2)

Δt =   time step (s)

ρ_l =   density of the molten pool (kg/m^3)

c_{pl} =   heat capacity of the molten pool (J/kg•K)

Δm =   mass of previously solid porous material that melted and became part of molten pool during time step (kg)

c_m =   heat capacity of material that became part of molten pool during time step (J/Kg•K)

T_0 =   temperature of molten pool at start of time step (K)

T_m =   start of time step temperature of material that became part of molten pool during time step (K).

The variable Δm in the above equation is calculated by the model for calculating the rate of spreading of molten material through porous debris, which is described in Section 7.3.3.

7.4   Core Slumping Models

This section describes the models that determine when material from a molten pool in the core region slumps from this region to the lower head of the reactor vessel. Three events are considered to trigger this slumping. The first event is the melting of the vertically oriented crust at the periphery of the core that was containing the molten pool and keeping it from slumping into the core bypass region. The second event is the failure of the crust at the top of the molten pool that was supporting core material above the molten pool. This event is considered to cause slumping of the molten pool to the lower head only when the molten pool had already spread to the periphery of the core. The third event is the propagation of the molten pool to the elevation of the bottom of the core. In order to have the capability to perform a sensitivity study on the timing of core slumping, the provision is also provided for the code user to

prescribe the molten pool to slump to the lower head at the instant that the molten pool has spread to the periphery of the core. In all events that trigger slumping of the molten pool, the entire molten pool is considered to slump to the lower head.

Failure of the upper crust of the molten pool occurs when the upper crust has melted to a thickness of less than 0.5 mm and the crust is supporting core material. The crust is assumed to be supported by the liquid in the molten pool.

The failure of a metallic crust that is supporting the molten pool from the bottom is also considered. This case occurs when a molten pool propagates to a metallic crust that formed during the metallic meltdown of the core. If a downward spreading molten pool is encounters a metallic crust, then the metallic crust is considered to block the downward spreading of the molten pool until the metallic crust fails or is melted. After failure or melting of the metallic crust, the molten pool is considered to spread downward as it did before it encountered the metallic crust. The metallic crust is considered to fail when it has melted to a thickness of less than 25 mm.[103] The metallic crust is assumed to be supported by intact fuel rods. In order to have the capability to perform sensitivity studies, the code user can prescribe the failure thickness of the metallic crust and prescribe that the molten pool slumps to the lower head at the instant that failure of the metallic crust is calculated to occur.

These failure criteria are based on calculations of stress under conditions estimated for the TMI-2 accident and have a large degree of uncertainty. Even for a well-defined manufactured structure, the time of failure may be difficult to predict. For a structure that evolves during a severe accident and has uncertainties in configuration, composition, load, and temperature, the prediction of the time of failure is an order of magnitude more difficult. This large uncertainty in the calculation of crust failure requires that the severe accident analyst examine the effect of the failure criteria upon the calculated course of a severe accident. The failure criteria in the SCDAP/RELAP5 code are easily adjusted by the code user so this sensitivity study can be performed.

The degree of interaction of the slumping material with the water through which it falls is also defined by the code user. If the user defines that no interaction takes place, then the slumping core material is considered to fall as an intact stream and there is no transfer of internal energy from the slumping material to water. The slumped material that accumulates in the lower head is considered to have no porosity. If the user defines a complete interaction between slumping material and the water through which it falls, then the slumping material is considered to break up into small particles and transfer all of its internal energy to the water. The slumped material that accumulates in the lower head is considered to have a porosity of 0.5 and a particle size of 10 mm. The transfer of internal energy from the slumping material to water may cause a large amount of vapor generation and may significantly increase the pressure in the reactor vessel.

A user prescription of the behavior of slumping material is considered the best approach because of large uncertainties in the size and configuration of the breach through which the molten material drains. Also, an analysis of the breakup of slumping material is complicated by structures in the reactor vessel, such as core former plates, baffle plates, fuel rods, and spacer grids. As a result, it is necessary to enable a severe accident analyst to perform a sensitivity study of the behavior of slumping material.

8. MODEL FOR CREEP RUPTURE OF STRUCTURAL COMPONENTS

A model based on creep rupture theory is used to calculate the damage and nearness to rupture of structural components selected by the code user. Two different theories are applied: (1) Larson-Miller,[104] and (2) Manson-Haferd.[105] The particular theory to be applied is dependent on the material composition and stress. The materials that can be modeled for creep rupture are (a) A-508 Class 2 carbon steel, (b) 316 stainless steel, and (c) Inconel 600. For 316 stainless steel and Inconel 600 materials, the Larson-Miller theory is used. For A-508 Class 2 carbon steel, the Manson-Haferd theory is applied for the lower range of stress and the Larson-Miller theory for the higher range of stress.

Criteria for choosing the theory best suited for a particular material and temperature range are presented by Goldhoff.[106] His criteria determine the applicable theory by examining the results of creep rupture tests performed on specimens at a constant stress and temperature. After tests have been performed with a range of stresses and temperatures, the data are plotted to produce a family of curves of the log of rupture versus temperature and the log of rupture time versus reciprocal temperature. The Larson-Miller theory[104] gives the best prediction when the family of curves on a plot of log of rupture time versus reciprocal of test temperature meet at a point with a value of $1/T = 0$, where $T =$ temperature in degrees R. The Dorn[107] theory is used when the family of curves are parallel. The Manson-Haferd theory[105] is used when the family of curves on a plot of rupture time versus temperature meet at a point.

A parameter that measures creep damage is calculated at each time step for each structure being monitored for creep rupture. The creep damage is evaluated by the equation

$$D_c (t + \Delta t) = D_c (t) + \frac{\Delta t}{t_r (t)}$$
(8-1)

where

$D_c(t)$ =   creep damage at time t

Δt =   time step at current problem time (s)

$t_r(t)$ =   time required for the structure to fail by creep rupture at the current state of temperature and stress (s)

t =   problem time (s).

If the value of D_c is zero, the structure has not experienced any creep damage. If the value is one, the structure has failed due to creep damage.

The equation for calculating t_r is dependent on the material composition and stress. The equations for three materials considered by SCDAP/RELAP5 are shown in Table 8-1. The Manson-Haferd theory is applied to A-508 carbon steel for effective stresses less than 14 ksi (96.6 MPa). The Larson-Miller theory is applied to this material for effective stresses greater than 14 ksi (96.6 MPa) and to 316 stainless steel and Inconel 600 at all levels of stress.

Tests were performed at the INEL to obtain creep rupture data on A-508 Class 2 carbon steel.[108] Data were obtained in the temperature range of 900 to 1,025 K and in the stress range of 56 to 141 MPa. The creep rupture data for 316 stainless steel were obtained from Reference 104. Data were available in the temperature range of 700 to 1,089 K. The creep rupture data for Inconel 600 were obtained from References 104 and 109 and were available in the temperature range of 811 to 1,366 K.

Table 8-1. Equations for calculating the time to creep rupture.

Material	Range of Stress	Equation for Creep Rupture Time[a]
Carbon steel A-508	$0.0 < \sigma_{eff} < 14.0$	$t_r = 10^{\left[\frac{T - 1503.69}{P}\right]} + 3.499$ $P = 158.233\log(\sigma_{eff}) - 255.346$
	$14.0 \geq \sigma_{eff}$	$t_r = 10^{\left[\frac{P}{T} - 20\right]}$ $P = 9603.0\log(\sigma_{eff}) + 46454.0$
316 stainless steel	$0.0 < \sigma_{eff} < 52.0$	$t_r = 10^{\left[\frac{P}{T} - 20\right]}$ $P = -13320.0\log(\sigma_{eff}) + 54870.0$
	$52.0 \geq \sigma_{eff}$	$t_r = 10^{\left[\frac{P}{T} - 20\right]}$ $P = -64000.0\log(\sigma_{eff}) + 142000.0$
Inconel 600	$0.0 < \sigma_{eff}$	$t_r = 10^{\left[\frac{P}{T} - 15\right]}$ $P = -11333.0\log(\sigma_{eff}) + 43333.0$

a. **tr = time to rupture (h), T = average temperature of structure (R), seff = effective stress in structure (ksi).**

9. REFERENCES

1. T. Heames et al., *VICTORIA: A Mechanistic Model of Radionuclide Behavior in the Reactor Coolant System Under Sever Accident Conditions,* NUREG/CR-5545, SAND90-0756, Rev. 1, December 1992.

2. C. M. Allison, C. S. Miller, and N. L. Wade (Eds.) *RELAP5/MOD3 Code Manual*, Volumes I through IV, NUREG/CR-5535, EGG-2596, June 1990.

3. C. M. Allison and G. H. Beers, "Comparisons of the SCDAP Computer Code with Bundle Data Under Severe Accident Conditions," *Seventh International SMIRT Conference,* Chicago, IL, August 22-26, 1983.

4. E. C. Lemmon, *COUPLE/FLUID: A Two-Dimensional Finite Element Thermal Conduction and Advection Code*, EGG-ISD-SCD-80-1, February 1980.

5. J. Rest and S. A. Zawadzki, "FASTGRASS-VFP/PARAGRASS-VFP Version 50531, Users Guide," *Argonne National Laboratory Quarterly Report, January-March 1983,* Volume I, NUREG/CR-3689, ANL-83-85, Volume I, June 1983.

6. *PATRAN Plus User's Manual*, Release 2.4, PDA Engineering, Costa Mesa, CA, 1987.

7. *ABAQUS User's Manual*, Version 4.6, Hibbitt, Karlsson & Sorensen, Inc., Providence, RI, 1987.

8. D. M. Snider, K. L. Wagner, and W. Grush, *Nuclear Plant Analyzer (NPA) Reference Manual Mod1*, EGG-EAST-9096, April 1990.

9. K. D. Bergeron et al., *User's Manual for CONTAIN 1.0, A Computer Code for Severe Nuclear Reactor Accident Containment Analysis*, NUREG/CR-4085, SAND84-1204, May 1985.

10. L. T. Ritchie et al., *CRAC2 Model Description*, NUREG/CR-2552, SAND82-0342, March 1984.

11. D. I. Chanin et al., *MELCOR Accident Consequence Code System (MACCS Version 1.5)*, NUREG/CR-4691, SAND86-1562, July 1988, DRAFT.

12. C. D. Fletcher, *Computational Techniques for Fluid Dynamics, Volume 1*, Springer-Verlag, 1988, p. 107-121.

13. T. K. Sherwood, R. L. Pigford, and C. R. Wilke, *Mass Transfer*, New York: McGraw-Hill, 1975.

14. R. B. Bird, W. E. Stewart, and Lightfoot, *Transport Phenomena*, New York: Wiley, 1960.

15. E. W. Coryell et al., *Design Report: SCDAP/RELAP5 Reflood Oxidation Model*, EGG-RAAM-10307, October 1992.

16. S. Modro and M. Carboneau, *"The LP-FP-2 Severe Fuel Damage Scenario and Discussion of the Relative Influence of the Transient and Reflood Phases in Affecting the Final Condition of the Bundle,"* *OECD LOFT Final Meeting, Madrid, Spain, May 9-11, 1990.*

17. K. Minato et. al., *Zircaloy Oxidation and Cladding Deformation in PWR-Specific CORA Experiments*, KfK 4827, July 1991.

18. J. T. Prater and E. L. Courtright, *Properties of Reactor Fuel Materials at High Temperature*, NUREG/CR-4891, July 1987.

19. J. K. Hohorst et al., *SCDAP/RELAP5/MOD2 Code Manual, Volume 4: MATPRO--A Library of Materials Properties for Light-Water-Reactor Accident Analysis*, NUREG/CR-5273, EGG-2555, February 1990.

20. S. Hagen et al., "Out of Pile Experiments on Severe Fuel Damage Behavior of LWR Fuel Elements (CORA Program)," IAEA-SM-296/26, *International Symposium on Severe Accidents in Nuclear Power Plants, Sorrento, Italy, March 21-25, 1988.*

21. J. Rest, *Proceedings of the International Meeting on Thermal Nuclear Reactor Safety, Chicago, IL, August 29-September 2, 1982*, NUREG/CP-0027, February 1983, pp. 111-121.

22. J. Rest, "Evaluation of Volatile and Gaseous Fission Product Behavior in Water Reactor Fuel Under Normal and Severe Core Accident Conditions," *Nuclear Technology, 61*, 1983, pp. 33-48.

23. J. Rest, "An Improved Model for Fission Product Behavior in Nuclear Fuel Under Normal and Accident Conditions," *Journal of Nuclear Materials, 120*, 1984, pp. 195-212.

24. J. Rest, "The Mechanistic Prediction of Xenon, Iodine, and Cesium Release from LWR Fuel Under Degraded Core Accident Conditions," *Proceedings of the Topical Meeting on Fission Product Behavior and Source Term Research, Snowbird, UT, July 15-19, 1984.*

25. J. Rest, "The Coupled Kinetics of Grain Growth and Fission Product Behavior in Nuclear Fuel under Degraded Core Accident Conditions," *Journal of Nuclear Materials, 131*, 1985, pp. 291-302.

26. J. Rest, "The Prediction of Transient Fission-Gas Release and Fuel Microcracking under Severe Core-Accident Conditions," *Nuclear Technology*, 56, 1981, pp. 553.

27. M. H. Wood and J. R. Mathews, "On the Use of Grain Boundary Loss Terms in Fission Gas Release and Swelling Models," *Journal of Nuclear Materials, 89*, 1980, pp. 53-61.

28. B. G. Schnitzler, *Fission Product Decay Heat Modeling for Disrupted Fuel Regions (GDECAY)*, EGG-PHYS-5698, December 1981.

29. M. R. Kuhlman et al., CORSOR User's Manual, NUREG/CR-4173, BMI-2122, March 1985.

30. U. S. Nuclear Regulatory Commission, *Technical Bases for Estimating Fission Product Behavior During LWR Accidents*, NUREG-0772, June 1981.

31. M. J. Zucrow and J. D. Hoffman, *Gas Dynamics, Volume I,* New York: John Wiley and Sons, 1976.

32. J. H. Keenan et al., Gas Tables, 2nd Edition, New York: John Wiley and Sons, 1980.

33. W. C. Reynolds, *Thermodynamic Properties in SI*, Department of Mechanical Engineering, Stanford University, 1979.

34. McGraw-Hill, *Lange's Handbook of Chemistry*, New York: McGraw-Hill Book Co., 1973.

35. Y. S. Tailoukian and C. Y. Ho, *Properties of Nonmetallic Fluid Elements, Volume 2,* New York: McGraw-Hill Book Co., 1981.

36. A. G. Croff, *ORIGEN-2-A Revised and Updated Version of the Oak Ridge Isotope and Depletion Code*, ORNL-5621, July 1980.

37. G. A. Berna and C. M. Allison, *Component State Models for SCDAP*, EGG-CDD-5872, June 1982.

38. R. Hill, *The Mathematical Theory of Plasticity*, Oxford: Clarendon Press, 1950, pp. 317-325.

39. A. Mendelson, *Plasticity: Theory and Application*, New York: MacMillan, 1968, pp. 100-104.

40. M. P. Bohn, *FRACAS: A Subcode for the Analysis of Fuel Pellet Cladding Mechanical Interaction*, TREE-NUREG-1028, April 1977, pp. 29-33.

41. D. L. Hagrman, *Zircaloy Cladding Shape at Failure (BALON2)*, EGG-CDAP-5397, July 1981.

42. L. J. Siefken et al., *FRAP-T6: A Computer Code for the Transient Analysis of Oxide Fuel Rods*, EGG-CDAP-5410, April 1981.

43. E. R. Carlson, *Probabilistic Flow Area Reduction Model*, EGG-CDD-5567, November 1981.

44. G. A. Berna et al., *FRAPCON-2 Developmental Assessment*, NUREG/CR-1949, PNL-3849, July 1981.

45. J. P. C. Kleijnen, *Statistical Techniques in Simulation-Part II*, New York: Marcel Dekker, Inc., 1975.

46. P. Hofmann and H. Ostereka, "Dissolution of Solid UO_2 by Molten Zircaloy and the Modeling," Paper IAEA-SM-296/1, *International Symposium on Severe Accidents in Nuclear Power Plants, Sorrento, Italy, March 21-25, 1988.*

47. E. B. Dussan V. and Robert Tas-ping Chow, "On the Ability of Drops or Bubbles to Stick to Non-Horizontal Surfaces of Solids," *Journal of Fluid Mechanics, Vol. 137*, pp 1-29, 1983.

48. S. Hagen, L. Sepold, P. Hofmann and G. Schanz, *Out of Pile Experiments on LWR Severe Fuel Damage Behavior, Tests CORA-C and CORA-2*, KfK 4404, September 1988.

49. S. Hagen et al., *Results of SFD Experiment CORA-13 (OECD International Standard Problem 31)*, KfK 5054, February 1993.

50. S. M. Jensen, D. W. Akers and B. A. Pregger, *Postirradiation Examination Data and Analysis for OECD LOFT Fission Product Experiment LP-FP-2, Volumes 1 and 2*, OECD LOFT-T-3810, December 1989.

51. D. A. Petti et al, *PBF Severe Fuel Damage Test 1-4 Test Results Report*, NUREG/CR-5163, EGG-2542, EG&G Idaho, Inc., December 1986.

52. M. Epstein and H. K. Fausbe, *Theoretical Studies of Capillarity, Phase Change and Relocation Phenomena Encountered in a SRS AAssembly Meltdown (U)*, WSRC-RP-90-1287, November 1990.

53. T. R. Goodman, *"Application of Integral Methods to Transient Nonlinear Heat Transfer,"* Advances in Heat Transfer, 1 (1964), pp 51-120.

54. E. A. Garcia, P. Hofmann, and A. Denis, *Analysis and Modeling of the Chemical Interaction Between Inconel Grid Spacers and Zircaloy Cladding of LWR Fuel Rods; Formation of Liquid Phases Due to Chemical Interaction and its Modelinq*, KfK 4921, Kernforschungszentrum Karlsruhe, Germany, July 1992.

55. S. Hagen, P. Hofmann, G. Schranz, and L. Sepold, *Interactions in Zircaloy/UO_2 Fuel Rod Bundles with Inconel Spacers at Temperatures above 1,200 C*, KfK 4378, Kernforschungszentrum Karlsruhe, Germany, September 1990.

56. D. W. Akers et al., *TMI-2 Core Debris Grab Samples--Examination and Analysis*, GEND-INF-975, September 1986.

57. R. J. Lipinski, *A Model for Boiling and Dryout in Particle Beds*, NUREG/CR-2646, SAND82-0765, June 1982.

58. P. Hofmann and M. Machiewicz, *Chemical Behavior of (Ag,In,Cd) Absorber Rods in Severe Accidents*, KfK 4670, CNEA NT-16189, August 1990.

59. P. Hofmann, E. A. Garcia, and A. Denis, "Low-Temperature Liquefaction of LWR Core Components," *Severe Accident Research Program Partners Review Meeting, Brookhaven National Laboratory, Upton, NY, April 30 - Nay 4, 1990.*

60. F. Nagase et al., *Interaction Between Zircaloy Tube and Inconel Spacer Grid at High Temperature*, JAERI-M 90-165, Japan Atomic Energy Research Institute, August, 1990.

61. D. A. Petti et al, *PBF Severe Fuel Damage Test 1-4 Test Results Report*, NUREG/CR-5163, EGG-2542, December, 1986.

62. E. L. Tolman et al., *TMI-2 Accident Scenario Update*, EGG-TMI-7489, December 1986.

63. C. L. Hunt, *Effect of Steam Oxidation on the Strain of Fuel Sheathing at High Temperatures*, AECL-5559 (August 1976).

64. J. K. Hohorst, C. M. Allison, T. J. Haste, R. P. Hiles, and S. Hagen, "Assessment of SCDAP/RELAP5 Using Data from the CORA Melt Progression Experiments," *Severe Accident Modeling Topical Meeting on Nuclear Reactor Thermal Hydraulics (NURETH-5), September 21-24, 1992, Salt Lake City, UT.*

65. Wolfgang Hering, "CORA Experiments," *CORA International Workshop, Karlsruhe, Germany, September, 1990.*

66. F. P. Griffin and K. A. Smith, *BWR Control Blade/Channel Box Interaction and Melt Relocation Models for SCDAP*, ORNL/NRC/LTR-92/12/R1, December 31, 1992.

67. P. Hofmann, M. Markiewicz, and J. Spino, "Reasons for the Low-Temperature Failure of BWR Absorber Elements," *Severe Accident Research Program Partners Review Meeting, Idaho Falls, ID, April 10-14, 1989.*

68. L. Baker, Jr., *An Assessment of Existing Data on Zirconium Oxidation Under Hypothetical Accident Conditions in Light Water Reactors*, ANL/LWR/SAF 83-3, 1983.

69. L. Baker and L. C. Just, *Studies of Metal-Water Reactions at High Temperatures, III. Experimental and Theoretical Studies of the Zirconium-Water Reaction*, ANL-6548, May 1962.

70. J. F. White et al., *Seventh Annual Report-AEC Fuels and Materials Development Program*, GEMP-1004, March 1968.

71. T. J. Haste et al., *Zircaloy Oxidation Kinetics in the Temperature Range 700-1300 C*, IAEA-TC-657/4.7, September 1988.

72. S. Leistikow and G. Schanz, "Oxidation Kinetics and Related Phenomena of Zircaloy-4 Fuel Cladding Exposed to High Temperature Steam and Hydrogen-Steam Mixtures Under PWR Accident Conditions," *Nuclear Engineering and Design, 103*, 1987, pp. 65-84.

73. V. F. Urbanic and T. R. Heidrick, "High-Temperature Oxidation of Zircaloy-2 and Zircaloy-4 in Steam," *Journal of Nuclear Materials, 75*, 1978, pp. 251-61.

74. J. V. Cathcart et al., *Zirconium Metal-Water Oxidation Kinetics, IV - Reaction Rate Studies*, ORNL/NUREG-17, 1977.

75. Gunnar Eriksson, "Thermodynamic Studies of High-temperature Equilibriums, SOLGASMIX, a Computer Program for Calculation of Equilibrium Compositions in Multiphase Systems," *Chemica Scripta, Volume 8, Number 3*, 1975, pp. 100-103.

76. J. E. Kelly, J. T. Nitchevek, and M. L. Schway, "Heat Transfer Characteristics of Dry Porous Particular Beds with Internal Heat Generation," *Proceedings of ASME/JSME Thermal Engineering Joint Conference, Honolulu, HI, Volume 4, 1983*, p. 83.

77. S. Imura and E. Takegoshi, "Effect of Gas Pressure on the Effective Thermal Conductivity of Pack Beds," *Heat Transfer Japanese Research, 3,* 4, 1974, p. 13.

78. D. Vortmeyer, "Radiation in Packed Solids," *6th International Heat Transfer Conference, Toronto, Canada, 1978.*

79. G. P. Wilhite, D. Kunii, and J. M. Smith, "Heat Transfer in Beds of Fine Particles (Heat Transfer Perpendicular to Flow)," *AIChE Journal, 8,* 3, 1952, p. 340.

80. A. V. Luikov, A. G. Shashkov, L. L. Vasiliev, and Yu E. Fraiman, "Thermal Conductivity of Porous Systems," *International Journal of Heat Mass Transfer, 11,* 1968, p. 117.

81. E. C. Lemmon, "Multidimensional Integral Phase Change Approximations for Finite Element Conduction Codes," *Numerical Methods in Heat Transfer*, New York: John Wiley & Sons, 1982, pp. 201-213.

82. L. J. Siefken et al., *Extension to SCDAPRELAP5/MOD2 Debris Analysis Models for the Severe Accident Analysis of SRS Reactors, Final Design Report*, EGG-EAST-8508, June 1989.

83. R. L. Moore et al., "TMI-2 Degraded Core Heatup and Cooldown Analysis," *Nuclear Technology, v87,* December 1989, p. 990-1004

84. M. Epstein and H. K. Fauske, *The TMI-2 Core Relocation - Heat Transfer and Mechanisms*, EGG-TMI-7956, July 1987.

85. F. Mayinger et al., *Examination of Thermal-Hydraulic Processes and Heat Transfer in a Core Melt*, BMFT RS 48/1, 1976, Institute for Verfahrenstechnik der T. U. Hanover.

86. M. Jahn and H. H. Reineke, "Free Convection Heat Transfer with Internal Heat Source, Calculations and Measurements," *Proceedings of the International Meeting on Thermal Nuclear Reactor Safety*, NUREG/CR-0027, 2, February 1983, pp. 996-1010.

87. Z. R. Martinson et al., *PBF Severe Fuel Damage Test 1-1 Test Results Report*, NUREG/CR-4684, EGG-2463, October 1986.

88. A. B. Wahba and E. F. Hicken, "Ten Years of Experimenting in the Loss of Fluid Test (LOFT) Facility," *Atomkernenergie-kerntechnik, 49,* No. 1/2, 1986, pp. 68-73.

89. R. O. Gauntt et al., *The DF-4 BWR Control Blade/Channel Box Fuel Damage Experiment*, NUREG/CR-4671, SAND86-1443 (draft), March 1988.

90. D. O. Lanning and N. J. Lombardo, *Data Report for Full Length High Temperature Experiments*, PNL-6540, April 1988.

91. M. L. Russel, "TMI-2 Core Geometry," *Proceedings of the TMI-2 Topical Meeting, Washington, D.C., November 1988.*

92. F. M. Haggag, *Zircaloy Cladding Embrittlement Criteria: Comparison of In Pile and Out of Pile Results*, NUREG/CR-2757, July 1982.

93. F. M. Haggag, *Fuel Bundle Damage Propagation Models for SCDAP*, EGG-NSMD-5738, June 1983.

94. H. M. Chung and T. F. Kassner, *Embrittlement Criteria for Zircaloy Fuel Cladding Applicable to Accident Situations in Light Water Reactors*, NUREG/CR-1344, ANL-79-48, January 1980.

95. D. W. Akers et al., *TMI-2 Core Debris Grab Samples-Examination and Analysis*, GEND-INF-975, September 1986.

96. P. Kuan, *TMI-2 Upper Core Particle Bed Thermal Behavior*, EGG-TMI-7757, August 1987.

97. R. R. Hobbins et al., "PBF Severe Fuel Damage Test 1-4 Melt Progression Scenario," *Severe Accident Research Program Partner's Review Meeting, Sandia National Laboratories, Albuquerque, NM, April 25-30, 1988.*

98. L. Barleon et al., "Extended Dryout and Rewetting of Small Particle Core Debris," *Proceedings of the Sixth Information Exchange Meeting on Debris Coolability*, EPRI NP-4455, March 1986, p. 17.

99. K. R. Boldt et al., *DCC Degraded Core Coolability: Experiment and Analysis*, NUREG/CR-4606, SAND86-1033, September 1986.

100.T. Ginsberg et al., "Core Debris Quenching Heat Transfer Rates under Top and Bottom Flooding Conditions," *Proceedings International Meeting on LWR Severe Accident Evaluation, Volume 2, Cambridge, MA, August 1983.*

101.D. H. Cho et al., "On the Pattern of Water Penetration into a Hot Particle Bed," *Nuclear Technology*, *65*, 23, April 1984.

102.M. Jahn and H. Reineke, "Free Convection Heat Transfer with Internal Heat Sources, Calculations and Measurements," *Proceedings of the 5th International Heat Transfer Conference, Tokyo, Japan, September 1974.*

103.P. Kuan, *Core Relocation in the TMI-2 Accident*, EGG-TMI-7402, September 1986.

104.F. R. Larson and J. Miller, "A Time Temperature Relationship for Rupture and Creep Stress," *Transactions of the ASME*, July 1952, pp. 765-775.

105.S. S. Manson and A. M. Haferd, "A Linear Time Temperature Relation for Extrapolation of Creep and Stress Rupture Data," *NACA TN 2890*, March 1953.

106.R. M. Goldhoff, "A Comparison of Parameter Methods for Extrapolating High Temperature Data," *ASME Journal of Basic Engineering*, 1959, pp. 629-643.

107.R. L. Orr, O. D. Sherby, and J. E. Dorn "Correlation of Rupture Data for Metals at Elevated Temperatures," *Transactions of the ASME, 46*, 1954, p. 113.

108.B. L. Harris, V. N. Shah, and G. E. Korth, *Creep Rupture Failure of Three Components of the Reactor Primary Coolant System During the TMLB' Accident*, EGG-EA-7431, November 1986.

109.F. R. Larson and J. Miller, "A Time Temperature Relationship for Rupture and Creep Stress," *Transactions of the ASME*, July 1952, pp. 765-775.